

Photons in restricted topologies

Kyle Ballantine

A thesis submitted for the degree of
Doctor of Philosophy

Trinity College Dublin

2016

Declaration

I declare that this thesis has not been submitted as an exercise for a degree at this or any other university and it is entirely my own work.

I agree to deposit this thesis in the University's open access institutional repository or allow the library to do so on my behalf, subject to Irish Copyright Legislation and Trinity College Library conditions of use and acknowledgement.

Kyle Ballantine

Published material

Material from this thesis appears or will appear in the following papers:

K. E. Ballantine, J. F. Donegan, and P. R. Eastham. Conical diffraction and the dispersion surface of hyperbolic metamaterials *Phys. Rev. A*, 90:013803, July 2014.

K. E. Ballantine, J. F. Donegan, and P. R. Eastham. There are many ways to spin a photon: Half-quantisation of optical angular momentum, *Sci. Adv.* 2, e1501748 April 2016.

Acknowledgements

Firstly I would like to sincerely thank my supervisor, Prof. Paul Eastham, for his help and guidance over the course of this work. He has always been available for lengthy discussions and has constantly challenged me to improve my understanding. I would also like to warmly thank Prof. John Donegan, who got me started in research, and has always been willing to offer guidance when asked. I thank Prof. James Lunney, who has driven work in conical refraction over the years, and Rónán Darcy, who has done much experimental work on the topic. I would like to thank Nigel Carroll and Plamen Stamenov for their assistance with experimental matters.

On a more personal level, I would not have reached this stage without the help of many people. My deepest thanks to my parents, who've supported me every step of the way, and to my sister Kelly for many stimulating discussions. Thanks to Noelle, whose love and companionship have been invaluable. To my friends who have helped get me through the tough days, and celebrate the good ones. Leaving many people out, special thanks to Brendan, Tim, Brian, Chuan, and David, who as well as being a friend has taught me much of what I know about research.

Finally I would like to acknowledge funding from the European Regional Development Fund and the HEA, Ireland.

Summary

In this work we discuss three different aspects of the topological classification of propagating beams of light. This topological classification relies on global properties of the light beam, which are insensitive to local disorder or perturbations. However, topological invariants calculated for scalar fields may not fully describe a beam of light, which consists of a vector field which points in a particular direction at a given time. We consider the extension of the topological classification of light beams to cases where the polarisation is allowed to vary.

When the phase of a scalar electric field varies around a point, that field carries angular momentum, proportional to the magnitude of the change of phase. When the polarisation also varies, we show that there is a new angular momentum which is carried by such a beam. This generalised angular momentum accounts for the possible winding in both the direction of polarisation and the phase around a point. We show that the spectrum of this angular momentum can be a half-integer or an integer multiple of Planck's constant.

To confirm these predictions, we measure the angular momentum current in a beam with varying polarisation. As well as the classical current, we measure quantum fluctuations due to the discrete nature of the photons which carry this current. This experiment shows that the generalised angular momentum is indeed quantised in half-integer multiples of \hbar , and provides a general method for sorting and detecting beams according to their generalised angular momentum.

Next, we study a new class of material, the hyperbolic metamaterial, in the generic case where all three principal dielectric constants are unequal. These materials have negative dielectric constant in one direction, and positive but unequal in the other two. We show that the iso-frequency surface, that is the surface of wavevectors at which light of a constant frequency can propagate, consists of two sheets which meet at four linear intersection points. We derive a geometrical optics, and then a full diffraction theory of light propagating close to one of these directions.

We also include the effects of absorption and discuss how such a material could be realised in practice.

Finally, we examine the topological classification of light beams in periodic structures, in terms of their crystal wave vector k . Again we show that although it is possible to describe a single polarisation using the classification of scalar fields, when the polarisation is allowed to vary then this classification is no longer suitable. Instead we show that the propagation of the field can be described by a local non-Abelian gauge field. This non-Abelian field has an integer associated with it which classifies pairs of bands describing two orthogonal polarisations. We give a simple formula to compute the non-Abelian field and the invariant which classifies the winding of this field around loops in reciprocal space.

Contents

1	Introduction and motivation	1
1.1	Introduction	1
1.2	Topology and physics	3
1.2.1	General introduction	3
1.2.2	Winding numbers, optical vortices, and topological invariants	5
1.2.3	Dimension and quantisation	8
1.2.4	Topological invariants and edge states	11
1.2.5	Topological invariants in photonic systems	11
1.3	Conical refraction	13
1.3.1	Paraxial description of conical refraction	15
1.3.2	Gaussian circularly polarised input beam	16
1.4	Outline of thesis	18
2	Generalised angular momentum theory	21
2.1	Introduction	21
2.1.1	Angular momentum of light	23
2.1.2	Angular momentum in two dimensions and the paraxial approximation	26
2.1.3	Operators and eigenfunctions	28
2.1.4	Angular momentum in a conically refracted beam.	30
2.2	Generalised angular momentum	31
2.2.1	Introduction to generalised angular momentum	31
2.2.2	Generalised angular momentum: definition	33
2.2.3	Properties and discussion	35
2.3	Generalised angular momentum: measurement	37
2.3.1	Mechanical effects: angular momentum and torque	40
2.4	Quantum fluctuations of angular momentum	41

2.4.1	Angular momentum operator	41
2.4.2	Wavepacket states	43
2.5	Calculation of quantum fluctuations	45
2.5.1	Orbital angular momentum: coherent states	46
2.5.2	Orbital angular momentum: number states	48
2.5.3	Generalised angular momentum: number states	51
2.5.4	Generalised angular momentum: coherent states	53
2.6	Quantum operators and interferometer	55
2.7	Conclusions	57
3	Generalised angular momentum experiments	59
3.1	Introduction	59
3.2	Angular momentum current and interferometer	60
3.2.1	Shot noise and interferometer output	61
3.3	Varying generalised angular momentum in input beam	62
3.4	Experimental details	63
3.4.1	Dove prisms	63
3.4.2	Interferometer	66
3.4.3	CCD and photodiode	70
3.4.4	Amplifier design	71
3.4.5	Measuring shot noise	74
3.5	Classical results	76
3.5.1	Spin and orbital angular momentum	76
3.5.2	Generalised angular momentum	78
3.6	Quantum results	81
3.6.1	Spin and orbital angular momentum	81
3.6.2	Generalised angular momentum	83
3.7	Error analysis	84
3.8	Conclusions	87
4	Biaxial hyperbolic metamaterials	89
4.1	Introduction	89
4.2	Biaxial hyperbolic metamaterials	91
4.3	Fresnel equation and dispersion surfaces	93
4.3.1	Dispersion surfaces	93
4.3.2	Intersection points	96
4.4	Geometric optics in a hyperbolic metamaterial	98
4.4.1	Refractive index and polarisation	98
4.4.2	Poynting vector	100
4.5	Beyond geometric optics	102

4.5.1	Absorption	102
4.5.2	Diffraction	103
4.6	Phase diagrams and possible implementation	106
4.7	Discussion and conclusions	108
5	Gauge fields and topological invariants	111
5.1	Introduction	111
5.1.1	Geometric phase	112
5.1.2	Topological insulators	114
5.1.3	Photonic topological insulators	116
5.2	U(1) invariants in the presence of polarisation coupling	118
5.2.1	Example: chiral biaxial material	118
5.2.2	Homotopies between U(1) vortices	123
5.3	Non-Abelian gauge fields in paraxial optics	123
5.3.1	Calculation of finite operator	126
5.3.2	U(2) topological invariants	127
5.4	Non-Abelian gauge field of a chiral biaxial material	130
5.5	Conclusions	132
6	Concluding remarks	135
	Bibliography	139

List of Figures

1.1	Illustration of a topological invariant.	3
1.2	Example of phase of vortex.	4
1.3	Illustration of Gauss's Law.	4
1.4	Illustration of homotopy group.	6
1.5	Dispersion surface of light in a biaxial medium.	14
1.6	Intensity and polarisation of conically refracted Gaussian beam.	17
2.1	Schematic illustration of the difference between spin and orbital angular momentum of light.	24
2.2	Spin, orbital and total angular momentum current of conically refracted beam.	31
2.3	Illustration of simultaneous rotation of image and polarisation.	32
2.4	Illustration of rotation of polarisation ellipse	33
2.5	Polarisation profiles of beams with generalised angular momentum.	36
2.6	Illustration of optical sorting and manipulation of generalised angular momentum states.	39
2.7	Normalised noise power in the current of the generalised angular momentum $\hat{L} + \gamma\hat{S}$ as a function of γ	54
2.8	Illustration of quantum operator formalism for interferometer	55
3.1	High dynamic range logarithmic images of Bessel-like beams.	64
3.2	Interference patterns showing orbital angular momentum of the components of the conically refracted beam.	65
3.3	Illustration of rays passing through a fixed polarisation Dove prism.	65
3.4	Phase of the two orthogonal polarisations due to three reflections on passing through the Dove prism,	66
3.5	Illustration of optical sorting of generalised angular momentum states.	67
3.6	Annotated photograph of experimental setup.	69

3.7	Scaling of CCD and photodiode response with intensity	71
3.8	Schematic of the electronic equivalent circuit of the photodiode and the designed transimpedance amplifier.	72
3.9	Transimpedance gain and predicted noise from transimpedance amplifier as a function of frequency.	73
3.10	Measured background noise of transimpedance amplifier	73
3.11	Intensity noise spectrum of laser	75
3.12	Measured spin angular momentum current	76
3.13	Measured orbital angular momentum current	77
3.14	Images of orbital angular momentum components filtered by interferometer	78
3.15	Measured generalised angular momentum current	79
3.16	Images of generalised angular momentum components filtered by interferometer	80
3.17	Total CCD intensity showing switching between $j = 1/2$ and $j = -1/2$.	80
3.18	Measured Fano factor for spin angular momentum current	82
3.19	Measured Fano factor for orbital angular momentum current	83
3.20	Measured Fano factor for generalised angular momentum current	85
3.21	Fit of shot noise against DC voltage.	86
3.22	Residuals of measured noise from linear fit.	87
4.1	Example of common hyperbolic metamaterial configurations.	90
4.2	Illustration of negative refraction in a hyperbolic metamaterial	90
4.3	Iso-frequency surfaces for different possible principal dielectric index signs	94
4.4	Topological transition between Fresnel surfaces describing biaxial material and biaxial hyperbolic metamaterial	97
4.5	Degenerate points in biaxial material and biaxial hyperbolic metamaterial	98
4.6	Coordinate system for ray description	99
4.7	Poynting vector of conically refracted rays in a biaxial hyperbolic metamaterial	101
4.8	Iso-frequency surface in presence of absorption	103
4.9	Full diffraction pattern in a biaxial hyperbolic metamaterial	106
4.10	Phase diagram of effective medium theory of silver rods in alumina . . .	107
4.11	Density plots of biaxiality and median index of a biaxial HMM	108
5.1	Illustration of phase depending on path	113
5.2	Energy levels of Hamiltonian Eq. (5.20).	120
5.3	Polarisation and instantaneous field of the eigenvectors of Eq. (5.26). . .	121
5.4	Cross section of Berry flux for lower band of a chiral biaxial material. . .	122
5.5	Illustration of homotopy between a field with a vortex and a field with uniform phase.	124

5.6	The four matrix coefficients of the x component of the non-Abelian gauge potential A for a chiral biaxial material.	130
5.7	The two components of the non-Abelian field strength F for a chiral biaxial material	131

Chapter 1

Introduction and motivation

1.1 Introduction

The behaviour of any physical system is generally described by differential equations, which can depend in a complex way on many different parameters. Usually we can make precise predictions only for idealised systems, ignoring disorder. However, there are properties which cannot be affected by such disorder. For example, consider a knot in a rope which is fixed at both ends. This knot cannot come undone, no matter how the rope moves or frays, until the rope breaks completely. Topological properties such as this not only allow for precise characterisation, but also lead to physical laws which, at least in the range of applicability of the theory, are obeyed to an extremely high precision [1, 2, 3].

This topological description of matter leads not only to physical understanding, but also to applications in the design of devices which are insensitive to disorder [3, 4, 5]. The goal of topology in physics is therefore to understand the number of distinct, global arrangements of a physical system, and to use this understanding to design devices which, as long as they remain in one of these arrangements, are constrained to behave in a particular way.

In this work we discuss three aspects of the topological classification of beams of light. Such beams consist of oscillating electric fields which are described at each point by their phase, where in the cycle the field is, but also by their polarisation, the range of directions in which the field points over a cycle. While the phase is a crucial property in most topological descriptions of light, the polarisation is often neglected. We focus particularly on the case where this polarisation varies around the beam.

The first phenomenon we examine, angular momentum of light, concerns beams which are invariant under rotations. If the polarisation is constant, the electric field can be described by a complex scalar function of time and space, representing both the amplitude and the phase of the oscillation. Clearly for a scalar field the phase must return to its original value upon traversing a closed loop around the circumference of the beam. Hence, the number of windings in the phase is a fixed topological invariant [6, 7]. If the polarisation is also allowed to vary, then the field is a vector at each point. It may seem that the direction of the field should also rotate by an integer multiple of 2π . However, the polarisation is defined by an ellipse traced out by the vector field over one full oscillation. This ellipse is invariant under a π rotation. Hence we can consider in-homogeneously polarised beams, where the phase and polarisation can each rotate by a half-integer multiple of 2π , returning the field to its original state. We propose a new form for the total angular momentum which allows for the possibility of different rates of rotation of phase and polarisation.

The second subject is the iso-frequency surface of a crystal or metamaterial, particularly a hyperbolic metamaterial. It is known that when one dielectric constant of such a material is negative, the iso-frequency surface (the surface of wave-vectors at which light will propagate with a given frequency) undergoes a topological transition from an ellipsoid to a hyperboloid [8, 9]. We extend this to the case of one negative and two positive but unequal constants, and examine the intersections between the hyperboloid and ellipsoid. We derive the ray description of conical refraction in these materials and show that it is topologically and quantitatively distinct from conical refraction in a conventional biaxial material. We also develop a wave optics description, which allows us to obtain the diffraction patterns formed from arbitrary beams incident close to the optic axis. The resulting patterns lack circular symmetry and hence are qualitatively different from those obtained in conventional, positive index materials.

The third subject, topological invariants in photonic crystals, is also based on phase winding, this time around a closed loop not in real space, but in reciprocal, or k -space [10]. Here the crystal wave-vector k characterises the solutions of the wave equation in a periodic medium. We show that a new topological invariant, associated with windings in both the phase and the polarisation, is necessary. This invariant may lead to topologically protected edge states in photonic systems (i.e. photonic topological insulators) which are immune to generic, polarisation altering, scattering.

A more detailed outline of the thesis is given at the end of this chapter. In the remainder of this chapter we give a general introduction and motivational comments on two subjects. In section 1.2 we give a general introduction to the use of

topology in condensed matter and in photonics. In section 1.3 we give an introduction to the phenomenon of conical refraction, which results in a beam whose phase and polarisation both vary in space. Such a beam serves as a motivating example throughout the work. Additional background material on angular momentum, hyperbolic metamaterials, and the topological classification of periodic materials is given in the introduction to each individual chapter.

1.2 Topology and physics

1.2.1 General introduction

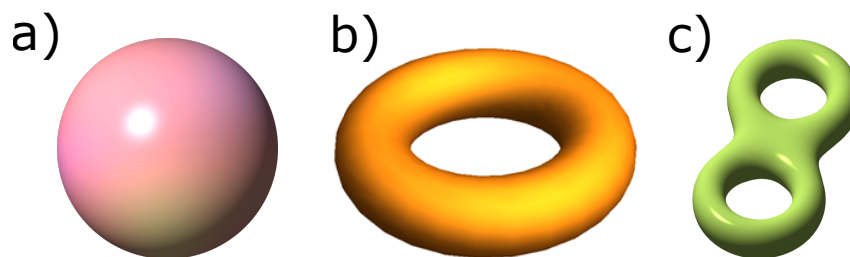


Figure 1.1: The familiar topological invariant is the genus of a structure, which counts the number of holes. The sphere a) is genus zero. b) A torus is genus one. c) A more exotic surface with genus two.

Topology is the study of those properties of an object which do not change when the object is smoothly deformed. Smooth deformations can be thought of as processes like stretching, twisting etc., but not processes like tearing and glueing. Perhaps the most well-known topological property is the genus, or number of holes an object has. For example a sphere has no holes. It has the same genus as any other such shape; cylinder, cube etc. However a torus, or doughnut shape has one hole, and so is topologically distinct. This concept is illustrated in Fig. 1.1.

Another, related, topological invariant is the phase winding number. Consider a complex scalar field $\psi(\vec{x})$, i.e. a function which associates a complex number to each point in space. If we travel around this space in a closed loop, we will arrive back at the same point. However complex numbers are only defined up to a phase of 2π , so $e^{i\delta} = e^{i(2n\pi+\delta)}$. Hence it is possible that over the course of the loop the phase increases by some multiple of 2π . An example is shown in Fig. 1.2, in two dimensions. Following a loop around the center, the phase increases by a total of 6π , going from red through all phases and back to red three times. We could stretch or compress this phase gradient in different parts of the plane, but there is no way to remove the phase winding without introducing a discontinuity to the surface.

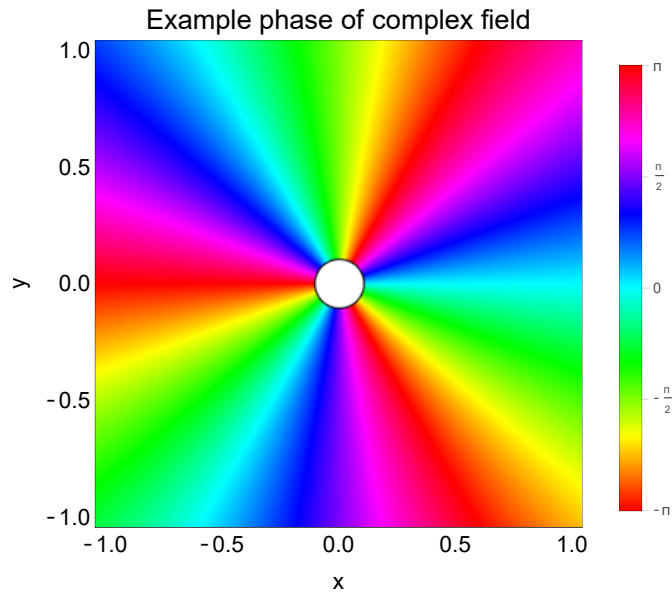


Figure 1.2: Example showing the phase (represented by colour) of a field with a vortex. In this case the phase changes by a total of 6π around the center, so the strength of the vortex is 3. Note the intensity must go to zero at the center of the vortex, as there is no way to smoothly join up the phase in each direction. Phase differences of 2π are irrelevant, so points which differ by a multiple of 2π are represented by the same colour.

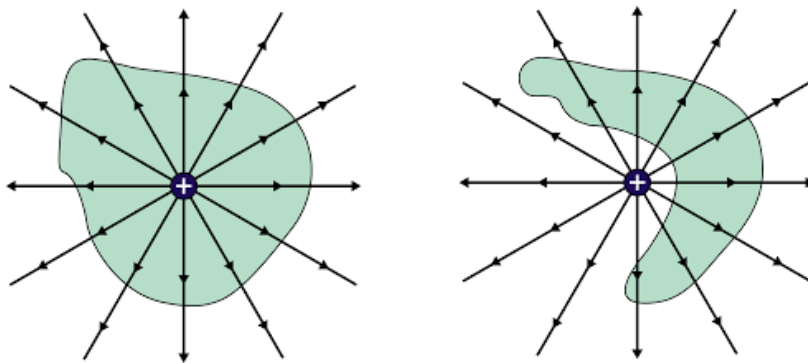


Figure 1.3: Illustration of Gauss's law. The flux at a particular point on the surface is, in general, not easy to calculate. However, the total flux through the surface is a simple topological invariant, the number of monopoles enclosed by the surface.

If we consider mathematical objects with additional structure, it may not be easy to sort them into different categories. Algebraic topology gives a link between global topological descriptions and local, algebraic, ones. A familiar example from physics is Gauss's law. Assuming quantisation of electric charge, the total charge inside a closed surface is a topological invariant. It cannot change smoothly but jumps by a fixed amount when a monopole crosses the surface. Gauss's law tells us that this total charge is equal, up to a constant, to the integral of electric flux across the entire surface,

$$\int \vec{E} \cdot d\vec{A} = Q_{enc}/\epsilon_0 \quad (1.1)$$

where \vec{E} is the electric field, $d\vec{A}$ a surface element, and Q_{enc} the total charge enclosed by the surface. This is a useful example to keep in mind. Locally, the flux through a bit of surface depends on the charge distribution and may not be easy to calculate. However, the total flux is a fixed quantity, which cannot be changed by smooth transformations either of the charge distribution, or the Gaussian surface. In the following we will come across examples of complicated local expressions, whose integrals are topological invariants. The local forms of the expressions depend on the particular details of that system, but the invariants capture some simple fixed property of the system as a whole.

1.2.2 Winding numbers, optical vortices, and topological invariants

As we have seen above, surfaces in three dimensions can be characterised by the number of holes. This concept is an important topological property of any space, either real coordinate space or some configuration space of a system. This property is described mathematically by the homotopy group of the space [11]. This group is obtained from the set of all possible closed loops by identifying two loops if one can be smoothly deformed into the other. For example, any loop on the surface of a sphere can be gradually contracted to a point. By contrast, a loop through the center of a torus cannot be contracted in this way. It is the holes in the space which can obstruct these smooth deformations and mean that not all loops are equivalent. This is illustrated in Fig. 1.4 for the example of a sphere and a torus. For a topological description of the space, the placement or size of the hole is irrelevant. What is important is how objects in the space can be configured around it.

Consider a field whose phase varies with angle ϕ , for example as $\psi \propto e^{il\phi}$ with l an integer. Such a field could describe a light wave or a quantum wave-function for example. An example is shown in Fig. 1.2, with $l = 3$. If the field is continuous, then the amplitude must go to zero at the origin where the angle ϕ , and hence the phase, is not well-defined. This requirement for a point (or in higher dimensions a line or

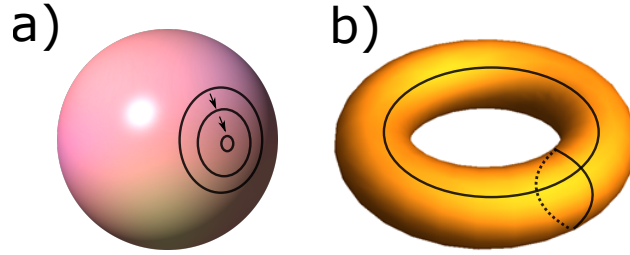


Figure 1.4: The homotopy group, which describes how loops can be contracted, gives a mathematical formulation of the concept of the number of holes in a space. On a surface with no holes, such as the surface of a sphere, every loop can be contracted to a point. On a more complicated surface such as a torus, loops around the central hole cannot be contracted. The number of different loops which cannot be contracted into each other characterises the surface.

surface) of zero intensity changes the topological nature of the configuration space of the field. Although the intensity distribution and the phase can be varied around the ring, there is no way to smoothly vary the total phase increase $2\pi l$ without breaking the ring of non-zero intensity. This type of phase winding appears in the creation of optical vortices which carry optical angular momentum [12, 13, 14, 15], as well as the topological invariants which are required by phase windings in the Brillouin zone in periodic crystals [10, 16]. In the latter case a gauge transformation, a local redefinition of the phase of the field and the vector potential, which are not independently observable, can be used to move the singularity. However, on a global level the topological charge, i.e. the total number of times the phase changes by 2π around the singularity, is unchanged.

Optical vortices in real space can be created using diffraction optics or spatial light modulators to imprint a $2\pi l$ phase shift around a beam [17, 18]. These vortices can interact in interesting ways. For example a vortex of strength l can split when perturbed into l independent vortices each with unit strength [19, 7]. Similarly two vortices with equal and opposite windings can annihilate [20]. For three dimensional scalar fields it has been shown that the lines of zero intensity around which the phase varies can loop around each other and form complex knots [21]. By varying parameters of the field, these lines can split and recombine in a way which preserves the direction and magnitude of the phase winding. For a collimated beam, these three dimensional knots can be seen as point vortices in a transverse plane which appear and annihilate in pairs, and circle around each other as they propagate [22].

When a coordinate or parameter is varied in a periodic way, more general phase windings can occur. This is due to the geometry of the wave-function's dependence on the parameters. This phase is known as the Berry phase [23]. The Berry phase is present in addition to the phase due to time evolution. Consider a Hamilto-

nian which depends on some set of parameters $\{\lambda_i\}$ such that its eigenvalues and eigenstates for given parameters are

$$H(\lambda) |n(\lambda)\rangle = \epsilon_n(\lambda) |n(\lambda)\rangle. \quad (1.2)$$

Then as $\vec{\lambda}$ is varied in time the states pick up both a dynamic and a geometric phase given by [23]

$$|n(\lambda(t))\rangle = e^{i\gamma_n(t)} e^{-\frac{i}{\hbar} \int_0^t \epsilon_n(\lambda(t')) dt'} |n(\lambda(0))\rangle, \quad (1.3)$$

$$\gamma_n(t) = i \int_{\lambda(0)}^{\lambda(t)} d\lambda \langle n(\lambda) | \nabla_\lambda | n(\lambda) \rangle. \quad (1.4)$$

This Berry phase γ can of course be included in the definition of the states $|n(\lambda)\rangle$, but crucially this can only be done locally. If two different paths through the space of possible $\{\lambda_i\}$ give different phases, then the difference does not depend on the choice of phase; it is gauge invariant. In particular the Berry phase picked up when traversing a closed loop, if it is not zero, cannot be made zero by any consistent choice of phases [23, 24].

In a periodic potential, the wave-functions which satisfy the Schrödinger equation have the form of Bloch waves,

$$\psi_{\vec{k}}(\vec{r}) = e^{i\vec{k}\cdot\vec{r}} u_n(\vec{r}), \quad (1.5)$$

labelled by the crystal momentum k and a discrete band index n . Here u_n is a periodic function with the same period as the potential. This is a general result of translation symmetry, and so the electromagnetic modes of a periodic medium have a similar form. As well as the band index n , which is an arbitrary label, each band can be characterised by a topological integer invariant, the Chern number. The Chern number, which is defined precisely below, is a topological number which is similar to the simple count of the number of holes in an object. Intuitively, it counts the number of times the phase of the energy eigenvectors increase by 2π around the edge of the Brillouin zone.

In a periodic medium the Berry phase is a function of the reciprocal momentum \vec{k} . The Berry connection gives the phase difference between two neighbouring points, and the line integral of this connection gives the Berry phase;

$$\mathcal{A}_n(\vec{k}) = i \langle n(\vec{k}) | \nabla_{\vec{k}} | n(\vec{k}) \rangle, \quad (1.6)$$

$$\gamma_n = \int_C d\vec{k} \cdot \mathcal{A}_n(\vec{k}). \quad (1.7)$$

Each band is then characterised by the integral of the connection around the edge of the Brillouin zone which, by Stokes theorem, is equal to the integral of the curl of that quantity across the surface of the Brillouin zone [25, 26]:

$$C_n = \frac{1}{4\pi} \oint_{\partial\text{BZ}} \mathcal{A}_n(\vec{k}) \cdot d\vec{k} = \frac{1}{4\pi} \int_{\text{BZ}} \nabla_{\vec{k}} \times \mathcal{A}_n(\vec{k}). \quad (1.8)$$

If the phase of the eigenstates $|n(\vec{k})\rangle$ can be chosen smoothly everywhere then the Chern number will be zero. However, it may happen that this phase cannot be smoothly defined at a number of discrete points. The Chern number simply counts the sum of the phase windings around each of these points, which must be an integer, just as the orbital angular momentum counts the phase winding around the circumference of a beam in real space. A different choice of gauge can move these singularities, meaning that the integral around an arbitrary loop is not invariant, but because the Brillouin zone is periodic moving the singularities has no effect and the Chern number is gauge invariant.

An important example of such a topological characterisation of a physical system is the TKNN invariant, named for Thouless, Kohmoto, Nightingale, and den Nijs, of the quantum Hall effect [25], historically one of the first to be discovered in condensed matter physics. This topological classification explains the plateaus in conductivity of a two-dimensional electron gas in a magnetic field as a result of an invariant which is confined to be an integer, and so cannot change smoothly. Each occupied band $|u_j\rangle$ contributes an integer

$$n_j = \frac{i}{2\pi} \int d\vec{k} (\langle \partial_{k_x} u_j | \partial_{k_y} u_j \rangle - \langle \partial_{k_y} u_j | \partial_{k_x} u_j \rangle) \quad (1.9)$$

to the quantised Hall conductance

$$\sigma_{xy} = \frac{e^2}{\hbar} \sum_j n_j. \quad (1.10)$$

Since each n_j depends on an integral of the curvature of the states over the whole Brillouin zone, it is a global, topological property of the wave-function.

1.2.3 Dimension and quantisation

Another significant result of topological considerations which will be crucial to what follows is their role in quantisation. This emerges in lower dimensional systems where the geometry is not sufficient to impose quantisation, which arises instead because of global topological requirements. (The dimension, which is often considered as a characterisation of a vector space, is itself more simply a topological property [27].) The restriction to two, one and even zero dimensions has led to many new phenomena in solid state physics [28, 29] and we will see that the paraxial restriction, from three-dimensional vector fields to two dimensional fields transverse to the propagation direction of a beam of light, leads to new insights into angular momentum.

In three dimensions, quantisation of angular momentum arises as a result of commutation relations

$$[\hat{L}_i, \hat{L}_j] = i\hbar\epsilon_{ijk}\hat{L}_k, \quad (1.11)$$

where \hat{L} is the quantum angular momentum operator $\hat{r} \times \hat{p}$. This relation leads to quantisation by the standard textbook argument [30]. Starting with the eigenstates of \hat{L}_z , considering the effect of the raising and lowering operators $\hat{L}_\pm = \hat{L}_x \pm i\hat{L}_y$ shows that these eigenstates must be labelled by discrete integers. The commutation relations are geometric constraints, applying equally to infinitesimal as well as finite rotations.

In two dimensions, say for a particle constrained to move in the x - y plane, only L_z is non-zero, and so there is no commutation relation to be obeyed. In this case quantisation comes from the requirement that the field is single-valued,

$$\psi(\phi + 2\pi) = \psi(\phi). \quad (1.12)$$

Assuming that $|\psi|$ is non-zero and that ψ is continuous then the phase must increase by a multiple of 2π around a loop,

$$\text{Arg}(\psi(\phi + 2\pi)) - \text{Arg}(\psi(\phi)) = 2\pi l \quad l \in \mathbb{Z}. \quad (1.13)$$

This restriction to integer l is therefore a global, topological property [31]. Accordingly, the condition Eq. 1.12 does not restrict ψ locally. Since the quantisation arises due to topology it is only sensitive to global properties of the space. The simplest function which fulfils the requirement in Eq. 1.12 is $\psi \propto e^{il\phi}$.

The global nature of quantisation in two dimensions is the underpinning of the Aharonov-Bohm effect, seen when electrons orbit a solenoid. For an ideal solenoid, the magnetic field is zero outside of the central core. However, the vector potential is non-zero, and when electrons complete a circuit of a solenoid they pick up a phase proportional to the magnetic flux,

$$\Delta\phi = \frac{e\Phi_B}{\hbar}, \quad (1.14)$$

where Φ_B is the magnetic flux through the solenoid [32]. The magnetic flux punctures the space, dividing paths into groups according to how many times they encircle it. When considering possible orbits of the solenoid, the space is equivalent to a two dimensional plane with the origin removed, $\mathbb{R}^2 - \{0\}$. Since every closed path is characterised by an integer n , the number of times it winds around the solenoid, the homotopy group of this space is the integers \mathbb{Z} . This winding leads to a total accumulated phase $n\Delta\phi$. Since the real, observable, magnetic field is given by the curl of the vector potential, we can add to this potential any function with zero curl. In particular we can choose a function which cancels the original potential in any region which does not fully enclose the solenoid. However, the overall phase gained when the electron completes a closed loop is gauge invariant, meaning it cannot be altered by such an addition.

This accumulated phase has an interesting implication for the angular momentum of two-dimensional particles [33]. In such a system, the restriction Eq. 1.12 will still hold if we demand single-valued wave-functions. However, according to the principle of minimal coupling the magnetic potential must be added to the kinetic momentum to obtain the canonical momentum

$$\vec{p} = \vec{p}_{\text{can}} - q\vec{A}. \quad (1.15)$$

where q is the charge and \vec{A} is the magnetic vector potential. Hence the angular momentum, which generates rotations [34], is

$$L_z = (\vec{r} \times \vec{p})_z = -i\hbar\partial_\phi + qA_\phi. \quad (1.16)$$

In the simplest single-valued gauge, $A_\phi = \Phi_B/2\pi$. The total angular momentum in units of \hbar is $l - (q\Phi/2\pi\hbar)$ which is non-integer. This is the most intriguing aspect of angular momentum in two dimensions: the angular momentum of a particle is not restricted to integer or half-integer values. A modified spin-statistics theorem holds, with interchanged particles picking up an arbitrary phase

$$|\psi_1\psi_2\rangle = e^{i\theta} |\psi_2\psi_1\rangle. \quad (1.17)$$

Such a particle is known as an anyon [34], and obeys so-called "fractional statistics", which reduce to Bose-Einstein or Fermi statistics when $\theta = 0, \pi$, respectively. For example in a strongly correlated electron gas confined to two dimensions, the interaction of each electron with the magnetic field of all other electrons gives rise to quasi-particles which obey fractional statistics. These have been observed in the fractional quantum Hall effect [35, 36].

An intriguing alternative description is obtained by absorbing the phase picked up upon orbiting the solenoid into a new boundary condition. To do this the magnetic potential can be removed globally by the transformation

$$\vec{A} \rightarrow \vec{A} - \nabla \frac{\Phi_B \phi}{2\pi}, \quad (1.18)$$

which does not affect the magnetic field \vec{B} . However, this transformation is discontinuous, for example across the negative x axis if we choose $\phi \in (-\pi, \pi)$. This leads to a boundary condition on ψ ,

$$\psi(\phi + 2\pi) = e^{iq\Phi_B} \psi(\phi) \quad (1.19)$$

$$\neq \psi(\phi). \quad (1.20)$$

The phase picked up upon orbiting the solenoid has been absorbed into a non-trivial boundary conditions of the coordinate space [34]. This illustrates the connection between the angular momentum in two dimensions and the global topological structure of the space.

1.2.4 Topological invariants and edge states

One reason why the topological classification of energy bands is important is the bulk-boundary correspondence. For an insulator with a gap between two sets of bands, the sum of the Chern number, given by Eq. 1.8, for all bands below the band-gap is a topological property which cannot be changed by smooth deformations [25]. When two such materials, with different invariants, are placed in contact, there is no way to smoothly interpolate between the two bandstructures at the boundary without closing the bandgap. Hence the interface between two topologically non-trivial insulators must have conducting states [3, 37, 38]. This relation between a property of the bulk material and its edge states is an example of the bulk-boundary correspondence: the behaviour at the interface between two materials is governed by the topological properties of the bulk bandstructures of each material.

The bulk-boundary correspondence is also responsible for the quantised transport in the quantum Hall effect [1, 39]. As remarked in section 1.2.2 there is an integer invariant which characterises each energy band. When the Fermi surface lies between these bands, the bulk material is insulating. However, when there is an interface between such a material and another insulator with a different topological classification, then there is no way to smoothly connect the bands across the interface without closing the energy gap. This topological requirement leads to at least one conducting state at the edge. The topological necessity of these states explains the remarkable precision of quantum Hall measurements [1], even in the presence of disorder and imperfections which are inevitable in any experiment.

1.2.5 Topological invariants in photonic systems

Topological invariants have been used to classify optical systems, both in real space and reciprocal space. As discussed in section 1.2.2, optical vortices, which exist when electromagnetic fields contain phase windings in real space, have been the subject of theoretical investigation [40, 41, 42]. They have also been used in many applications. Some, such as optical spanners [43, 44], rely on the angular momentum carried in such beams. However, others make use of the topological distinction between different vortices, for example to encode information [45, 46]. The discrete nature of the winding number, and the link between topology and quantisation, has also allowed researchers to explore a variety of fundamental quantum phenomena such as entanglement [47], generalised Bell inequalities [48], and the uncertainty principle [49].

Since the recent growth of interest in topological features of periodic condensed matter systems, there have been several efforts to transfer this theory to photonic systems, as well as other bosonic systems such as cold atoms and polaritons. There

are two main ways this has been achieved. The first is through a direct application of the topological classification of crystal band-structures to the energy bandstructure of photonic systems, for example photonic crystals. The second, less direct, method is to exploit analogies between electric fields and quantum wave-functions, in particular the formal equivalence between the two dimensional Schrödinger equation and the paraxial wave equation [50].

One distinction between fermions and bosons is the nature of the time-reversal operator. This is important because two states can be topologically distinct as long as a particular symmetry is present, but could be deformed into each other through intermediate states which break that symmetry. We will explain in section 5.1, when we discuss topological insulators in more detail, that for fermionic systems there is a class of topological insulators which are protected by time-reversal symmetry. Because the time-reversal operator behaves differently for fermions than for bosons, time-reversal invariant topological insulators cannot be directly implemented in photonic systems. Time-reversal symmetry can be explicitly broken, for example by including a Faraday material. Such an approach has been shown to lead to topologically non-trivial systems [51, 52]. More recently photonic topological insulators have been proposed using metamaterials [53]. In this case the permittivity and permeability of the metamaterial are tuned to be equal, so the topological classification is protected by electric-magnetic duality rather than time-reversal symmetry.

For a beam of light which consists of rays with small angle to the beam axis, we can make the paraxial approximation, which writes the beam as a plane wave multiplied by a slowly varying envelope function. Under this approximation, the three dimensional wave equation reduces to the paraxial Helmholtz equation

$$i \frac{dE}{dz} = -\frac{1}{2k} \nabla_{\perp}^2 E. \quad (1.21)$$

This equation governs the propagation along the beam axis z of the transverse field. In the case of light in a periodic medium which can be described as a set of weakly coupled paraxial beams, for example a two-dimensional lattice of weakly coupled wave-guides, it may not be necessary to explicitly break time dependence symmetry. The role of time is played by the z coordinate, and z symmetry can be broken by chirality. This has led to topologically protected edge states in a variety of systems [54, 55, 56].

A more general approach consists of using artificial gauge fields to break the time-reversal symmetry. An artificial gauge field can arise by tuning the system so that light picks up a non-zero-phase when it travels around a given loop. Such a loop then acts as a plaquette threaded by an effective magnetic flux. These systems do not truly break time-reversal symmetry, but rely on the presence of only a single polarisation or direction of propagation. Nevertheless, robust edge states have been predicted and measured using this approach [57, 58, 59].

These designs of topological materials without true time-reversal symmetry breaking rely on decoupling between the two polarisation states of light [38]. For example artificial gauge fields rely on a change of phase when light of a single polarisation moves around a loop. By overall time-reversal symmetry the opposite polarisation must pick up the same phase when traversing the loop in the opposite direction. Scattering from one polarisation in to the other can therefore lead to losses. In general scattering from arbitrary defects will not preserve polarisation, and such losses will be inevitable [60], undermining the topological robustness of transport for a single polarisation. Hence it is necessary to understand topological characterisation of beams with inhomogeneous polarisation. This will be the subject of chapter 5.

1.3 Conical refraction

One of our main results is to extend the topological characterisation of optical systems to include cases of inhomogeneous polarisation, i.e. where the ellipticity or the angle of the polarisation varies around the beam, either in real space or in k -space. The motivating example for this extension is the conically refracted beam, which has a polarisation and phase which varies with the azimuthal angle around the beam.

Conical refraction is a phenomenon which occurs in an anisotropic medium with no rotational symmetry. In a general medium the electric field \vec{E} and the electric displacement field \vec{D} are related by a tensor

$$\vec{D}_i = \epsilon_{ij} \vec{E}_j. \quad (1.22)$$

Depending on the crystal symmetry ϵ_{ij} , in a frame in which it is diagonal, can have one, two, or three distinct entries, called the principal dielectric constants. A more complete exploration of the resulting crystal optics is given in chapter 4, where we include the possibility of one or more negative dielectric constants. For now we note that for any direction of propagation in a medium, there are two refractive indices given by the Fresnel equation [61]. Depending on ϵ_{ij} these two indices may be equal. For each direction these indices describe the propagation of two orthogonal polarisations. If the two eigenvalues are not equal then the different polarisations experience different refractive indices, an effect known as birefringence.

The solutions to the Fresnel equation describe the propagation of plane waves in a particular direction in the crystal given by $\vec{k}/|k|$. These solutions can be visualised as surfaces in \vec{k} -space of wave-vectors at which light of constant frequency can propagate, i.e. $\omega(\vec{k}) = \omega_0$. Alternatively since the frequency is linked to the magnitude of the wave-vector through the refractive index $|k| = n\omega/c \equiv nk_0$, these surfaces can be interpreted as giving the magnitude of refractive index for any given direction

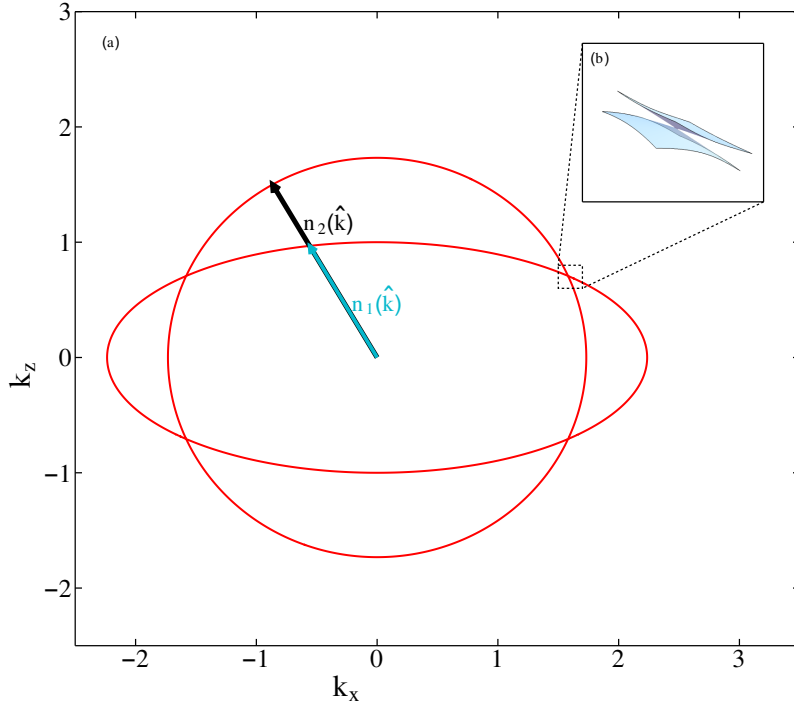


Figure 1.5: Dispersion surface of light in a biaxial medium. This can be interpreted as a constant frequency surface $\omega(\vec{k}) = \omega_0$ or as a polar plot of the refractive index $n_{1,2} = |\vec{k}|/k_0$ for different directions in k -space. The two surfaces give the refractive index for the two orthogonal polarisations. This picture shows that there are four points (directions in k space) where the surfaces intersect, and it is along these directions which conical refraction will occur. (a) Shows a cross section of this surface in the k_x - k_z plane showing four linear intersections. Inset (b) shows a close-up of the intersection in three dimensions.

of propagation. For a uniaxial material, with two equal dielectric constants, the refractive indices describing each polarisation are equal in two specific directions and the iso-frequency surfaces intersect quadratically in k -space. However, for a biaxial crystal, with all three dielectric constants unequal, the surfaces intersect at four points, with linear rather than quadratic intersections. These intersections are shown in Fig. 1.5. It is in the direction of these intersections which beams undergo conical refraction.

Conical refraction, first predicted by Hamilton and subsequently observed by LLOYD in 1832, is an interesting phenomenon of singular optics. The normal to the iso-frequency surface, which usually gives the direction of the Poynting vector associated with each ray [61], is not well defined at the linear intersection point. The only restriction on the direction of the Poynting vector is that it must be perpendicular to the electric field \vec{E} and the magnetic field \vec{H} . Similarly \vec{D} , $\vec{B} = \mu_0 \vec{H}$, and \vec{k} are all orthogonal. As \vec{D} takes different values in the plane orthogonal to \vec{k} , \vec{E} will

take values given by $\epsilon^{-1}\vec{D}$. The Poynting vector will take values perpendicular to \vec{E} and \vec{B} , which lie along a cone skewed away from \vec{k} . Thus a single ray of unpolarised or circularly polarised light will be refracted into a cone. Polarisation singularities of this type occur generically when the isotropic symmetry of vacuum is broken [62].

Although the main theory of conical refraction has long been established it remains an active area of research. Conical refraction has been utilised for applications such as optical trapping [63, 64, 65] and lasing [66]. Recently the conical refraction of non-Gaussian beams has been explored experimentally [67, 68]. As we will describe in chapter 2, the conically refracted beam also has a unique optical angular momentum distribution [69, 70].

1.3.1 Paraxial description of conical refraction

Since the conical diffraction beam will be used as the main example throughout this work, as well as in the experimental measurements in chapter 3, we now present a brief overview of the paraxial theory which describes such a beam. This treatment follows Berry [71], although the original formulation of conical refraction is due to Belskii and Khapalyuk [72, 73]. The solution of the paraxial wave equation in a biaxial medium is given by the evolution along the beam axis, taken to be the z axis, as a function of the orthogonal coordinates $\vec{R} = (x, y)$, of an initial electric field. This initial field evolves under a paraxial Hamiltonian

$$\vec{E}(\vec{R}, z) = \exp \left\{ -ik \int_0^z dz' H(\vec{P}, z') \right\} \vec{E}(\vec{R}, 0), \quad (1.23)$$

where

$$H = \frac{1}{2}P^2 + AP \begin{pmatrix} \cos \theta_p & \sin \theta_p \\ \sin \theta_p & -\cos \theta_p \end{pmatrix}, \quad (1.24)$$

$$= \frac{1}{2}P^2 + A\vec{P} \cdot \vec{\sigma}. \quad (1.25)$$

Here k_0 is the vacuum wave-vector ω/c , A is a measure of the biaxiality, $k = n_2 k_0$ where n_2 is the median refractive index (i.e. $n_1 < n_2 < n_3$, $n_i = \sqrt{\epsilon_i}$), P, θ_p are circular coordinates of the relative transverse wave-vector $\vec{P} = (k_x, k_y)^T/k_0$, and $\vec{\sigma} = \{\sigma_3, \sigma_1\}$ is the two-dimensional vector of Pauli matrices in a Cartesian vector basis. The unitary operator $\exp\{-ik \int dz H\}$ evolves the beam forward along the z axis according to the paraxial wave equation,

$$-i \frac{\partial \vec{E}}{\partial z} = H \vec{E}, \quad (1.26)$$

in exactly the same way as a quantum wave-function evolves in time via a unitary operator which satisfies the Schrödinger equation [50].

If the incident beam is uniformly polarised, with polarisation Jones vector \hat{e}_0 , and circularly symmetric, then Eq. 1.23 can be written as

$$\vec{E}(\vec{R}, z) = \left[B_0(R, Z) + B_1(R, Z) \begin{pmatrix} \cos \theta_r & \sin \theta_r \\ \sin \theta_r & -\cos \theta_r \end{pmatrix} \right] \hat{e}_0. \quad (1.27)$$

The coefficients B_0 and B_1 are integrals over Bessel beams given by

$$B_0 = k \int_0^\infty dP P a(P) \exp(-ikZP^2/2) \cos(kR_0P) J_0(kRP), \quad (1.28)$$

$$B_1 = k \int_0^\infty dP P a(P) \exp(-ikZP^2/2) \sin(kR_0P) J_1(kRP), \quad (1.29)$$

and $a(P)$ is the circularly symmetric Fourier transform of the incident field,

$$a(P) = k \int_0^\infty dR R E_0(R) J_0(kRP). \quad (1.30)$$

Here for simplicity Z is a re-scaled z coordinate $Z = l + (z - l)n_2$ where l is the length of the crystal, and $R_0 = Al$. Hence a uniformly polarised input beam is converted into two components. The first retains the original polarisation and the other, with a different spatial distribution, has its polarisation altered in a position dependent way.

1.3.2 Gaussian circularly polarised input beam

Of particular interest is the case of an incoming Gaussian beam with circular polarisation;

$$a(P) = kw^2 \exp(-k^2 P^2 w^2 / 2), \quad (1.31)$$

$$\hat{d}_0 = (1, \pm i)^T. \quad (1.32)$$

As explained further in section 2.1.2, the Jones vectors $(1, \pm i)^T$ correspond to left and right circularly polarised light respectively. In this case the matrix which appears in Eq. 1.27 both interchanges the circular polarisations and also adds a position dependent phase

$$\begin{pmatrix} \cos \theta_r & \sin \theta_r \\ \sin \theta_r & -\cos \theta_r \end{pmatrix} \begin{pmatrix} 1 \\ \pm i \end{pmatrix} = e^{\pm i\theta} \begin{pmatrix} 1 \\ \mp i \end{pmatrix}. \quad (1.33)$$

Hence the two polarisations from each term of Eq. 1.27 add with different phases at each point. Of particular importance is the focal image plane $Z = 0$, which would be the virtual image plane of the entrance face of the crystal if it were isotropic with the same average refractive index. In this plane the amplitudes $B_0 = B_1$, and so the sum results in linear polarisation with an angle of polarisation which varies around the beam. The beam intensity and polarisation is shown in Fig. 1.6. Figure 1.6(a) and (c) show the intensity distribution of the beam in the focal image plane and

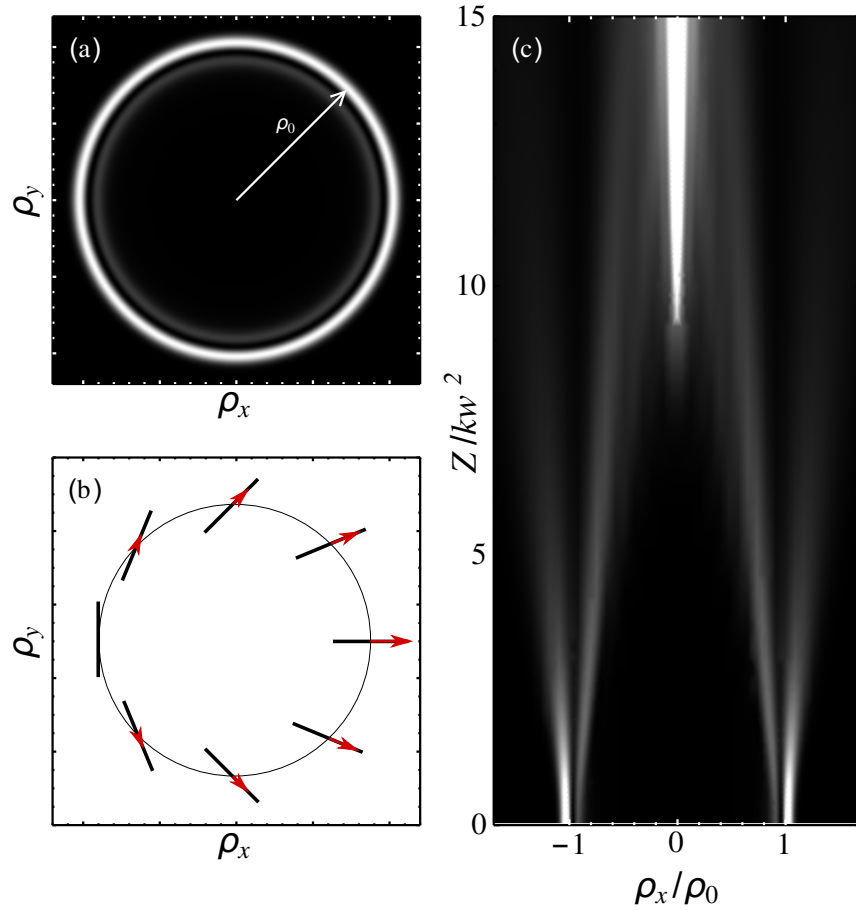


Figure 1.6: Intensity and polarisation of conically refracted Gaussian beam. (a) Intensity profile showing the double-ring structure in the focal image plane. (b) Schematic illustration showing the linear polarisation and the instantaneous electric field at a fixed time, around ring of the conically diffracted beam in the focal image plane as shown in (a). (c) Propagation of beam from the focal image plane, where it has a double ring structure, to the far-field where it is characterised by an on-axis spike.

under propagation along the z axis. Figure 1.6(b) shows the polarisation around the beam in the focal image plane. The arrows show the instantaneous field at a fixed time, illustrating the phase. The polarisation rotates by 180° around the circumference of the beam.

1.4 Outline of thesis

In this thesis we consider the spatially varying phase and polarisation of beams like those arising from conical refraction as the starting point for the investigation of inhomogeneous polarisation in several different contexts. This leads to extensions of the theoretical description of angular momentum of light, hyperbolic metamaterials, and topological invariants of photonic systems, in order to account for winding polarisation as well as phase.

In chapters 2 and 3 we show that there is a new class of angular momentum operators, which we refer to as generalised angular momentum. Chapter 2 provides the theoretical foundation of this generalised angular momentum. We derive the classical properties of this quantity and also obtain the associated quantum operator. The angular momentum is shown to have an appropriate mechanical effect in section 2.3. The quantum fluctuations in the angular momentum of both number and coherent states carrying generalised angular momentum are derived in section 2.4.

In chapter 3 we report a series of experiments to measure the generalised angular momentum, using a Mach-Zehnder interferometer which performs phase and polarisation rotations on the light in one arm relative to the other. We describe the experimental method in detail in section 3.4. We have measured the spin, orbital and generalised angular momentum current for various beams with the results given in section 3.5. The shot noise in the angular momentum current, which reveals the quantum of angular momentum, was also measured for spin, orbital and generalised angular momentum. The results, which show that the generalised angular momentum in a coherent beam may be carried in half-integer multiples of Planck's constant, appear in section 3.6.

In chapter 4 we extend the theory of conical diffraction to a new context, that of a hyperbolic metamaterial with at least one negative dielectric constant. We describe the topological change of the refractive index surface from ellipsoid to hyperboloid in section 4.3, and derive both the geometrical optics description (in section 4.4) and the full diffraction theory (in section 4.5) of light propagating close to an intersection of that surface.

In chapter 5 we extend the topological classification of photonic band-structures to cases in which the polarisation varies with direction in k -space. We show in section 5.2 that the usual Chern number defined for scalar fields does not properly

describe bands with varying polarisation as well as phase. In section 5.3 we show that a non-Abelian gauge field describes these bands, and that there is an integer topological invariant associated with this field. We derive simple formulas to calculate this field and the invariant in the presence of polarisation coupling. Finally in section 5.4 we illustrate these results by applying them to an example of a chiral biaxial material.

Because different chapters deal with various branches of optics, each chapter has its own introduction to the background literature in that field. Outside of these introduction sections the remaining work is original, except where cited.

Chapter 2

Generalised angular momentum theory

2.1 Introduction

In this chapter we turn to the first of the three subjects which we deal with in this thesis; angular momentum of light with inhomogeneous polarisation. This chapter consists of a theoretical exploration of a new quantity, which we call the generalised angular momentum. In chapter 3 we will turn to experimental measurements of the classical mean and the quantum fluctuations of this quantity for varying beams of light.

In general, the angular momentum carried by a beam of light can be decomposed into two contributions. The first is spin angular momentum, due to the rotation of the electric field vector at each point in space [74]. The second is the orbital angular momentum [17], due to varying phase around the beam as a whole, leading to an azimuthal component of the wave-vector. In three dimensions these two quantities combine equally to form the total angular momentum [75].

Effects due to the angular momentum of light have been studied since the first measurements of the torque exerted by beams of polarised light, and versions of those mechanical effects appear in experiments on optical trapping and manipulation [76]. Angular momentum effects are also emerging in the radio-frequency domain, for applications in astronomy and communications [45]. Fundamental interest focuses on the photon's angular momentum as a quantum-mechanical property [77]. The angular momentum of single photons has been measured [78], and entanglement [41] and EPR-like correlations [47] studied.

Many of these applications use either the spin or the orbital angular momentum independently, rather than the total angular momentum. This is possible because most laboratory beams are composed of rays at small angles to the beam axis. Such beams can be approximately described by the two dimensional field transverse to the beam axis. In this case the spin and orbital angular momentum are both physical [79, 42], and we can consider other quantities besides their sum.

If the electric field at a particular point in the beam does not have equal amplitude in all directions, then the electric field vector traces out an ellipse as it rotates, rather than a circle. The field is specified by the phase at each point, but also by the angle of the major axis of this ellipse. We will show that when this angle is allowed to vary in space then there is a generalised angular momentum which describes such beams. This generalised angular momentum is a linear combination of spin and orbital angular momentum with either integer or half-integer coefficients. Furthermore, the eigenvalues of this angular momentum can be half-integer as well as integer, leading to a value of angular momentum per photon which is a fractional multiple of Planck's constant. Fractional electronic charge and angular momentum has previously been observed by demonstrating a reduced shot noise in an electronic current [80]. Our results open the way to experiments studying fractional quantisation using photons in place of electrons [81, 82, 83, 84].

In the remainder of this introduction we describe the background theory behind the angular momentum of light, and also describe the angular momentum distribution in the conically refracted beam (see section 1.3), which will be used both as an illustrative example, and as the source of the experimental beams used in chapter 3. In section 2.2 we show that beams of light with inhomogeneous phase and polarisation can be described by a generalised angular momentum which is a linear combination of spin and orbital angular momentum. We consider some of the basic properties of this quantity and show why it takes the form which it does. In section 2.3 we show that this angular momentum could be measured by a suitable interferometer. We also show that there is an analogue of a half-wave plate which can convert the generalised angular momentum, and furthermore that such a device experiences the appropriate torque when doing so. In section 2.4 we move on to consider the quantum operator associated with the generalised angular momentum. In section 2.5 we calculate the mean and the quantum fluctuations in both the orbital and the generalised angular momentum current operators for a variety of states. We show that the quantum of generalised angular momentum current can be obtained by measuring the quantum noise in a coherent state. Finally in section 2.6 we show how this angular momentum current is related to the output of the interferometer considered in section 2.3 which will be used in the actual measurement.

2.1.1 Angular momentum of light

The mechanical properties of light were first explored by Poynting, concentrating on linear momentum. The Poynting vector [85] is the cross product of the electric and magnetic fields, and is proportional to the momentum density (momentum per unit volume) of an arbitrary electromagnetic field

$$\vec{P} = \epsilon_0 \vec{E} \times \vec{B}. \quad (2.1)$$

This linear momentum density is conserved in any medium with translation invariance, and can be measured in a variety of ways, for example by the pressure that a beam of light exerts when reflecting from an object [86].

In analogy to classical mechanics, we can define an angular momentum density which is simply the cross product of position with momentum. The total angular momentum is then

$$\vec{J} = \int d^3r \epsilon_0 \vec{r} \times [\vec{E} \times \vec{B}]. \quad (2.2)$$

This quantity is also conserved in a rotationally symmetric medium, and is known as optical angular momentum [85, 87]. In the presence of charged matter Eq. 2.2 contains contributions from longitudinal fields, i.e. electric fields which are parallel to the linear momentum density, at any point. These are due to the Coulomb forces between particles, and can be grouped with the angular momentum of the particles themselves. The contributions from the transverse fields are characteristic of propagating light [75]. In the following we will concentrate on the propagating part, due to the transverse fields, and ignore the possibility of free charges.

The magnetic field of a propagating wave can be described by a gauge dependent magnetic potential \vec{A} such that $\vec{B} = \nabla \times \vec{A}$. Using the part of the vector potential which is transverse to the linear momentum at each point \vec{A}_\perp , which is gauge invariant, and the transverse electric field \vec{E}_\perp , the total angular momentum can be written suggestively as $\vec{J} = \vec{L} + \vec{S}$ [88, 75] where

$$\vec{S} = \epsilon_0 \int d^3r \vec{E}_\perp \times \vec{A}_\perp, \quad (2.3)$$

$$\vec{L} = \epsilon_0 \int d^3r \vec{E}_\perp \cdot (\vec{r} \times \nabla) \vec{A}_\perp, \quad (2.4)$$

resemble a spin and orbital part. In particular the integrand in Eq. 2.3, which represents the spin angular momentum density, does not depend on the choice of coordinates while the integrand in Eq. 2.4 does, through the position vector \vec{r} . However, the orbital angular momentum obtained by integrating the density over all space is an intrinsic property of the beam which does not depend on the choice of origin [89].

Although this interpretation in terms of spin and orbital angular momentum is not without problems [75, 79], the spin angular momentum associated with circular polarisation has long been known. It was first demonstrated by Beth [90] by measuring the torque produced by circularly polarised light on a wave-plate. The polarisation of the light can be expressed in the basis of right and left circularly polarised light. In each of these states the electric field vector rotates clockwise or counter-clockwise as the beam propagates leading to an angular momentum of \hbar or $-\hbar$ per photon. This angular momentum is due to a rotating electric field, as illustrated in Fig. 2.1(a).

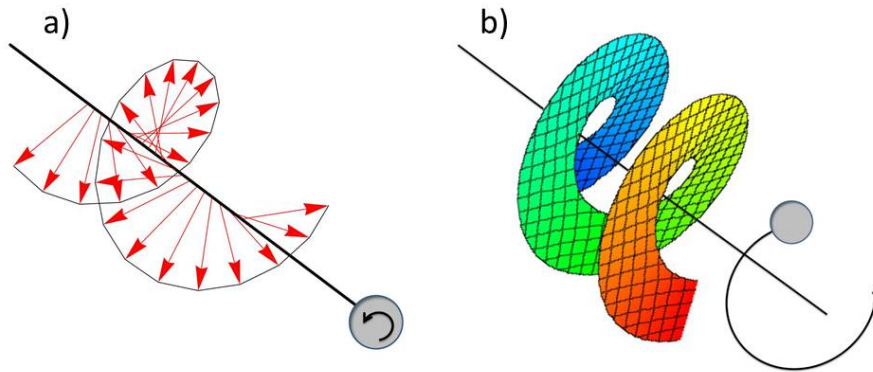


Figure 2.1: Schematic illustration of the difference between spin and orbital angular momentum of light. (a) Spin angular momentum can be pictured as a rotation of the vector polarisation in time, at each point in space. (b) Orbital angular momentum, due to the changing phase around the beam, can be pictured as the whole beam rotating about its centre. The intensity must be zero at the centre of the beam, as the phase is not defined.

The orbital part of the angular momentum is associated with light beams whose phase depends on the azimuthal angle around the beam. Vortices in waves such as light were first identified in 1987 [62]. The simplest example is a field which is proportional to $e^{il\phi}$ where l is an integer to ensure the field is single-valued [91]. The wave vector then has an off-axis component which spirals around the beam. This can be pictured as rotation of the beam as a whole around its centre. Each photon carries $l\hbar$, an integer multiple of Planck's constant, of orbital angular momentum. This type of angular momentum of light is illustrated schematically in Fig. 2.1(b).

The average angular momentum per photon, $\pm\hbar$ for circularly polarised light and $l\hbar$ for orbital angular momentum states, can be calculated classically as the angular momentum per unit energy, multiplied by $\hbar\omega$ [92]. However, these considerations carry through to quantum electrodynamics by noting that the electromagnetic field can be quantised by expanding in any complete set of orthonormal modes. The usual choice is plane waves inside a box, the volume of which is then taken to infinity [93]. To study angular momentum a more convenient basis set is Laguerre-Gauss modes,

each of which has a definite orbital and spin angular momentum. These have the form [87];

$$u_{l,p}(r, \phi, z) = e^{il\phi} f_{l,p}(r, z), \quad (2.5)$$

where l is an angular index, p a radial index which will be suppressed, and

$$f_{l,p}(r, z) = C_{pl} e^{-r^2/w^2} e^{-i(2p+|l|+1) \operatorname{atan}(z/z_r)} (-1)^p (r\sqrt{2}/w)^{|l|} L_p^{|l|}(2r^2/w^2). \quad (2.6)$$

Here C_{pl} , w , and z_r are constants which characterise the beam and p and l are integers. The Laguerre-Gauss modes are orthonormal when integrated over the plane transverse to the beam axis,

$$\int d^2r u_{l,p}(\vec{r}_\perp) u_{l',p'}(\vec{r}_\perp) = (2\pi)^2 \delta_{l,l'} \delta_{p,p'}, \quad (2.7)$$

and complete, i.e. any transverse field can be expanded as a linear combination of these modes [94].

The quantisation is done by expanding the field in these modes [95, 96],

$$\vec{E} = \sum_{l,\sigma} a_{l,\sigma} u_l e_\sigma + a_{l,\sigma}^* u_l^* e_\sigma, \quad (2.8)$$

with $e_{\pm 1}$ representing the right and left circular spin basis. The expansion coefficients are then promoted to operators and commutation relations imposed (a process known as canonical quantisation);

$$\begin{aligned} a_{l,\sigma} &\rightarrow \hat{a}_{l,\sigma}, \\ [\hat{a}_{l,\sigma}, \hat{a}_{l',\sigma'}^\dagger] &= \delta_{ll'} \delta_{\sigma\sigma'}. \end{aligned} \quad (2.9)$$

This expansion can then be substituted into the classical expression for other quantities. In particular, the angular momentum observables, which are now operators, have a simple form;

$$\begin{aligned} \hat{L} &= \sum l \hbar a_{l,\sigma}^\dagger a_{l,\sigma}, \\ \hat{S} &= \sum \sigma \hbar a_{l,\sigma}^\dagger a_{l,\sigma}, \\ \hat{J} &= \hat{L} + \hat{S}. \end{aligned} \quad (2.10)$$

This is just the number of photons in each mode, times the angular momentum of that mode, summed over all modes [96]. We will return to the quantum optics of angular momentum in section 2.4.

The interpretation of Eq. 2.2 as the sum of separate spin and orbital angular momentum given by Eqs. 2.3 and 2.4 has been controversial. It has been found [79] that the total orbital angular momentum can depend partly on polarisation, while the spin angular momentum can also depend on the azimuthal phase. It has also been shown that the quantum operators \hat{L} and \hat{S} are not true angular momenta as they do not retain the correct commutation relations [95].

This is a consequence of expanding the field in a set of transverse modes. Rotations that act on the field and not the coordinate basis, or vice versa, do not generally preserve this transversality. Hence only the combination $\hat{L} + \hat{S}$ corresponds to angular momentum in three dimensions [95].

2.1.2 Angular momentum in two dimensions and the paraxial approximation

To be more precise, the reason why \vec{L} and \vec{S} , and their corresponding quantum operators \hat{L} and \hat{S} , are not proper angular momenta, and the root of the difficulties with this interpretation, is that they do not generate the correct algebra, \mathfrak{so}_3 . This is the algebra of infinitesimal rotations, which generate finite rotations in three dimensions, given by the group $SO(3)$. This group can be represented by special orthogonal 3×3 matrices and is non-Abelian. These full rotations of the three-dimensional field would indeed preserve transversality. The structure of \mathfrak{so}_3 , encoded in the commutation relations Eq. 1.11, leads to a particularly constraining form of the spin-statistics theorem which classifies particles as bosons with integer spin or fermions with half-integer spin [97, 98].

The subject of angular momentum in two dimensions is considerably simpler. In two dimensions the relevant group is $SO(2)$ which is Abelian. This results in a trivial algebra which L_z and S_z do obey. It also means that particles can have an arbitrary quantum spin which need not be an integer or half-integer multiple of Planck's constant. As described in section 1.2.3, a modified form of the spin-statistics theorem relates the phase when two particles are interchanged to the fractional angular momentum. Particles with fractional angular momentum in two dimensions are called anyons [33].

Although light in general is described by a three dimensional vector field, the description of propagating beams can be simplified by considering only rays which propagate at small angles to the z-axis. The total field can be written as a plane wave times a slowly varying envelope function,

$$\vec{E}_{\text{TOT}} = \text{Re} \left[e^{i(k_z z - \omega t)} \vec{E} \right], \quad (2.11)$$

with $k_z = 2\pi/\lambda$. The field is then described by a two dimensional complex vector, e.g. $\vec{E} = (E_x, E_y)^T$ in a Cartesian basis. The Helmholtz wave equation ,

$$\left(\nabla^2 - \frac{1}{c^2} \frac{\partial^2}{\partial t^2} \right) \vec{E}_{\text{TOT}} = 0, \quad (2.12)$$

then leads to the paraxial wave equation

$$\left(\nabla_{\perp}^2 + 2ik_z \frac{\partial}{\partial z} \right) \vec{E} = 0 \quad (2.13)$$

under the approximation that

$$\left| \frac{\partial^2 \vec{E}}{\partial z^2} \right| \ll \left| k_z \frac{\partial \vec{E}}{\partial z} \right|, \quad (2.14)$$

i.e. the envelope function varies slowly compared to the wavelength of the light. The differential operator $\nabla_{\perp}^2 = d_x^2 + d_y^2$ is the transverse part of the Laplacian. Equation 2.13 is equivalent to the two dimensional Schrödinger equation with the beam axis coordinate z playing the role of time [50]. As with the Schrödinger equation, in more complex systems with inhomogeneity, anisotropy, etc. we can derive a paraxial equation similar to Eq. 2.13 but with more terms added to the Laplacian operator which describes light in free space. We have already seen one such example describing light in a biaxial medium in section 1.3.1.

The complex two-dimensional vector \vec{E} , known as the Jones vector, encodes both the phase and the polarisation of light. For example the circular polarisation states are represented by

$$|L\rangle = \begin{pmatrix} 1 \\ i \end{pmatrix}, \quad |R\rangle = \begin{pmatrix} 1 \\ -i \end{pmatrix}, \quad (2.15)$$

which according to Eq. 2.11 gives

$$\vec{E}_{\text{TOT}} = \begin{pmatrix} \cos(k_z z - \omega t) \\ \pm \sin(k_z z - \omega t) \end{pmatrix}. \quad (2.16)$$

This reduction to a two-dimensional transverse field simplifies many of the problems with interpreting angular momentum in three dimensions. In particular the quantum versions \hat{L}_z and \hat{S}_z can be considered angular momenta, since they respect the trivial algebra of \mathfrak{so}_2 . Secondly, in the paraxial picture there is a well defined beam direction, and it is natural to consider the angular momentum current across a plane perpendicular to this direction. This is defined as

$$M = \int d^2 r \epsilon_0 \left(\vec{r} \times \left[\vec{E} \times \vec{B} \right] \right) \cdot \hat{e}_z, \quad (2.17)$$

where the integral is over the x - y plane. This current has units of angular momentum per unit length along the beam axis. Because we are using the paraxial approximation, the plane wave part of the field in Eq. 2.11 depends on the combination $z - ct$, and it can be shown that the angular momentum per unit time is simply given by cM [42].

It can be shown [92, 42] that in the paraxial approximation the angular momentum currents can be written as

$$M^L = \text{Re} \left[\frac{\epsilon_0 c}{2\omega} \int d^2 r \vec{E}^* \cdot \left(-i \frac{d}{d\phi} \right) \vec{E} \right], \quad (2.18)$$

$$M^S = \text{Re} \left[\frac{\epsilon_0 c}{2\omega} \int d^2 r \vec{E}^* \sigma_3 \vec{E} \right], \quad (2.19)$$

where in Eq. 2.19 we write \vec{E} in a circular polarisation basis. When M is written as $M^L + M^S$ the current separates into components which depend only on the polarisation and the orbital structure of the beam respectively [42].

The total angular momentum current in a beam with a particular phase or polarisation profile will depend on the total intensity of the beam. We can normalise Eq. 2.19 by the total energy flux to give the angular momentum per unit energy. Furthermore, multiplying this quantity by $\hbar\omega$ gives the average angular momentum per photon;

$$J = L + S = \text{Re} \frac{\hbar \int d^2r \vec{E}^* \cdot (-id_\phi + \sigma_3) \vec{E}}{\int d^2r \vec{E}^* \cdot \vec{E}}. \quad (2.20)$$

It should be kept in mind however, that despite the appearance of \hbar this is a purely classical result.

2.1.3 Operators and eigenfunctions

As the two-dimensional transverse field transforms under the Abelian rotation group $SO(2)$, we wish to explore the possible form of the total angular momentum operator for photons in a paraxial beam of light, specified by a two component complex vector field \vec{E} . We take circularly polarised states as our basis and use polar coordinates (r, ϕ) across the beam. The angular momentum operators involve the infinitesimal generators of rotations that act on this field. They include [92] the third Pauli matrix $S_z = \hbar\sigma_3$, which rotates the polarisation direction homogeneously across the beam, and the usual orbital form $L_z = -i\hbar I(d/d\phi)$, which rotates the beam profile but leaves polarisation unchanged (note σ_3 is the equivalent in a circular polarisation basis of σ_2 in a Cartesian one).

To show that these are the operators which generate rotations, consider infinitesimal rotations of the field [92, 40]. The orbital operator follows from

$$\vec{E}(\phi) \rightarrow \vec{E}(\phi + \delta\phi), \quad (2.21)$$

$$\approx \vec{E} + \delta\phi \frac{d\vec{E}}{d\phi}, \quad (2.22)$$

$$= \left(1 + \delta\phi \frac{d}{d\phi}\right) \vec{E}, \quad (2.23)$$

so that

$$L = -i\hbar \frac{d}{d\phi}. \quad (2.24)$$

The spin operator follows on considering rotations of the polarisation vectors. In

the Cartesian basis of linear polarisations, $\vec{E} = (E_x, E_y)^T$, we have

$$\begin{aligned}\vec{E} &\rightarrow \begin{pmatrix} \cos(\delta\phi) & \sin(\delta\phi) \\ -\sin(\delta\phi) & \cos(\delta\phi) \end{pmatrix} \vec{E}, \\ &\approx \begin{pmatrix} 1 & \delta\phi \\ -\delta\phi & 1 \end{pmatrix} \vec{E}, \\ &= (I + i\delta\phi\sigma_2)\vec{E},\end{aligned}\tag{2.25}$$

and the spin operator is the second Pauli matrix σ_2 . This becomes σ_3 on transforming to the basis of circular polarisations. The factor i is inserted to be consistent with the usual convention relating elements of the group to the generators, i.e. $X = \exp(ix\delta\phi) \approx (1 + ix\delta\phi)$.

These operators, which form the Lie algebra of infinitesimal rotations, generate the Lie group of finite rotations through exponentiation,

$$R_L(\phi_0) = \exp(i\phi_0 L),\tag{2.26}$$

$$R_S(\phi_0) = \exp(i\phi_0 S).\tag{2.27}$$

The operators L and S are exactly those which appear in the classical expressions for the expectation value of angular momentum of a beam [92, 42] given by Eq. 2.19

$$\begin{aligned}M &= \frac{\epsilon_0 c}{2\omega} \int d^2r \vec{E}^* \left[-i \frac{d}{d\phi} + \sigma_3 \right] \vec{E} \\ &= \frac{\epsilon_0 c}{2\omega} \int d^2r \vec{E}^* [L + S] \vec{E}.\end{aligned}\tag{2.28}$$

These expressions are identical to those which describe the expectation value of a quantum operator, if we were to interpret the field E as a wave-function. This is a consequence of the identical form of the paraxial wave equation Eq. 2.13 and the two dimensional Schrödinger equation [50, 99]. However, at this stage they should be interpreted as purely classical expressions. The inherently relativistic nature of propagating light fields means they cannot be treated in a first-quantised theory.

However, the operators are clearly linked to the full second quantised expressions. Expanding the field in a complete set of eigenmodes of L and S , $\{F_{l,\sigma}\}$, and quantising leads to the quantum spin and orbital angular momentum operators [95, 96],

$$\begin{aligned}\hat{S} &= \sum_{l,\sigma} \hat{a}_{l,\sigma}^\dagger \hat{a}_{l,\sigma} \langle F_{l,\sigma} | S | F_{l,\sigma} \rangle, \\ \hat{L} &= \sum_{l,\sigma} \hat{a}_{l,\sigma}^\dagger \hat{a}_{l,\sigma} \langle F_{l,\sigma} | L | F_{l,\sigma} \rangle.\end{aligned}\tag{2.29}$$

This process leads for example to Eq. 2.10 when the fields F are Laguerre-Gauss modes. Note that here \hat{L} and \hat{S} act on the quantum state of the electromagnetic field, while L and S act on the classical mode functions [100] (the Dirac kets are

used to represent the field purely for ease of notation). In this representation each photon contributes an exact amount of both spin and orbital angular momentum. When the field is in an eigenmode of the operators then all photons will be in the same angular momentum mode and so carry an exact amount l or σ of orbital or spin angular momentum.

In this chapter we will frequently refer to beams which are symmetric under a particular rotation. By this we mean that the beam is invariant up to a phase. Conservation of an angular momentum corresponds not to a particular property of the beam, but to the invariance of the medium to such a transformation. The reasons for considering beams which are eigenstates of a particular angular momentum are two-fold. Firstly, if a particular medium respects a symmetry, then eigenstates will remain eigenstates as they propagate, while other states will be mixed. Thus, so long as the states form a complete basis, the propagation of any beam can be described by the propagation of its components in that basis, each of which simply picks up a different phase. We can also describe the effect of optical devices, etc. by their effect on each eigenmode. Secondly, although invariance of the medium guarantees the conservation of the classical expectation value, the photons in a beam which is a mode of the operator will have an exact value of that quantity, while other beams will consist of photons which are in a superposition of different states, and so do not have a well defined exact value. As the Laguerre-Gauss beams do for orbital angular momentum, the eigenmodes of a particular angular momentum give us a basis to explore the properties of that angular momentum both theoretically and experimentally.

2.1.4 Angular momentum in a conically refracted beam.

The conically refracted beam described in chapter 1 has a unique angular momentum distribution [71, 69]. Equation 1.27 shows that incoming light with circular polarisation (i.e. spin angular momentum) is converted into light with a combination of spin and orbital angular momentum,

$$\begin{pmatrix} 1 \\ \pm i \end{pmatrix} \rightarrow B_0 \begin{pmatrix} 1 \\ \pm i \end{pmatrix} + B_1 e^{\pm i\phi} \begin{pmatrix} 1 \\ \mp i \end{pmatrix}, \quad (2.30)$$

or in terms of l and s

$$|l = 0, s = \pm 1\rangle \rightarrow B_0 |l = 0, s = \pm 1\rangle + B_1 |l = \pm 1, s = \mp 1\rangle, \quad (2.31)$$

where B_0 and B_1 are given in Eq. 1.28. One component has the same spin angular momentum as the incident beam while the other component has the opposite spin angular momentum and also has orbital angular momentum $l = \pm 1$. Thus the biaxial crystal acts as a partial spin to angular momentum converter.

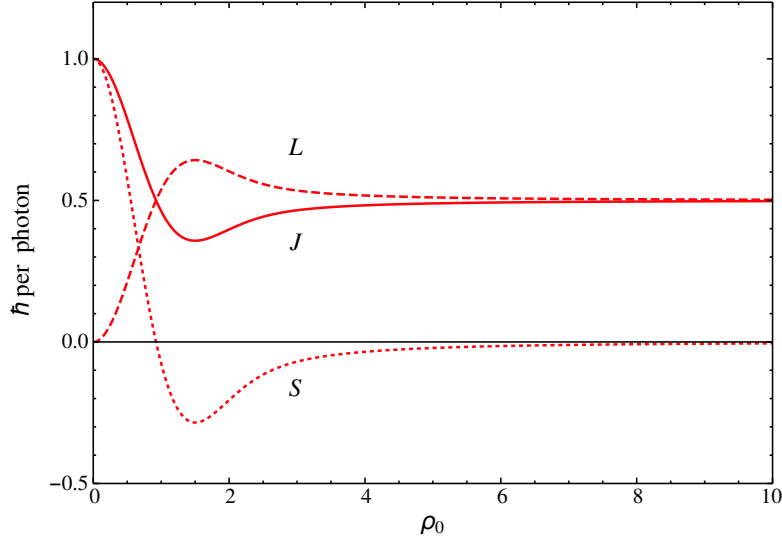


Figure 2.2: Spin, orbital and total angular momentum, per photon, of conically refracted beam as function of crystal strength parameter ρ_0 . Note fractional values are just average classical values due to beam being in a superposition of different states. Based on an identical figure in [69].

The classical spin and angular momentum current of the conical beam can be calculated using Eq. 2.20 as done in [69]. If the incoming beam has a spin angular momentum S_{inc} , i.e. it is given by $\alpha |l = 0, s = 1\rangle + \beta |l = 0, s = -1\rangle$ with $\alpha^2 - \beta^2 = S_{\text{inc}}$, then the angular momentum per photon of the conical beam, after traversing a crystal of biaxial strength $\rho_0 = Al$, is

$$L = S_{\text{inc}} \rho_0 F(\rho_0), \quad (2.32)$$

$$S = S_{\text{inc}} [1 - 2\rho_0 F(\rho_0)], \quad (2.33)$$

where $F(x) = \exp(-x^2) \int_0^x \exp(t^2) dt$ is the Dawson integral. The orbital, spin and total angular momentum of the conical beam are plotted in Fig. 2.2 as a function of the relative biaxiality $\rho_0 = Al/w$, where w is the waist of the incoming Gaussian beam.

2.2 Generalised angular momentum

2.2.1 Introduction to generalised angular momentum

As we have seen in section 2.1.1, in three dimensions the total angular momentum is given by the equal sum of spin and orbital contributions, and these components should not be considered independently. This identification of the total

angular momentum with the sum $L + S$ appears to be inevitable, following from the invariance of Maxwell's equations under arbitrary rotations [95, 87]. However, experiments usually involve beams of light propagating in a particular direction, so they are described well by the two-dimensional transverse field of the paraxial approximation. The only potential symmetries (which determine the form of the angular momentum operators according to Noether's theorem) are, in fact, rotations of this two-dimensional cross-section around the propagation direction. This restricted symmetry allows a more general form for the total angular momentum along the beam.

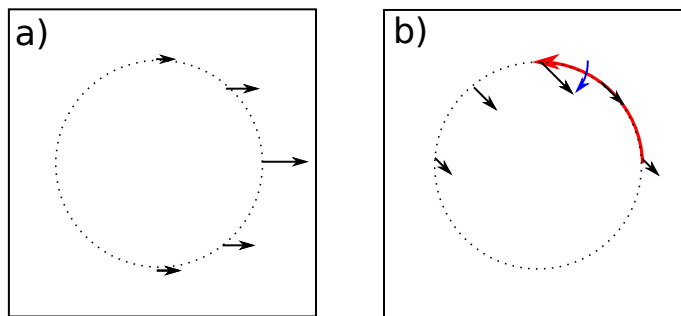


Figure 2.3: For a transverse vector field (in this case transverse to an axis coming out of the page) we can perform two types of rotation. For an example field given in a), these rotations are illustrated in b). We can rotate the intensity, for example anti-clockwise by 90° , so that the point where the field is largest moves from the far right to the top of the image (shown in red). We can simultaneously rotate the vector field at each point by an independent amount, for example clockwise by 45° (shown in blue).

This restriction allows us to consider the two types of rotation, of the image and of the vector polarisation, separately. Because the field is always transverse to the propagation direction, we can rotate it by any amount around this axis and it will still be transverse. Similarly, we can rotate the intensity of the beam around this axis without changing the direction of propagation. Not only can we consider either of these two rotations independently, but we could also consider applying a rotation of the intensity by some angle, followed by a rotation of the field by a different angle, as illustrated in Fig. 2.3. Since the rotations independently preserve the transverse nature of the field, so too will the combined rotation.

These combined rotations also, by Noether's theorem, have a conserved quantity associated with them. Because the rotation consists of separate rotations of intensity and polarisation, the conserved quantity will be a sum of the conserved angular momentum associated with each of these rotations. However, as we remarked previ-

ously, the field still needs to be invariant under a total, 360° , rotation. As we shall see, this restriction limits the combinations of spin and orbital angular momentum which are physically meaningful.

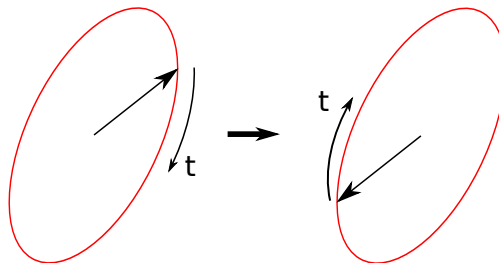


Figure 2.4: The electric field at each point traces out an ellipse as it oscillates (linear and circular polarisation are both special cases of an ellipse). This ellipse returns to itself when rotated by 180° , leaving the instantaneous electric field at a different point in its cycle.

A beam of light is composed of an oscillating electric field at each point, and so the polarisation is defined not just as a single direction that the electric field points at a given instant, but by the ellipse that the field traces out over one cycle. Linear polarisation and circular polarisation can both be viewed as the limiting cases of an ellipse. Importantly, we only have to rotate an ellipse by 180° to return to the same ellipse. Hence if we rotate the field by any multiple of 180° , we will end up with the same polarisation ellipse, and the field will simply be at a different point within the cycle around the ellipse. This is shown in Fig. 2.4. The polarisation ellipse must be rotated twice in order for the field to return to its initial state.

The fact that the field only returns to its original position when the polarisation ellipse has been rotated through two cycles is characteristic of fermions rather than the bosonic photons which make up the beam. We show that by restricting to the two-dimensional transverse field, the angular momentum of light can indeed be half-integer, emulating the demonstration of fractional quantisation of electrons discussed in the introduction. This is the first demonstration of half-integer angular momentum of light. This demonstration has a fundamental effect on how we view the relationship between quantum mechanics and paraxial optics. It also opens the door for numerous applications in quantum computing and communication which depend on the statistics of the particles used.

2.2.2 Generalised angular momentum: definition

From this point on we will be mainly concerned with these rotations around the z axis, and will therefore drop the subscript and write S and L for S_z and L_z respectively. Since these two angular momenta act independently on the two-dimensional

transverse field, we are no longer restricted to considering the equal sum $J = L + S$. We consider instead the possibility of a total angular momentum that is a more general linear combination, $J_\gamma = L + \gamma S$. Such a quantity can be defined and measured for any beam, and for any value of γ . However, it is a physically meaningful and useful quantity for beams which are invariant under the associated transformation, i.e. are eigenmodes of this operator, which will then be invariant under the generated rotation up to an overall phase.

Writing the eigenvalue equation,

$$(L + \gamma S) \vec{E} = j_\gamma \vec{E}, \quad (2.34)$$

in matrix form in a circular polarisation basis

$$\begin{pmatrix} -id_\phi + \gamma & 0 \\ 0 & -id_\phi - \gamma \end{pmatrix} \begin{pmatrix} E_l \\ E_r \end{pmatrix} = j_\gamma \begin{pmatrix} E_l \\ E_r \end{pmatrix}, \quad (2.35)$$

we find that the most general field which satisfies this equation is of the form

$$\vec{E} = \begin{pmatrix} a_1 e^{il_1 \phi} \\ a_2 e^{il_2 \phi} \end{pmatrix}, \quad (2.36)$$

where $l_1 = j_\gamma - \gamma$ and $l_2 = j_\gamma + \gamma$. Here a_1 and a_2 are arbitrary coefficients which may also have some radial dependence. Since $l_2 = l_1 + 2\gamma$, the right circular mode has $l + \gamma s = l_1 + \gamma$ while the left circular mode has $l + \gamma s = l_2 - \gamma = l_1 + \gamma$. Solving for γ and j_γ , we find

$$\gamma = (l_2 - l_1) / 2, \quad (2.37)$$

$$j_\gamma = (l_2 + l_1) / 2. \quad (2.38)$$

An eigenfield of the generators is a field which is invariant under macroscopic rotations up to a phase:

$$\begin{aligned} (L + \gamma S) \vec{E} &= j_\gamma \vec{E}, \\ \Rightarrow R_L(\phi_0) R_s(\gamma \phi_0) \vec{E} &= \exp(i j_\gamma \phi_0) \vec{E}. \end{aligned} \quad (2.39)$$

They are also associated with the classical conserved quantity through Noether's theorem: the quantity $L + \gamma S$ will be conserved in a medium which is invariant under the rotation given by Eq. 2.39. The mode Eq. 2.36 is a superposition of two components with definite spin and orbital angular momentum. However, taken together the combination is not an eigenmode of spin or orbital angular momentum, but only the combination $L + \gamma S$.

Although the eigenvalue equation is satisfied for arbitrary l_1 and l_2 , for the field to be single-valued and continuous both l_1 and l_2 must be integers. Beams with fractional average orbital angular momentum have previously been considered [101,

102], with a phase that increases by a fraction of 2π around the beam before a step discontinuity at some angle. Away from the discontinuity, such beams are locally eigenstates of the orbital angular momentum operator $d/d\phi$. However, the position of the discontinuity destroys rotational symmetry, and on propagating these beams split into integer vortices [101]. On demanding integer l , we find that γ and j_γ are either both integer, or both half-integer. The spectra of possible angular momentum operators splits, into the traditional integer valued spectrum of the operators L , S , and $L + S$, among others, and the fractional spectrum of operators such as $L + S/2$, with half-integer eigenvalues. However, it is clear from Eq. 2.36 that these beams are continuous and single-valued, and are eigenstates of $L + \gamma S$ at all points. At this point the fractional eigenvalue is a purely classical effect. As we shall see later however, the quantum operators associated with the classical angular momenta with half-integer γ also have fractional angular momentum spectra.

2.2.3 Properties and discussion

Even at a classical level, the half-integer value of an angular momentum may seem surprising. The orbital angular momentum and the spin angular momentum, when considered separately, must have integer eigenvalues so that the fields return to their original configuration after a 2π rotation. The reason that the eigenvalue Eq. 2.37 can be either half-integer or integer is because the angle of elliptical polarisation is only defined up to a π rotation, rather than a 2π one. When the polarisation ellipse is rotated by π the state is equivalent up to a phase. A scalar beam, when rotated by 2π , must pick up a phase $2\pi n$, with n an integer, to return to the same value. However, a vector field will remain unchanged so long as a combination of a polarisation rotation and a phase rotation return it to its former state. This can be accomplished by an integer number of 2π rotations of the phase and an integer number of 2π rotations of the polarisation ellipse. Alternatively a rotation of the polarisation by an odd multiple of π accompanied by a rotation of the phase by an odd multiple of π will also leave the field unchanged. Hence there is a series of generalised angular momentum quantities $L + \gamma S$ which can be divided into two discrete sets, $2\gamma = 2n$, and $2\gamma = 2n + 1$, $n \in \mathbb{Z}$. This division will have important consequences when we consider the spectrum of the associated quantum operators in subsequent sections.

Figure 2.5 illustrates this distinction by showing the polarisation profiles of several linearly polarised ring beams which have either an integer or a half-integer number of rotations of the angle of polarisation around the ring. For example, Fig. 2.5(a) shows a uniformly polarised beam. This can be described by a scalar field and must have a $2\pi n$ phase shift around a complete loop. However, Fig. 2.5(b) shows the conical beam pattern where the angle of polarisation rotates by 180° around the

loop. Clearly if we transport a field around the beam, keeping the phase constant while gradually altering the angle to keep it parallel to the local polarisation, we would return to the starting point with the field pointing in the opposite direction to the original field at that point. Hence it is necessary to have an $n\pi$ phase shift with odd n to compensate for this rotation. In Fig. 2.5(c) for comparison, the angle of polarisation rotates by 360° , and so the phase must be constant, or have a $2n\pi$ phase shift to return to the original configuration. Figure 2.5 (d) shows a further example of rotation of the polarisation by $3\pi/2$ around the beam.

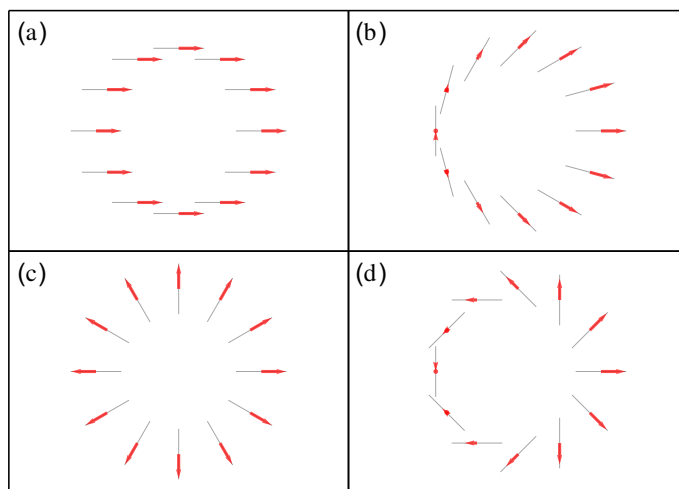


Figure 2.5: Polarisation profiles of beams with generalised angular momentum. (a) No rotation of polarisation or phase, (b) π rotation of polarisation and π phase shift (c) 2π rotation of polarisation and no phase change, (d) $3\pi/2$ rotation of polarisation and π phase change. These patterns illustrate that the polarisation may rotate by an odd as well as an even multiple of π around a beam, as long as the phase changes by a similar multiple.

The fractional offset in the generalised angular momentum spectrum is analogous to that of an electron orbiting a fractional quantum of magnetic flux. For the electron, the fractional offset arises from the Aharonov-Bohm phase accumulated over a complete orbit around the flux line [34]. The fractional offset for the photon arises due to the position dependent polarisation direction. Thus adiabatic transport around the beam involves a rotation of polarisation, introducing a Berry phase [23] equal to the fractional offset. This is most easily seen by considering the term $A\vec{p}\cdot\vec{\sigma}$ in the paraxial Hamiltonian Eq. 1.24. This can be combined with the $p^2/2$ term to rewrite the Hamiltonian as $(\vec{p} + A\vec{\sigma})^2/2 - A^2/2$, equivalent to having a magnetic vector potential in the Schrödinger equation which couples to spin.

The field Eq. 2.36 is a general solution to the eigenvalue problem Eq. 2.34. The values of the coefficients $a_{1,2}$ are arbitrary. However, when one or the other is zero then the field is an eigenstate of both orbital and spin angular momentum independently, and so is trivially an eigenstate of $L + \gamma S$ for any γ . When $a_{1,2} \neq 0$ then the field is in general elliptically polarised, and so is not an eigenstate of S . Let the field be normalised so that the intensity is $|a_1|^2 + |a_2|^2 = 1$. Then the polarisation can be described by the Stokes parameters, Q , U , and V . The degree of circular polarisation is $|a_1|^2 - |a_2|^2$ which can vary from 1 for right circular polarisation to 0 for linear polarisation and -1 for left circular polarisation. The horizontal polarisation parameter is $Q = 2|a_1||a_2| \cos(\Delta + 2\gamma\phi)$ while the diagonal polarisation parameter is $U = -2|a_1||a_2| \sin(\Delta + 2\gamma\phi)$, where $\Delta = \arg a_1 - \arg a_2$. Hence the total degree of linear polarisation is $\sqrt{Q^2 + U^2} = 2|a_1||a_2|$ which is 1 when $|a_1| = |a_2| = 1/\sqrt{2}$ and 0 when $|a_1| = 0$ or $|a_2| = 0$. Alternatively, the polarisation may be described by the angle that the major axis of the polarisation ellipse makes with the horizontal which is $\Delta/2 + \gamma\phi$. Since γ may be integer or half-integer, this illustrates that around a full circuit of a beam the polarisation can rotate by an integer multiple of π rather than 2π .

Since the Laguerre-Gauss modes are also eigenstates of $L + \gamma S$ for any γ , many properties carry over directly. For example the Laguerre-Gauss modes are themselves a complete, orthonormal basis set of solutions to the paraxial wave equation which are eigenstates of $L + \gamma S$, although there are also others which are not eigenstates of L and S independently. Thus any paraxial beam can be written as the sum of beams with definite j_γ . The Laguerre-Gauss modes are an example of such a basis, but others exist which are not eigenstates of L and S independently. The basis can be chosen to be orthonormal in the sense that $i_\gamma \neq j_\gamma \Rightarrow \langle i_\gamma | j_\gamma \rangle = 0$. The converse is not true for the Laguerre-Gauss modes, $\langle i_\gamma | j_\gamma \rangle = 0 \not\Rightarrow i_\gamma \neq j_\gamma$. The states $|l = j - \gamma, s = 1\rangle$ and $|l = j + \gamma, s = -1\rangle$ both have $l + \gamma s = j$ but are orthogonal.

2.3 Generalised angular momentum: physical effects and measurement

This formal identification of $J_\gamma \equiv L + \gamma S$ as an optical angular momentum, i.e. as a generator of a particular type of rotation, is reinforced by considering its practical consequences. Direct measurements of optical angular momentum at the single photon level have been achieved by introducing rotations of the beam (image or polarisation) into one arm of a Mach-Zehnder interferometer [78], probing the angular dependence of the field (see Fig. 2.6). Cascades of interferometers allow measurements in subspaces of dimension $d > 2$. We have extended this scheme to measuring

a generalised angular momentum, such as $L + S/2$, by rotating the polarisation by a fixed fraction of the angle of rotation of the image at each stage. In the next chapter we describe experimental measurement of the generalised angular momentum of a particular beam using this method. First however, we want to show how the generalised angular momentum in an arbitrary beam can be measured in general.

To see how we can use an interferometer to measure a generalised angular momentum in practice, consider for example a beam which is in one of two states $L + S/2 = \pm 1/2$, corresponding to

$$\vec{E}_{1/2} = (a_1, a_2 e^{i\phi})^T, \quad (2.40)$$

$$\vec{E}_{-1/2} = (a_1 e^{-i\phi}, a_2)^T, \quad (2.41)$$

respectively, in a circular polarisation basis. This beam is incident on the input beam-splitter of a Mach-Zehnder interferometer and split into two arms. The field in one arm undergoes a phase offset while the field in the other undergoes a rotation of the spatial profile by an angle ϕ_0 and of the polarisation by an angle $\phi_0/2$. This rotation is represented by the operator, given by the exponentiation of the matrix in Eq. 2.36,

$$U = \exp\left(i\phi_0 \begin{pmatrix} -id_\phi + 1/2 & 0 \\ 0 & -id_\phi - 1/2 \end{pmatrix}\right). \quad (2.42)$$

acting on the fields Eq. 2.40 and 2.41.

The fields $\vec{E}_{\pm 1/2}$ are eigenmodes of U with eigenvalues $e^{\pm i\phi_0/2}$. When the beam in each arm is recombined at the second beam-splitter the resulting field is a sum of the field from each arm. When the phase of each reflection is included the resulting field in each output port, which we label $\vec{E}_{a,b}$, are

$$\begin{aligned} \vec{E}_a &= \frac{i}{2} (e^{i\delta} + U) \vec{E}_{\pm 1/2} = \frac{i}{2} (e^{i\delta} + e^{\pm i\phi_0/2}) \vec{E}_{\pm 1/2}, \\ \vec{E}_b &= \frac{1}{2} (e^{i\delta} - U) \vec{E}_{\pm 1/2} = \frac{1}{2} (e^{i\delta} - e^{\pm i\phi_0/2}) \vec{E}_{\pm 1/2}. \end{aligned} \quad (2.43)$$

If we choose $\phi_0 = \pi$ and $\delta = \pi/2$ then it is easy to check that the resulting intensity is $I_a = 1, I_b = 0$ if the input beam is $\vec{E}_{1/2}$ and $I_a = 0, I_b = 1$ if the input beam is $\vec{E}_{-1/2}$. Furthermore, if the input is $\alpha E_{1/2} + \beta E_{-1/2}$ then the output is

$$I_a = |\alpha|^2 \quad (2.44)$$

$$I_b = |\beta|^2. \quad (2.45)$$

This is true since the field given by Eq. 2.43 is zero for one of the components at either output. Hence the result does not rely on the orthogonality of $E_{\pm 1/2}$.

Note that if the value of the generalised angular momentum of the beam were $-3/2, 5/2, 9/2, \dots$ then the eigenvalue of the operator Eq. 2.42 would still be $e^{i(4n+1)\pi/2} = e^{i\pi/2}$ and similarly if it were $-5/2, 3/2, 7/2, \dots$ the eigenvalue would

be $e^{-i\pi/2}$. Hence the beam can be split according to its projection onto a subspace of the angular momentum space, modulo a range of two, and if it contains only two components it can be filtered completely. By an appropriate choice of δ and ϕ_0 other projections are possible and so a cascade of interferometers can project each component into smaller and smaller subspaces. Hence the interferometer acts as a filter, filling the role for generalised angular momentum of a polarising beam-splitter, or a polarisation detector, for spin angular momentum.

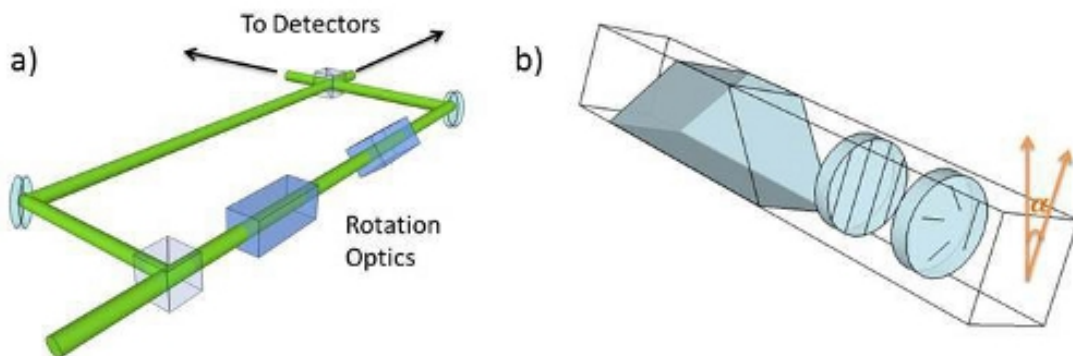


Figure 2.6: Illustration of optical sorting and manipulation of generalised angular momentum states. (a) An interferometer can act as the equivalent of a polarising beam-splitter. A rotation in one arm adds a phase to each angular momentum eigenstate, leading to destructive or constructive interference in either output port. (b) A combination of Dove prism, half-wave plate with fixed fast axis, and half-wave plate with varying fast axis can act as a half-wave plate analogue for the generalised angular momentum beam, sending $|j_\gamma\rangle$ to $| -j_\gamma\rangle$. The torque on this device is $2j_\gamma\hbar$ per photon, illustrating the mechanical reality of the generalised angular momentum. Two such devices which differ by an angle α will perform a generalised rotation of the beam by an angle 2α .

Another basic optical element, the half-wave plate also has an analogue for generalised angular momentum. A half-wave plate introduces a π phase shift between two orthogonal linear polarisations. Two half-wave plates with an angular offset rotate the polarisation by twice that angle, and hence can be used to measure spin angular momentum [78]. By using mode converters consisting of cylindrical lenses [103], or Dove prisms which reflect incoming rays about a plane parallel to their base [104], image and phase can be rotated extending the idea to orbital angular momentum. A combination of Dove prism and polarisation optics can provide a suitable analogue for the generalised angular momentum.

Consider the transmission of a beam through the composite optical element shown in Fig. 2.6(b), comprising a polarisation preserving Dove prism, a half-wave plate, and a half-wave plate with a position dependent fast axis. Such spatially varying wave plates have been considered previously [105]. The polarisation effects of Dove prisms and their compensation is described in section 3.4.2, but for now we

assume the Dove prism reflects the image with no effect on the polarisation.

The Dove prism sends $\phi \rightarrow -\phi$ while the half-wave plates have a combined Jones matrix

$$\begin{pmatrix} 0 & e^{-2i\gamma\phi} \\ e^{2i\gamma\phi} & 0 \end{pmatrix} \begin{pmatrix} 0 & 1 \\ 1 & 0 \end{pmatrix} = \begin{pmatrix} e^{-2i\gamma\phi} & 0 \\ 0 & e^{2i\gamma\phi} \end{pmatrix}. \quad (2.46)$$

This converts the original state

$$\begin{pmatrix} a_1 e^{il_1\phi} \\ a_2 e^{il_2\phi} \end{pmatrix} \xrightarrow{DP} \begin{pmatrix} a_1 e^{-il_1\phi} \\ a_2 e^{-il_2\phi} \end{pmatrix} \xrightarrow{HWPs} \begin{pmatrix} a_1 e^{-il_2\phi} \\ a_2 e^{-il_1\phi} \end{pmatrix} \equiv \begin{pmatrix} a_1 e^{l'_1\phi} \\ a_2 e^{l'_2\phi} \end{pmatrix}, \quad (2.47)$$

where we have used $\gamma = \frac{1}{2}(l_2 - l_1)$. Applying this sequence of transformations to an eigenmode of $J_{z,\gamma}$ we find that the resulting field is an eigenstate of $L + \gamma'S$ with $\gamma' = \frac{1}{2}(l'_2 - l'_1) = \frac{1}{2}(-l_1 + l_1) = \gamma$. However, the eigenvalue $j'_\gamma = \frac{1}{2}(l'_2 + l'_1) = \frac{1}{2}(-l_1 - l_2) = -j_\gamma$ is reversed.

If the device as a whole is rotated by an angle α then the reflection from the Dove prism sends $\phi \rightarrow 2\alpha - \phi$. The matrix form of the half-wave plate operator Eq. 2.46 goes to

$$U(\phi) \rightarrow R(\alpha)U(\phi - \alpha)R(-\alpha). \quad (2.48)$$

Since the matrix is diagonal in a basis of circular polarisations the rotation matrix $R(\alpha)$ has no effect. However, the angle is now measured from the new base at α , so its elements become $\exp\{\pm 2i\gamma(\phi - \alpha)\}$. The result is

$$\begin{pmatrix} a_1 e^{il_1\phi} \\ a_2 e^{il_2\phi} \end{pmatrix} \xrightarrow{DP} \begin{pmatrix} a_1 e^{il_1(2\alpha - \phi)} \\ a_2 e^{il_2(2\alpha - \phi)} \end{pmatrix} \xrightarrow{HWPs} \begin{pmatrix} a_1 e^{i(l_1+l_2)\alpha - il_2\phi} \\ a_2 e^{i(l_1+l_2)\alpha - il_1\phi} \end{pmatrix} = e^{ij_\gamma\alpha} \begin{pmatrix} a_1 e^{-il_2\phi} \\ a_2 e^{-il_1\phi} \end{pmatrix}, \quad (2.49)$$

adding an overall phase which is opposite for a j_γ state and a $-j_\gamma$ state.

The composite element, thus, plays the role for J_γ that is played by a half-wave plate for S and a Dove prism for L . As in those cases, the angle-dependent phase factor introduced into each eigenstate means that a pair of elements rotate the beam - here implementing the rotation corresponding to J_γ . As the generalised angular momentum is a property of beams whose polarisation vary with angle, it is not surprising that it requires in-homogeneous polarisation elements to act on them.

2.3.1 Mechanical effects: angular momentum and torque

The transfer of angular momentum described above results in a torque on the device, which will cause it to rotate if it is not fixed. This torque can be found by conservation of energy, using an identical argument to that presented for orbital angular momentum in [106]. As the device begins to spin, the rotational energy will come from a Doppler shift of the light beam [106, 107]. If the device is spinning at

a rate of Ω , then at time t it makes an angle Ωt , resulting in a phase shift of $e^{2ij_\gamma\Omega t}$, as in Eq. 2.49 with $\alpha = \Omega t$. This is equivalent to a Doppler shift

$$e^{i\omega t} \rightarrow e^{i\omega t} e^{2ij_\gamma\Omega t} = e^{i(\omega+2j_\gamma\Omega)t} \quad (2.50)$$

or an energy shift

$$\hbar\omega \rightarrow \hbar(\omega + 2j_\gamma\Omega). \quad (2.51)$$

The torque is given by the dependence of energy on rotational velocity

$$\tau = \frac{dE}{d\Omega} = 2\hbar j_\gamma. \quad (2.52)$$

The torque exerted on the composite element by each eigenmode, implied by the rotational Doppler shift from the phase factor $e^{ij\alpha}$, is $2\hbar j_\gamma$ per photon. Since the mode goes from j_γ to $-j_\gamma$, the torque is equal to the rate of change of the generalised angular momentum which therefore has an appropriate mechanical effect [108, 109].

2.4 Quantum fluctuations of angular momentum

2.4.1 Angular momentum operator

Having described the generalised angular momentum as a quantity associated with classical electromagnetic fields, we would now like to study quantum-mechanical properties. In particular we would like to know how much generalised angular momentum is carried by a single photon in a particular state, or more generally be able to calculate how much of any particular angular momentum is carried by a photon in any particular state. This can be done with some extension to the well established quantum theory of spin and orbital angular momentum of light, which was briefly described in section 2.1.1. Here we go through the derivation of those results more carefully and extend them to generalised angular momentum.

To study the quantum properties of beams with angular momentum, we must first expand in a complete set of modes. As J_γ is a quantity of interest, we would like to use a set of its eigenmodes. Although various choices are possible, the most convenient choice is the set of Laguerre-Gauss modes (see Eq. 2.5) which are eigenmodes of L and S individually as well as $L + \gamma S$, allowing us to compute the properties of these separate angular momentum operators using the same basis. After the field is expanded in these modes the amplitudes can be quantised via the canonical quantisation procedure.

In order to carry out this canonical quantisation we retrace the steps of the classical derivation of angular momentum, keeping track of the coefficients of the basis modes. In the paraxial approximation an arbitrary vector potential in the

Coulomb gauge can be written as [96]

$$\vec{A}(\vec{r}, t) = \sum_{l, \sigma, p} \int_0^\infty \frac{d\omega}{\sqrt{16\pi^3 \epsilon_0 c \omega}} [\vec{\epsilon}_\sigma \alpha_{l, \sigma, p}(\omega) e^{-i\omega(t-z/c)} u_{l, p}(\vec{r}_\perp, z) + \text{c.c.}], \quad (2.53)$$

where σ is the helicity, $\vec{\epsilon}_\sigma$ is the polarisation vector in the x, y plane, α is an arbitrary complex coefficient, c.c. means complex conjugate, and $u_{l, p}(r_\perp, z)$ are the Laguerre-Gauss modes described in Eq. 2.5.

The electric and magnetic fields can then be obtained from this potential. In particular the electric field in the Coulomb gauge is $\vec{E} = -\partial_t \vec{A}$. Inserting this expansion for the field into the expressions for angular momentum, Eqs. 2.4 and 2.3, and again restricting ourselves to the z components, we find the angular momentum is given in terms of the coefficients $\alpha_{l, \sigma, p}(\omega)$ by

$$\begin{aligned} S &= \epsilon_0 \int_V d^3r \vec{E}_\perp \times \vec{A}_\perp &= \sum_{l, \sigma, p} \int d\omega \sigma |\alpha_{l, \sigma, p}(\omega)|^2, \\ L &= \epsilon_0 \int_V d^3r \vec{E}_\perp \cdot (\vec{r} \times \vec{\nabla})_z \vec{A}_\perp &= \sum_{l, \sigma, p} \int d\omega l |\alpha_{l, \sigma, p}(\omega)|^2, \end{aligned} \quad (2.54)$$

where in the second equation we use $(\vec{r} \times \vec{\nabla})_z = x\partial_y - y\partial_x = \partial_\phi$. Hence the generalised angular momentum is

$$L + \gamma S = \sum_{l, \sigma, p} \int d\omega (l + \gamma\sigma) |\alpha_{l, \sigma, p}(\omega)|^2. \quad (2.55)$$

To calculate the flux of angular momentum we can use the results of Barnett [42] and the expressions given in Eq. 2.19. Calculating the orbital part for example gives

$$M_L = \iint d\omega d\omega' \frac{l}{2\pi} \frac{\sqrt{\omega\omega'}}{\omega_0} \alpha_{l, \sigma, p}(\omega) \alpha_{l, \sigma, p}^*(\omega') e^{-i\omega(t-z/c)} e^{i\omega'(t-z/c)}. \quad (2.56)$$

This can be simplified by defining the Fourier transform coefficients

$$\tilde{\alpha}_{l, \sigma, p}(t) = \frac{1}{\sqrt{2\pi}} \int_{-\infty}^\infty d\omega \alpha_{l, \sigma, p}(\omega) e^{-i\omega t}. \quad (2.57)$$

The angular momentum flux can be rewritten

$$M_S = \sum_{l, \sigma, p} \sigma |\tilde{\alpha}_{l, \sigma, p}(t - z/c)|^2, \quad (2.58)$$

$$M_L = \sum_{l, \sigma, p} l |\tilde{\alpha}_{l, \sigma, p}(t - z/c)|^2, \quad (2.59)$$

and again as expected the flux in the generalised angular momentum is simply

$$M_\gamma = \sum_{l, \sigma, p} (l + \gamma\sigma) |\tilde{\alpha}_{l, \sigma, p}(t - z/c)|^2. \quad (2.60)$$

All these results can be quantised by promoting the coefficients to operators, either in the time or frequency domains, with canonical commutation relations.

$$\alpha_{l,\sigma,p}(\omega) \rightarrow \sqrt{\hbar} \hat{\alpha}_{l,\sigma,p}(\omega), \quad (2.61)$$

$$\left[\hat{\alpha}_{l,\sigma,p}(\omega), \hat{\alpha}_{l',\sigma',p'}^\dagger(\omega') \right] = \delta_{\sigma,\sigma'} \delta_{l,l'} \delta_{p,p'} \delta(\omega - \omega'). \quad (2.62)$$

The angular momentum can then be written by replacing the classical fields with operators and normal ordering. As the plane $z = 0$ is arbitrary, we replace $t - z/c$ with t for the sake of compactness and find

$$\hat{S} = \sum_{l,\sigma} \hbar \sigma \int d\omega \hat{\alpha}_{l,\sigma}^\dagger(\omega) \hat{\alpha}_{l,\sigma}(\omega), \quad (2.63)$$

$$\hat{L} = \sum_{l,\sigma} \hbar l \int d\omega \hat{\alpha}_{l,\sigma}^\dagger(\omega) \hat{\alpha}_{l,\sigma}(\omega), \quad (2.64)$$

$$\hat{J}_\gamma = \sum_{l,\sigma} \hbar(l + \gamma\sigma) \int d\omega \hat{\alpha}_{l,\sigma}^\dagger(\omega) \hat{\alpha}_{l,\sigma}(\omega), \quad (2.65)$$

for the angular momentum operators, and

$$M_S(t) = \sum_{l,\sigma} \hbar \sigma \hat{\alpha}_{l,\sigma}^\dagger(t) \hat{\alpha}_{l,\sigma}(t), \quad (2.66)$$

$$M_L(t) = \sum_{l,\sigma} \hbar l \hat{\alpha}_{l,\sigma}^\dagger(t) \hat{\alpha}_{l,\sigma}(t), \quad (2.67)$$

$$M_\gamma(t) = \sum_{l,\sigma} \hbar(l + \gamma\sigma) \hat{\alpha}_{l,\sigma}^\dagger(t) \hat{\alpha}_{l,\sigma}(t), \quad (2.68)$$

for the angular momentum fluxes.

The choice of Laguerre-Gauss modes has allowed us to simultaneously diagonalise the spin, orbital and generalised angular momentum operators as well as the operators corresponding to the flux of these quantities. Note that the currents are functions of time while the total angular momentum operators are integrated over frequency, or equivalently over the entire time/length of the beam.

2.4.2 Wavepacket states

Because of the commutation relation (2.62) the operator $\hat{a}^\dagger(t)\hat{a}(t)$ has a dimension of $(\text{time})^{-1}$ and represents the number of photons per unit time rather than the total number. However, the states themselves, given by $\hat{a}^\dagger(t)|0\rangle$ should be dimensionless. We may also want to describe a state which varies in time, for example a single photon whose emission has some probability distribution centred at a fixed time. These states can be constructed by taking appropriate wavepackets. The process is described in Loudon [110] and the results in this subsection are taken directly from

there. We define a wavepacket creation operator either in the time or frequency domain by

$$\hat{a}_\xi^\dagger = \int d\omega \xi(\omega) \hat{a}^\dagger(\omega) = \int dt \xi(t) \hat{a}^\dagger(t), \quad (2.69)$$

where $\xi(\omega)$ is an arbitrary function and $\xi(t)$ is its Fourier transform. Any indices carried by the operators \hat{a}^\dagger such as l and s will carry over to the wavepacket state, but for the sake of simplicity will be temporarily suppressed.

We can define the corresponding number states

$$|n_\xi\rangle = (n!)^{-1/2} \left(\hat{a}_\xi^\dagger\right)^n |0\rangle. \quad (2.70)$$

To ensure these are eigenstates of $\hat{N} = \int dt \hat{a}^\dagger \hat{a}$ with eigenvalue n , i.e. the total number of photons over all time is n , we require the following normalisation condition;

$$\int d\omega |\xi(\omega)|^2 = \int dt |\xi(t)|^2 = 1. \quad (2.71)$$

The wavepacket operators have the following useful commutation relations;

$$\left[\hat{a}_\xi, \hat{a}_\xi^\dagger\right] = 1, \quad (2.72)$$

$$\left[\hat{a}(t), \left(\hat{a}_\xi^\dagger\right)^n\right] = n\xi(t) \left(\hat{a}_\xi^\dagger\right)^{n-1}. \quad (2.73)$$

Note here that the operators in this theory will be functions of $\hat{a}(t)$ and $\hat{a}^\dagger(t)$ so will be time dependent, while the states depend on wavepacket creation operators which have already been integrated over all time. We will also need to evaluate commutators of higher powers of \hat{a}_ξ , at least in the vacuum state, using the relation

$$\langle 0 | \left[\hat{a}_\xi^n, \left(\hat{a}_\xi^\dagger\right)^m\right] | 0 \rangle = n! \delta_{m,n}. \quad (2.74)$$

Since the operators commute in pairs, if $m \neq n$ there will always be an excess of \hat{a}^\dagger 's or \hat{a} 's to eliminate the vacuum $\langle 0 |$ or $| 0 \rangle$. The result for $m = n$ is easy to prove by induction.

The coherent states are defined similarly,

$$|\alpha\rangle = \exp(\hat{a}_\alpha^\dagger - \hat{a}_\alpha), \quad (2.75)$$

where \hat{a}_α is defined as in Eq. 2.69 with $\xi(t)$ replaced with $\alpha(t)$. The reason for the different notation is that these functions have a different normalisation.

$$\int d\omega |\alpha(\omega)|^2 = \int dt |\alpha(t)|^2 = \langle n \rangle, \quad (2.76)$$

where $\langle n \rangle$ is the average total number of photons in the state. With this condition, they are eigenstates of the annihilation operator,

$$\hat{a}(t) |\alpha\rangle = \alpha(t) |\alpha\rangle, \quad (2.77)$$

and similarly in the frequency domain. The commutation relation (2.73) is still valid, but (2.72) must be replaced by

$$[\hat{a}_\alpha, \hat{a}_\alpha^\dagger] = \langle n \rangle. \quad (2.78)$$

When discrete indices, labelling the Laguerre-Gauss modes for example, are introduced equations (2.78),(2.77) and (2.73) are valid when operators share the same l and σ indices, while all operators where any of these indices are different will commute.

Note that one important case is a stationary beam from a laser with a single mode at ω_0 . In this case we can write the functions as

$$\alpha(\omega) = \sqrt{2\pi F} e^{i\theta} \delta(\omega - \omega_0), \quad (2.79)$$

$$\alpha(t) = \sqrt{F} \exp(-i\omega_0 t + i\theta), \quad (2.80)$$

where θ is the phase and F is the time independent mean photon flux.

Reintroducing the angular momentum indices, we can now construct the states which are superpositions of Laguerre-Gauss beams, but are eigenstates of J_γ . For example the conical refraction beam can be modelled by a superposition of $\sigma = 1, l = 0$ and $\sigma = -1, l = 1$ modes,

$$\hat{a}_{1/2}^\dagger \rightarrow \frac{1}{\sqrt{2}} (\hat{a}_{0,1}^\dagger + \hat{a}_{1,-1}^\dagger). \quad (2.81)$$

The general creation operator is

$$\hat{a}_{j_\gamma}^\dagger \rightarrow c_1 \hat{a}_{j_\gamma - \gamma, 1}^\dagger + c_{-1} \hat{a}_{j_\gamma + \gamma, -1}^\dagger, \quad (2.82)$$

which is the creation operator for a state with $L + \gamma S = j$. With this superposition we can construct the wavepacket operators as above,

$$\hat{a}_{\xi; j}^\dagger = \int dt \xi(t) \hat{a}_j^\dagger(t), \quad (2.83)$$

where we assume both components have the same time dependence. These operators can then be used to construct number and coherent states which describe photons in a superposition of modes with exact l and s .

2.5 Calculation of quantum fluctuations

We can now calculate the expectation value and the quantum variance of both the orbital and the generalised angular momentum, in beams which are in eigenstates of one or the other of these quantities. By doing this we can gain insight into the amounts of these angular momenta carried by each photon. In particular we will see

that for a coherent beam the limiting quantum noise due to the discrete nature of photons gives a direct way of measuring the angular momentum carried by a single photon.

The states examined consist of the number states defined in Eq. 2.70 and the coherent states defined in Eq. 2.75. These can be constructed using the creation and annihilation operators for a single Laguerre-Gauss mode or for the superposition given in Eq. 2.82. Operators such as Eq. 2.68 or their higher powers can be placed between these states to calculate the moments of the angular momentum current distribution. The commutation relations given in section 2.4.2 are used to evaluate the current expectation values in terms of the time dependent photon current; which is proportional to $\int dt |\xi(t)|^2$ or $\int dt |\alpha(t)|^2$.

With a perfect detector the current would be infinite when a photon is detected and zero otherwise. More physically reasonable results are given by considering a finite response time. To model an imperfect detector we average the current over some non-zero time T . Hence the operator which represents the measured current is

$$\hat{M}_\gamma(t) = \frac{1}{T} \int_t^{t+T} dt' \sum_{l,\sigma} \hbar(l + \gamma S) \hat{a}_{l,\sigma}^\dagger(t') \hat{a}_{l,\sigma}(t'), \quad (2.84)$$

and similarly for M_L and M_S . This operator corresponds to the rate at which photons carry generalised angular momentum through the plane $z = 0$ at a given time t .

For each term in the sum over l and σ in Eq. 2.84, the operator $\hat{a}_{l,\sigma}$ will commute with the creation operators which create the number state or the coherent state and annihilate the vacuum, unless the indices match. For example for a single photon state we will have

$$\hat{a}_{l,\sigma}(t) (c_1 \hat{a}_{j_\gamma - \gamma, 1}^\dagger + c_{-1} \hat{a}_{j_\gamma + \gamma, -1}^\dagger) |0\rangle = \xi(t) (c_1 \delta_{\sigma, 1} \delta_{l, j_\gamma - \gamma} + c_{-1} \delta_{\sigma, -1} \delta_{l, j_\gamma + \gamma}) |0\rangle, \quad (2.85)$$

and similarly for higher powers. We also require the important result that the coherent states are eigenvalues of the annihilation operators with matching indices.

$$\hat{a}_{\alpha; j_\gamma} = (c_1 \hat{a}_{j_\gamma - \gamma, 1}^\dagger + c_{-1} \hat{a}_{j_\gamma + \gamma, -1}^\dagger), \quad (2.86)$$

$$\Rightarrow \hat{a}_{l,\sigma}(t) |\alpha; j_\gamma\rangle = \alpha(t) (c_1 \delta_{s, 1} \delta_{l, j_\gamma - \gamma} + c_{-1} \delta_{s, -1} \delta_{l, j_\gamma + \gamma}) |\alpha; j_\gamma\rangle, \quad (2.87)$$

where $|\alpha; j_\gamma\rangle = \exp(\hat{a}_{\alpha; j}^\dagger - \hat{a}_{\alpha; j}) |0\rangle$ is the coherent state generated with creation operator given by Eq. 2.86 and wavepacket function $\alpha(t)$.

2.5.1 Orbital angular momentum: coherent states

Before moving on to the generalised angular momentum operator itself, we can investigate the properties of the orbital angular momentum flux when the beam

consists either of pure orbital angular momentum states, or of combinations which are eigenstates only of the generalised angular momentum. This will illustrate the expected results for the case where the photon carries an exact quanta of some observable and also serve as a point of comparison.

We start by considering a coherent state in a single mode $\hat{a}_{q,s}^\dagger$ for comparison. We find the mean,

$$\langle M_L \rangle = \langle \alpha | M_L | \alpha \rangle = \frac{1}{T} \int_t^{t+T} dt' \langle \alpha | \hbar q \hat{a}_{q,s}^\dagger(t') \hat{a}_{q,s}(t') | \alpha \rangle \quad (2.88)$$

$$= \frac{\hbar q}{T} \int_t^{t+T} dt' |\alpha(t')|^2, \quad (2.89)$$

and the second moment,

$$\langle M_L^2 \rangle = \frac{\hbar^2 q^2}{T^2} \int_t^{t+T} dt' \int_t^{t+T} dt'' \langle \alpha | \hat{a}_{q,s}^\dagger(t') \hat{a}_{q,s}(t') \hat{a}_{q,s}^\dagger(t'') \hat{a}_{q,s}(t'') | \alpha \rangle \quad (2.90)$$

$$= \frac{\hbar^2 q^2}{T^2} \left[\int_t^{t+T} dt' |\alpha(t')|^2 \right]^2 + \frac{\hbar^2 q^2}{T^2} \left[\int_t^{t+T} dt' |\alpha(t')|^2 \right], \quad (2.91)$$

where we have used the fact that the coherent states are eigenstates of the annihilation operator and the equal time commutator of the time dependent states is

$$[\hat{a}_{l,\sigma}(t), \hat{a}_{l,\sigma}^\dagger(t')] = \delta(t - t'). \quad (2.92)$$

Hence the noise power is proportional to the flux and the proportionality constant is the charge divided by the integration time.

$$(\Delta M_L)^2 = \frac{\hbar^2 q^2}{T^2} \left[\int_t^{t+T} dt' |\alpha(t')|^2 \right] = \frac{\hbar q}{T} \langle M_L \rangle. \quad (2.93)$$

This is a key feature of coherent states, and one which we shall use to measure the generalised angular momentum of a single photon: the variance of the current of some quantity is proportional to the quantum of the current carried by each particle, times the mean of the current. In particular the Fano factor [111],

$$F \equiv \frac{\Delta M^2}{\langle M \rangle} = \frac{\hbar q}{T}, \quad (2.94)$$

gives the quantum of angular momentum divided by the detection time. In this case each photon carries $q\hbar$ of orbital angular momentum current. This noise due to the discrete nature of the particles which carry the current is known as shot noise, and is a lower bound on the noise when measuring a Poissonian process [112]. Because the noise is proportional to the current, it provides a means of measuring the quantum even at relatively high photon numbers, so long as other sources of noise can be sufficiently suppressed. It is also worth noting that in this case the Fano factor does not depend on the time-dependent wavepacket, in contrast to the number states as

we will see below. As each event in a Poisson process is independent, there is no difference in the relative noise when observing over a long or a short time scale.

For the coherent states with superposition of angular momentum the method is similar. Because $\hat{a}_{1,0}$ and $\hat{a}_{-1,1}$ commute, the coherent state is an eigenstate of each of the annihilation operators, with eigenvalue $\alpha(t)/\sqrt{2}$. In addition because each term in the sum in M is proportional to l , the $l = 0$ term does not contribute. The results are as above with the substitution $q \rightarrow 1$ and $\alpha(t) \rightarrow \alpha(t)\sqrt{2}$;

$$\langle M_L \rangle = \frac{\hbar}{2T} \int_t^{t+T} dt' |\alpha(t')|^2, \quad (2.95)$$

$$\langle M_L^2 \rangle = \frac{\hbar^2}{4T^2} \left[\int_t^{t+T} dt' |\alpha(t')|^2 \right]^2 + \frac{\hbar^2}{2T^2} \left[\int_t^{t+T} dt' |\alpha(t')|^2 \right], \quad (2.96)$$

$$(\Delta M_L)^2 = \frac{\hbar^2}{2T^2} \left[\int_t^{t+T} dt' |\alpha(t')|^2 \right] = \frac{\hbar}{T} \langle M_L \rangle. \quad (2.97)$$

In this case the average orbital angular momentum current is $\hbar/2$ per photon, but the angular momentum is actually carried in units of \hbar , as the state consists of a combination of $l = 1$ and $l = 0$. This is reflected in the fact that the variance is \hbar/T times the current.

However, the result Eq. 2.97 is due to the special nature of this example where one component of the superposition has $l = 0$, so that all the current is carried by the $l = 1$ component. For a general superposition of $l = l_1, l_2$, with equal amplitudes, we find

$$\langle M_L \rangle = \frac{\hbar(l_1 + l_2)}{2T} \int_t^{t+T} dt' |\alpha(t')|^2, \quad (2.98)$$

$$\langle M_L^2 \rangle = \frac{\hbar^2(l_1^2 + l_2^2)}{4T^2} \left[\int_t^{t+T} dt' |\alpha(t')|^2 \right]^2 + \frac{\hbar^2(l_1^2 + l_2^2)}{2T^2} \left[\int_t^{t+T} dt' |\alpha(t')|^2 \right], \quad (2.99)$$

$$(\Delta M_L)^2 = \frac{\hbar^2(l_1^2 + l_2^2)}{2T^2} \left[\int_t^{t+T} dt' |\alpha(t')|^2 \right] = \frac{\hbar}{T} \frac{l_1^2 + l_2^2}{l_1 + l_2} \langle M_L \rangle. \quad (2.100)$$

This is due to the fact that the current is no longer carried in constant amounts, but in a mixture of two different units. The noise is proportional to the total power of the beam, but varying the components in the superposition will vary both the mean of the current and the Fano factor.

2.5.2 Orbital angular momentum: number states

The number states are slightly more complicated. They are not eigenstates of the operator $\hat{a}^\dagger \hat{a}$ which appears in \hat{M} but only eigenstates of this operator integrated over all time. However, Eq. 2.73 can be used together with $\hat{a}|0\rangle = 0$. We begin again with a calculation of a state with definite angular momentum q .

The average angular momentum current in this case is

$$\langle M_L \rangle = \frac{\hbar q}{n! T} \int_t^{t+T} dt' \langle 0 | \hat{a}_\xi^n \hat{a}_{q,s}^\dagger(t') \hat{a}_{q,s}(t') (a_\xi^\dagger)^n | 0 \rangle \quad (2.101)$$

$$= \frac{n\hbar q}{T} \int_t^{t+T} dt' |\xi(t')|^2 \quad (2.102)$$

$$= \frac{n\hbar q}{T} I(t), \quad (2.103)$$

where $I(t) \equiv \int dt' \xi(t')$ is the fraction of the particles that arrive from t to $t + T$, and we have used Eqs. 2.73 and 2.74. As expected the average current is just the number of particles that arrive in the detection time divided by that time, multiplied by the angular momentum of each photon.

The variance is obtained by calculating

$$\langle M_L^2 \rangle = \frac{\hbar^2}{n! T^2} \int_t^{t+T} dt' \int_t^{t+T} dt'' q^2 \langle 0 | \hat{a}_\xi^n \hat{a}_{l,\sigma}^\dagger(t') \hat{a}_{l,\sigma}(t') \hat{a}_{l,\sigma}^\dagger(t'') \hat{a}_{l,\sigma}(t'') (a_\xi^\dagger)^n | 0 \rangle \quad (2.104)$$

$$= \frac{\hbar^2}{n! T^2} \int_t^{t+T} dt' \int_t^{t+T} dt'' q^2 \langle 0 | \hat{a}_\xi^n \hat{a}_{l,\sigma}^\dagger(t') (\hat{a}_{l,\sigma}^\dagger(t'') \hat{a}_{l,\sigma}(t') + \delta(t' - t'')) \times \\ \times \hat{a}_{l,\sigma}(t'') (a_\xi^\dagger)^n | 0 \rangle \quad (2.105)$$

$$= \frac{\hbar^2 q^2 n(n-1)}{T^2} I(t)^2 + \frac{n\hbar^2 q^2}{T^2} I(t), \quad (2.106)$$

giving

$$\Delta M^2 = \frac{n\hbar^2 q^2}{T^2} I(t)(1 - I(t)). \quad (2.107)$$

The Fano factor,

$$F = \frac{\hbar q}{T} (1 - I(t)), \quad (2.108)$$

is independent of the total number of photons but depends on the distribution of the state in time through $I(t)$. The only source of noise in this case is beam-splitter noise from detecting only part of the beam. If all photons arrive in the detection time T then $I(t) = 1$ and there is no uncertainty in the angular momentum current.

For the states which are a superposition of Laguerre-Gauss modes, we can use the binomial expansion. The case for $j = 1/2$ with $l = 1, s = -1$ or $l = 0, s = 1$ will serve as an example, for other values the calculation is identical. The states can be written using the binomial expansion

$$|n_\xi\rangle = \frac{1}{\sqrt{n!}} (\hat{a}_\xi^\dagger)^n |0\rangle = \frac{1}{\sqrt{2^n n!}} (\hat{a}_{\xi 0,1}^\dagger + \hat{a}_{\xi 1,-1}^\dagger)^n |0\rangle \quad (2.109)$$

$$= \sum_k \frac{1}{\sqrt{2^n n!}} \binom{n}{k} (\hat{a}_{\xi 0,1}^\dagger)^{n-k} (\hat{a}_{\xi 1,-1}^\dagger)^k |0\rangle. \quad (2.110)$$

The result is

$$\langle M_L \rangle = \frac{\hbar}{2^n n! T} \int_t^{t+T} dt' \sum_{j,k} \binom{n}{k} \binom{j}{k} \langle 0 | \left(\hat{a}_{\xi 0,1}^{n-j} \hat{a}_{\xi 0,1}^{\dagger n-k} \right) \hat{a}_{\xi 1,-1}^j \hat{a}_{1,-1}^{\dagger}(t) \hat{a}_{1,-1}(t) \hat{a}_{\xi 1,-1}^{\dagger k} | 0 \rangle \quad (2.111)$$

$$= \frac{\hbar}{T 2^n} \int_t^{t+T} dt' |\xi(t')|^2 \sum_k k \binom{n}{k} \quad (2.112)$$

$$= \frac{n\hbar}{2T} I(T), \quad (2.113)$$

where we have again used the appropriate commutation relations as well as the identity Eq. 2.119 given below. Hence the expectation value of the current is the expected number of photons which will arrive in that time, times the average angular momentum per photon.

Now we calculate the variance in the angular momentum current. For simplicity the ξ subscript can be dropped with the understanding that any \hat{a} or \hat{a}^\dagger which does not depend on time is a wavepacket operator. A tedious but methodical application of Eqs. 2.119 to 2.121 and the commutation relations leads to

$$\langle M_L^2 \rangle = \frac{\hbar^2}{2^n n! T^2} \int_t^{t+T} dt' \int_t^{t+T} dt'' \sum_{j,k} \binom{n}{k} \binom{j}{k} \quad (2.114)$$

$$\times \langle 0 | \left(\hat{a}_{0,1}^{n-j} \hat{a}_{0,1}^{\dagger n-j} \right) \hat{a}_{1,-1}^{\dagger j} \hat{a}_{1,-1}^{\dagger}(t') \left\{ \hat{a}_{1,-1}^{\dagger}(t'') \hat{a}_{1,-1}(t'') + \delta(t' - t'') \right\} \hat{a}_{1,-1}(t'') \hat{a}_{1,-1}^{\dagger k} | 0 \rangle$$

$$= \frac{\hbar^2}{2^n T^2} I(t, T)^2 \sum_k k(k-1) \binom{n}{k} + \frac{\hbar^2}{2^n T^2} I(t, T) \sum_k k \binom{n}{k} \quad (2.115)$$

$$= \frac{\hbar^2 n(n-1)}{4T^2} I(t, T)^2 + \frac{\hbar^2 n}{2T^2} I(t, T). \quad (2.116)$$

Combining these gives

$$(\Delta M_L)^2 = \frac{n\hbar}{2T} I(t, T) \left(\frac{\hbar}{T} - \frac{\hbar}{2T} I(t, T) \right) = \langle M_L \rangle \frac{\hbar}{T} \left(1 - \frac{1}{2} I(t, T) \right). \quad (2.117)$$

In this case there are two sources of noise. As before one source comes from the fact that during the detection time only part of the beam may be measured. However, even when $I(t) = 1$ there is another source which is a result of the measurement projecting the superposition onto one of the two possible L values with equal probability. In this case the variance is

$$(\Delta M_L)^2 = \frac{\hbar}{2T} \langle M_L \rangle. \quad (2.118)$$

Of course since this is a number state and not a coherent state, the quantum of angular momentum cannot be inferred from the fractional prefactor.

Note the following identities are used above:

$$\sum_{k=0}^n \binom{n}{k} = 2^n, \quad (2.119)$$

$$\sum_{k=0}^n k \binom{n}{k} = n2^{n-1}, \quad (2.120)$$

$$\sum_{k=0}^n k^2 \binom{n}{k} = n(n+1)2^{n-2}. \quad (2.121)$$

The calculation of the mean and the variance of the spin angular momentum for various states is exactly the same, with s replacing l .

The results of this section have shown that for a number state the expectation value of the current is just the average angular momentum per photon times the average number of photons detected, as expected. The variance in the current is zero when all photons are detected and each photon carries an exact amount of the measured angular momentum. When the photon is not in an exact state additional noise is created. This is essentially beam-splitter noise; as the angular momentum is measured a projection is made onto one of the eigenstates with a 50% chance of measuring each value in the superposition. The results for coherent states from section 2.5.1 are similar, with the average angular momentum current being simply the average angular momentum per photon times the photon flux. However, the variance in this case is bounded from below by the current times the quantum of angular momentum when the beam is in an exact eigenstate. We can therefore use this noise to measure the quantum for a particular angular momentum. When the beam is in a superposition additional beam-splitter noise is added as before. These results will carry over to the generalised angular momentum operator. However, as we shall see it is the states with exact value of j_γ which minimise the variance, while those with exact l or s introduce additional noise.

2.5.3 Generalised angular momentum: number states

We now move on to calculations of the generalised angular momentum operator. As the calculations are similar to the above we will omit some details. In this case we expect to find that the half-integer expectation value should be understood as a property of a single photon, and not just as an average over photons in different states. Specifically we will show that for a coherent state with fixed generalised angular momentum, the Fano factor is equal to the eigenvalue of generalised angular momentum, j_γ , times \hbar/T , and hence $j_\gamma\hbar$ is the quantum carried by each photon.

The properties of the generalised angular momentum in a number state can be demonstrated by considering a single photon. The extension to arbitrary n is clear by comparing to the results in section 2.5.2. For a single photon in a single mode

$|l, s\rangle$ we find

$$\langle M_\gamma \rangle = \frac{\hbar}{T} j_\gamma I(t), \quad (2.122)$$

$$\langle M_\gamma^2 \rangle = \frac{\hbar^2}{T^2} j_\gamma^2 I(t), \quad (2.123)$$

where $j_\gamma = l + \gamma s$. The variance is

$$\Delta M_\gamma^2 = \frac{\hbar^2}{T^2} j_\gamma^2 I(t) (1 - I(t)) = \frac{\hbar}{T} j_\gamma (1 - I(t)) \langle M_\gamma \rangle. \quad (2.124)$$

Because the single Laguerre-Gauss modes are also eigenmodes of J_γ , no extra noise is introduced by measuring this quantity. This is in contrast to the case discussed in section 2.5.2 of measuring L for a state which is an eigenstate only of $L + \gamma S$.

We can also consider a single photon state given by

$$\frac{1}{\sqrt{2}} \left(a_{\xi;0,1}^\dagger + a_{\xi;1,-1}^\dagger \right) |0\rangle, \quad (2.125)$$

a superposition of Laguerre-Gauss modes. The time dependent operators commute with these creation operators unless the indices match:

$$a_{l,\sigma}(t') \frac{1}{\sqrt{2}} \left(a_{\xi;0,1}^\dagger + a_{\xi;1,-1}^\dagger \right) |0\rangle = \frac{1}{\sqrt{2}} (\delta_{l,0}\delta_{s,1} + \delta_{l,1}\delta_{s,-1}) |0\rangle. \quad (2.126)$$

When multiplied by the adjoint, each term contributes $(l + \gamma s)/2$ to the sum over l and s . Since there are two terms and both have equal $l + \gamma s$ this gives the same result as before;

$$\langle M_\gamma \rangle = \frac{\hbar}{T} j_\gamma I(t), \quad (2.127)$$

$$\langle M_\gamma^2 \rangle = \frac{\hbar^2}{T^2} j_\gamma^2 I(t), \quad (2.128)$$

$$\Delta M_\gamma^2 = \frac{\hbar^2}{T^2} j_\gamma^2 I(t) (1 - I(t)), \quad (2.129)$$

where now $j_\gamma = 1/2$ in this specific case, or more generally can be any integer or half-integer.

Measuring the generalised angular momentum for a number state in either a single mode, or a superposition with definite $l + \gamma s$ simply gives the average angular momentum per photon times the average photon current. In addition this quantity only has noise due to measuring some part of the beam. There is no noise introduced from the choice to measure the generalised, rather than the orbital angular momentum, and if the detection time is long enough to guarantee to detect the photon then the variance of the measurement is zero.

2.5.4 Generalised angular momentum: coherent states

To study the quantum of generalised angular momentum carried by each photon, we calculate the noise of the angular momentum current in a coherent state. This noise is bounded from below by the shot noise, and is experimentally more accessible than measuring properties of a single photon number state.

For a coherent state in a single Laguerre-Gauss mode we find for the mean and variance of the angular momentum current,

$$\langle M_\gamma \rangle = \frac{\hbar}{T} j_\gamma \int_t^{t+T} dt' |\alpha(t')|^2, \quad (2.130)$$

$$\Delta M_\gamma^2 = \frac{\hbar j_\gamma}{T} \langle M_\gamma \rangle, \quad (2.131)$$

respectively, i.e., shot noise with quantum $\hbar j_\gamma$. Again, this is because a single Laguerre-Gauss mode is also an eigenmode of $L + \gamma S$.

As the mean and variance of the generalised angular momentum is the main focus of this chapter, we will calculate it for a more general state than $|j = 1/2\rangle$. We consider a mode formed from an arbitrary superposition of Laguerre-Gauss modes with amplitudes $c_{q,s}$, and write $\hat{a}_\alpha = \sum_{q,s} c_{q,s} \hat{a}_{\alpha;q,s}$. The operators $a_{l\sigma}$ in the angular momentum flux commute with each component except the one for which $q = l$ and $s = \sigma$. Applying this to the expansion of the exponential which appears in the definition of the coherent states we find

$$a_{l,\sigma}(t') |\alpha\rangle = c_{l,\sigma} \alpha(t') |\alpha\rangle. \quad (2.132)$$

With this relation evaluating the angular momentum flux is possible. The mean is given by

$$\langle M_\gamma \rangle = \frac{\hbar}{T} \sum_{l,\sigma} \int_t^{t+T} dt' (l + \gamma\sigma) \langle \alpha | a_{l,\sigma}^\dagger(t') a_{l,\sigma}(t') | \alpha \rangle, \quad (2.133)$$

$$= \sum_{q,s} \frac{\hbar}{T} (q + \gamma s) |c_{q,s}|^2 \int_t^{t+T} dt' |\alpha(t')|^2. \quad (2.134)$$

Similarly the value of $\langle M_\gamma^2 \rangle$ is found to be

$$\langle M_\gamma^2 \rangle = \left[\sum_{q,s} \frac{\hbar}{T} (q + \gamma s) |c_{q,s}|^2 \int_t^{t+T} dt' |\alpha(t')|^2 \right]^2 + \quad (2.135)$$

$$+ \sum_{q,s} \frac{\hbar^2}{T^2} (q + \gamma s)^2 |c_{q,s}|^2 \int_t^{t+T} dt' |\alpha(t')|^2. \quad (2.136)$$

Hence we find that the normalised noise power of the general angular momentum current \hat{M}_γ , in a coherent state of such a mode, is

$$\frac{T\sigma_\gamma^2}{|\langle \hat{M}_\gamma \rangle|} = \frac{\hbar \sum (q + \gamma s)^2 |c_{q,s}|^2}{|\sum (q + \gamma s) |c_{q,s}|^2|} \geq \frac{\hbar}{2}. \quad (2.137)$$

The lower bound follows from applying triangle inequality to the denominator, and noting that for every non-zero term in the sum $q + \gamma s \geq 1/2$.

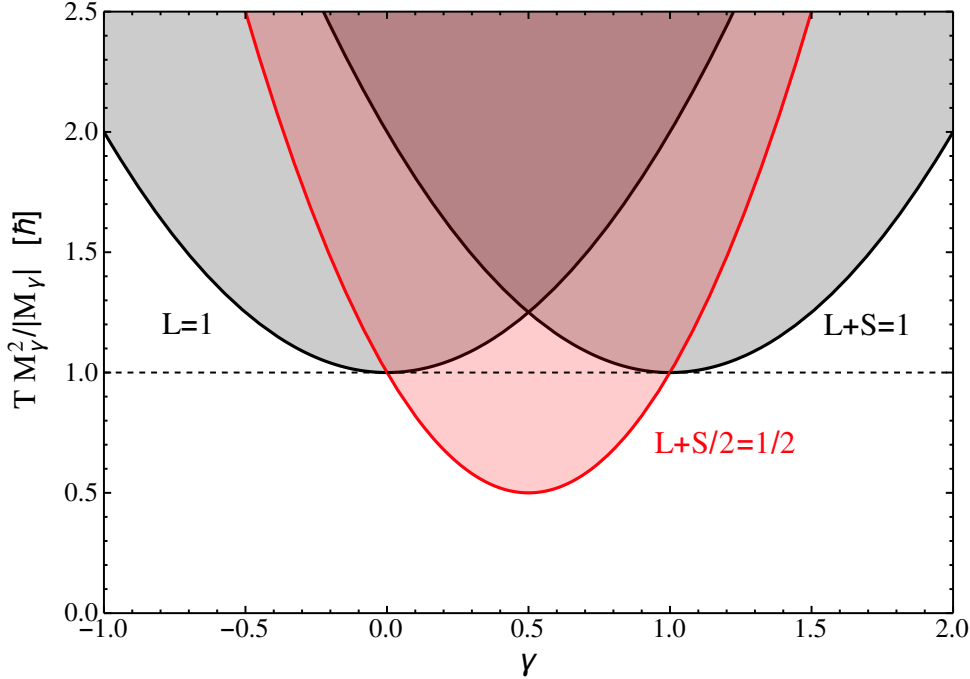


Figure 2.7: Normalised noise power in the current of the generalised angular momentum $\hat{L} + \gamma \hat{S}$ as a function of γ for various input beams, in units of \hbar . The beams are linearly polarised beams with $l = 1$, $l + s = 1$ and $l + s/2 = 1$ respectively. The shot noise is bounded from below, with a minimum of \hbar for integer angular momentum. A lower limit $\hbar/2$ can be reached for the fractional generalised angular momentum. This limit is reached for a beam which is in an exact state of the generalised angular momentum.

The Fano factor given by Eq. 2.137 is plotted in Fig. 2.7 for different beams as a function of γ . Note that this is the quantity which will be measured in the following chapter to demonstrate fractional angular momentum through a reduced bound in the shot noise. The beams considered are a generalised angular momentum eigenstate $c_1 |l = 0, s = 1\rangle + c_2 |l = 1, s = -1\rangle$ with $l + s/2 = 1/2$, a linearly polarised orbital angular momentum state $(|l = 1, s = 1\rangle + |l = 1, s = -1\rangle)/\sqrt{2}$, and a linearly polarised eigenstate of the total angular momentum $(|l = 1, s = 1\rangle + |l = 2, s = -2\rangle)/\sqrt{2}$ with $l + s = 1$. The latter two states are chosen to be linearly polarised so that they are not also eigenstates of generalised angular momentum.

The noise, Eq. 2.137, is minimised when the measured quantity corresponds to the conserved quantity of the beam. In that limit it is shot noise, from which the

quantum can be deduced. The operator J_γ has an eigenstate that is a sum of two Laguerre-Gauss modes,

$$\hat{a} = c_1 \hat{a}_{j-\gamma,1} + c_2 \hat{a}_{j+\gamma,-1}. \quad (2.138)$$

Substituting in this state the noise power is

$$\frac{T\sigma_\gamma^2}{|\langle \hat{M}_\gamma \rangle|} = \frac{\hbar j_\gamma^2 (|c_1|^2 + |c_2|^2)}{|j_\gamma| (|c_1|^2 + |c_2|^2)} \quad (2.139)$$

$$= \hbar |j_\gamma|. \quad (2.140)$$

Adding an extra term to the superposition Eq. 2.138 which takes it out of the subspace of constant j_γ will lead to additional noise above this limit. Furthermore, when γ is half-integer the minimum shot noise $\hbar/2$, achieved for beams with $j = 1/2$, is one-half of that achieved by beams with conventional, integer angular momentum.

Note that when a beam only consists of components with $j_\gamma = 0$ then Eq. 2.137 is not well defined. We do not consider these beams as they do not carry any of the angular momentum of interest. However, beams can consist of a superposition of components, some of which have $j_\gamma = 0$ and Eq. 2.137 will still apply in the limit that the amplitude of the other components approaches zero.

2.6 Quantum angular momentum operator and interferometer

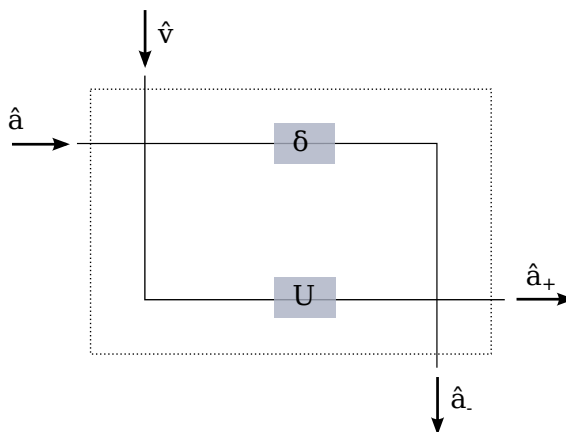


Figure 2.8: Illustration of quantum operator formalism for interferometer. The input state is described by the annihilation operator \hat{a} while the other input contains the vacuum state \hat{v} . The output of the interferometer is described by the annihilation operators at each output port, \hat{a}_+ and \hat{a}_- , which can be expressed in terms of the input state in much the same way as a classical field.

Now that we have calculated the quantum properties of the generalised angular momentum, we wish to return to the description of the interferometer given in

section 2.3, to understand how the interferometer can be used to measure these quantum properties alongside the classical value.

The calculation for a quantum field is similar to that described for the classical fields given in section 2.3. We use the input-output formalism to describe the effect of each element [110]. This formalism relates the photon creation operators which place a photon in the mode at one output of the interferometer and the creation operators for a photon at the input of the interferometer. The two output ports are labelled by $+$ and $-$, and each \hat{a} is also a vector of annihilation states for two orthogonal polarisations, depending on the choice of basis.

Following the evolution through the interferometer as before, the operators representing the quantum output from each port, labelled $+$ and $-$, are

$$\begin{aligned}\hat{a}_+ &= \frac{i}{2} (e^{i\delta} + U) \hat{a}, \\ \hat{a}_- &= \frac{1}{2} (e^{i\delta} - U) \hat{a},\end{aligned}\tag{2.141}$$

where \hat{a} represents the input field. A vacuum input state may also be included at the first beam-splitter, but does not contribute to the expectation value of normal ordered operators. The operator U encodes the effect of the Dove prisms and half-wave plates, and acts on the spin and orbital angular momentum indices of \hat{a} through

$$U a_{l,\sigma} = e^{i\phi(L+\gamma S)} a_{l,\sigma} = e^{i\phi(l+\gamma\sigma)} a_{l,\sigma}\tag{2.142}$$

in a similar way to the classical matrix used in Eq. 2.47.

Since the output of each port contains photons in an exact eigenstate, the angular momentum current is just the sum of the photon current at each port times the angular momentum of photons in that port. For an interferometer which separates the states $j_\gamma = \pm 1/2$ this is given by the operator $\hat{M} = \frac{1}{2}\hat{a}_+^\dagger \hat{a}_+ - \frac{1}{2}\hat{a}_-^\dagger \hat{a}_-$. If the input state is a superposition of modes with $l + \sigma/2 = \pm 1/2$ then this can be expressed in terms of the components of \hat{a} as

$$\hat{M} = \frac{1}{2}\hat{a}_{0,1}^\dagger \hat{a}_{0,1} + \frac{1}{2}\hat{a}_{1,-1}^\dagger \hat{a}_{1,-1} - \frac{1}{2}\hat{a}_{0,-1}^\dagger \hat{a}_{0,-1} - \frac{1}{2}\hat{a}_{-1,1}^\dagger \hat{a}_{-1,1}\tag{2.143}$$

$$= \sum_{l,\sigma} (l + \sigma/2) \hat{a}_{l,\sigma}^\dagger \hat{a}_{l,\sigma},\tag{2.144}$$

when the sum is restricted to the finite dimensional subspace in question. The operator which describes the weighted sum of the interferometer outputs is therefore equal to the generalised angular momentum operator in the finite dimensional subspace which only contains these components. Hence its mean and higher moments will all be identical, provided the input beam is contained wholly in that subspace. This method can be extended to other operators, as well as to higher dimensional subspaces, by using a cascade of interferometers and choosing the phase and rotation angle of each one correctly [78].

2.7 Conclusions

We have shown that for a paraxial beam of light the spin and orbital angular momentum can be combined not only into the conventional total angular momentum $J = L + S$, but also into a more general angular momentum $J_\gamma = L + \gamma S$ where γ is either integer or half-integer. Such an angular momentum is physically meaningful. It has a complete set of eigenmodes which are conserved under propagation in an isotropic medium. It can be filtered, measured and converted from one value to another with suitable optical elements, and produces the correct torque on the optical elements which accomplish this conversion.

Furthermore, we have shown that this generalised angular momentum can have half-integer as well as integer values per photon, not only on average, but for each photon in a coherent state, as evidenced by the calculation of the Fano factor. In the next chapter we will demonstrate this experimentally. This fractional angular momentum may be useful for communications and quantum computation. It also opens the way for experiments exploring fractional quantisation of light.

In this thesis, we considered beams close to the paraxial limit and have shown how the independence of spin and orbital angular momenta allows for a new definition of total angular momentum. However, it has recently been shown that independent spin and orbital angular momenta can be defined beyond this limit [113, 114, 115]. This immediately provides the nonparaxial generalization of the total angular momentum component J_γ , on replacing the paraxial forms for spin and orbital angular momenta, assumed here, with the nonparaxial ones. The nonparaxial spin and orbital angular momenta are independently conserved; hence, this would be a conserved quantity as well. The nonparaxial angular momenta correspond to modified forms of the rotation operators, specifically the transverse parts of those that rotate the field vectors (spin) and image (orbital) around the specified axis. The corresponding total angular momentum J_γ generates these modified rotations simultaneously, in a fixed ratio γ .

Chapter 3

Generalised angular momentum experiments: Measuring classical current and quantum noise.

3.1 Introduction

In the previous chapter we saw how a generalised angular momentum could replace the conventional total angular momentum for a paraxial beam, and examined some of the properties of this generalised angular momentum theoretically. In this chapter we report a set of experiments which explore this generalised angular momentum. We have created beams carrying varying amounts of this angular momentum using a biaxial crystal. We have constructed an interferometer which can filter these beams according to their generalised angular momentum and so measure this quantity in an arbitrary beam. A key feature of this theory is the half-integer spectrum of the operator $L + \gamma S$ when we choose a half-integer coefficient γ . In this chapter we demonstrate experimentally this fractional angular momentum by measuring a reduction in the quantum noise limit of the angular momentum current.

Previous experiments on orbital angular momentum in the quantum limit rely on single photon detection [41], or merely measure a classical average at low intensities, with an average of one photon in the detector at a time [78]. Rather than attempt to prepare and detect single photon states, the quantum of angular momentum carried by each particle can instead be read from the shot noise in the semi-classical limit [112]. This quantum shot noise is an unavoidable result of the discrete jumps in the current when a particle arrives, but can be measured from the statistical

distribution of many particles. The noise is characterised by a white noise spectrum, whose power spectral density is the product of the current and the size of the quantum. Using this method we can measure the quantum of angular momentum without using single photon sources or detectors.

This method mirrors the first direct observation of fractional charged quasi-particles, which were proposed as an explanation for the fractional quantum Hall effect [36]. The fractional charge shows up as a reduction in the quantum shot noise of a current [80] generated by backscattering from a small constriction, in order to create a Poisson distribution of charge carriers. Since photons in coherent laser light are described by a Poisson distribution the number of photons per given time interval should have a variance equal to the mean, i.e.

$$\Delta N^2 = \langle N \rangle. \quad (3.1)$$

If each photon carries an amount q of some quantity the current will be

$$M = qN \quad (3.2)$$

and so the current fluctuations are [112]

$$\Delta M^2 = q \langle M \rangle. \quad (3.3)$$

Noise below this limit has been shown in the case of amplitude squeezing, at the expense of additional phase noise [116, 117]. However, in this case we measure a reduction in the shot noise limit of an angular momentum current carried by a coherent beam of light, to confirm a fractional unit of \hbar per photon.

3.2 Angular momentum current and interferometer

As described in Chapter 2, the generalised angular momentum of a beam of light can be measured by extending the interferometric method proposed to measure the orbital, spin and total angular momentum [78]. Any angular momentum corresponds to invariance, up to a phase, under some rotation of the vector field (polarisation) and/or the image, possibly by different amounts. It can therefore be measured by performing such a rotation in one arm of a Mach-Zehnder interferometer, and comparing with the phase of the unrotated beam in the other arm. (Other interferometers, such as the Michelson interferometer, are unsuitable as most rotation optics will undo the rotation if the beam is reflected back along the same path.) If the beam is an eigenstate of the given rotation operator then the rotation results in a fixed phase, and the phase delay between the two arms can be adjusted so that the

beam interferes constructively in one of the output ports, and the beam with opposite handedness interferes destructively. The interferometer thus filters the beam according to the angular momentum, with a finite number of interferometers necessary to completely separate any beam with a finite number of components. We have already seen how such an interferometer can sort generalised angular momentum states. Now we show how the shot noise of the angular momentum current can be read experimentally from the current noise at the output of the interferometer, before describing the experimental configuration in section 3.4, and presenting the results in sections 3.5 and 3.6.

3.2.1 Shot noise and interferometer output

To measure the mean and variance in the angular momentum current, we use the interferometer as a generalised angular momentum detector, and read the mean and variance in the photocurrent from the output. The angular momentum current is

$$M = j_a I_a + j_b I_b \quad (3.4)$$

where $I_{a,b}$ is the photocurrent from output port a, b measured in photons per second, and $j_{a,b}$ is the generalised angular momentum per photon filtered into that port.

The noise in the angular momentum current is then

$$\langle M^2 \rangle - \langle M \rangle^2 = j_a^2 (\langle I_a^2 \rangle - \langle I_a \rangle^2) + j_b^2 (\langle I_b^2 \rangle - \langle I_b \rangle^2) + \quad (3.5)$$

$$+ j_a j_b (\langle I_a I_b \rangle + \langle I_b I_a \rangle - 2 \langle I_a \rangle \langle I_b \rangle) \quad (3.6)$$

$$= j_a^2 \sigma_a^2 + j_b^2 \sigma_b^2. \quad (3.7)$$

The cross terms cancel as for a coherent beam there is no correlation between the outputs, i.e.

$$\langle I_a I_b \rangle = \langle I_a \rangle \langle I_b \rangle. \quad (3.8)$$

Hence the shot noise in the angular momentum current, characterising the size of the quantum, can be found from the shot noise in the photocurrent at each output port. The Fano factor, which was theoretically calculated in Chapter 2 with the result given by Eq. 2.137, can thus be measured.

Note that in the theoretical derivations of the previous chapter we assumed that the current could be measured in full. The detector used in the experiment, described in section 3.4.3, has an imperfect quantum efficiency, meaning some fraction of the light will not be detected. This loss can be modelled as a perfect detector with a beam-splitter in front of it which has a transmission η equal to the quantum efficiency. The detected angular momentum current is

$$\frac{\hbar}{T} \int_t^{t+T} \sum_j j \hat{d}_j^\dagger(t') \hat{d}_j(t') \quad (3.9)$$

where $\hat{d}_j = \sqrt{\eta}\hat{a}_j + i\sqrt{1-\eta}\hat{v}$ is the annihilation for a photon transmitted through this imaginary beam-splitter.

Using this operator we can repeat the calculation for the shot noise in a coherent beam performed in chapter 2. For a state with two different values of j , which we can measure with a single interferometer, we find

$$\langle m \rangle = \frac{\eta\hbar}{T} (j_1 I_1 + j_2 I_2), \quad (3.10)$$

$$\langle m^2 \rangle = \frac{\eta^2\hbar^2}{T^2} (j_1 I_1 + j_2 I_2)^2 + \frac{\eta\hbar^2}{T^2} (j_1^2 I_1 + j_2^2 I_2), \quad (3.11)$$

$$\sigma_m^2 = \frac{\eta\hbar^2}{T^2} (j_1^2 I_1 + j_2^2 I_2). \quad (3.12)$$

where $j_{1,2}$ is the angular momentum carried by the first and second components and $I_{1,2}$ is the photon current in each component. The measured Fano factor

$$\frac{\sigma_m^2}{\langle m \rangle} = \frac{\hbar}{T} \frac{j_1^2 I_1 + j_2^2 I_2}{j_1 I_1 + j_2 I_2} \quad (3.13)$$

does not depend on η , and is just that expected from Eq. 2.137.

Equations 3.10 and 3.12 show that the measured current and the measured noise are both decreased by a factor η . The overall effect is equivalent to reducing the intensity of the beam. This is clear from the model we chose of a beam-splitter followed by a perfect detector. Since all the optics are linear, this beam-splitter could equally be placed before the interferometer, at the output of the laser. Since the beam is coherent, the beam-splitter will not affect the statistics of the photons, but simply decrease the overall intensity.

3.3 Varying generalised angular momentum in input beam

To produce a range of input beams with varying orbital, spin and generalised angular momentum, we use a biaxial crystal together with a range of polarisation optics. The biaxial crystal acts as a partial spin to orbital angular momentum converter as described in section 2.1.4. Consider a linearly polarised Gaussian beam passing through a quarter-wave plate at an angle $\theta + \pi/4$ to the polarisation. The resulting beam will vary between right circular, linear and left circular polarisation

$$\vec{E} = A_1 |l=0, s=1\rangle + A_2 |l=0, s=-1\rangle \quad (3.14)$$

with amplitudes

$$\begin{aligned} A_1 &= e^{i(\theta+\pi/4)} \cos \theta, \\ A_2 &= e^{-i(\theta+\pi/4)} \sin \theta. \end{aligned} \quad (3.15)$$

The circular basis states are transformed by the biaxial crystal into the half-integer general angular momentum states

$$|l, s\rangle = |0, 1\rangle \rightarrow \frac{1}{\sqrt{2}} (|1, -1\rangle + |0, 1\rangle) \equiv |1/2\rangle, \quad (3.16)$$

$$|0, -1\rangle \rightarrow \frac{1}{\sqrt{2}} (|-1, 1\rangle + |0, -1\rangle) \equiv |-1/2\rangle. \quad (3.17)$$

By varying the angle of the quarter-wave plate, we can vary the incoming beam between the two states on the left-hand side of Eq. 3.16, and hence can vary the output of the biaxial crystal between the states $|1/2\rangle$ and $|-1/2\rangle$ with coefficients given by Eq. 3.15.

These states can be used as the general angular momentum input states, or alternatively a further selection by a circular analyser is possible. For example selecting only the $s = -1$ states gives the integer orbital angular momentum states

$$|0, 1\rangle \rightarrow \frac{1}{\sqrt{2}} |1, -1\rangle, \quad (3.18)$$

$$|0, -1\rangle \rightarrow \frac{1}{\sqrt{2}} |0, -1\rangle \quad (3.19)$$

with $l = 1, 0$ respectively.

Experimental images of the orbital angular momentum components of the conical beam are shown in Fig. 3.1 in the far-field, i.e. away from the focal image plane. The Bessel-like beams are dominated by bright central lobes, so a high dynamic range image was taken and the result plotted on a log scale. The beams consist of many rings of rapidly dropping intensity. The $l = 0$ beam has a bright spike on axis while the $l = 1$ beam has a zero of intensity corresponding to the phase singularity. The orbital angular momentum of these beams has been measured previously [118]. Figure 3.2 shows a replication of these results. The distinctive fork in the wedge interference pattern of the second Bessel beam, and the spiral colinear interference pattern, confirm that this beam has orbital angular momentum $l = 1$, while the absence of these features in the first beam shows that this component carries $l = 0$.

3.4 Experimental details

3.4.1 Dove prisms

The image, i.e. the phase and the intensity of the beam, can be rotated by two Dove prisms, each of which reflects the beam about a different axis, leading to a net rotation. However, a regular Dove prism will convert linearly polarised light into an angle-dependent elliptical polarisation which is not easy to compensate for [119]. Instead we designed and built two Dove prisms based on those reported in [78], which have a fixed effect on the polarisation. The basic shape is shown in Fig. 3.3.

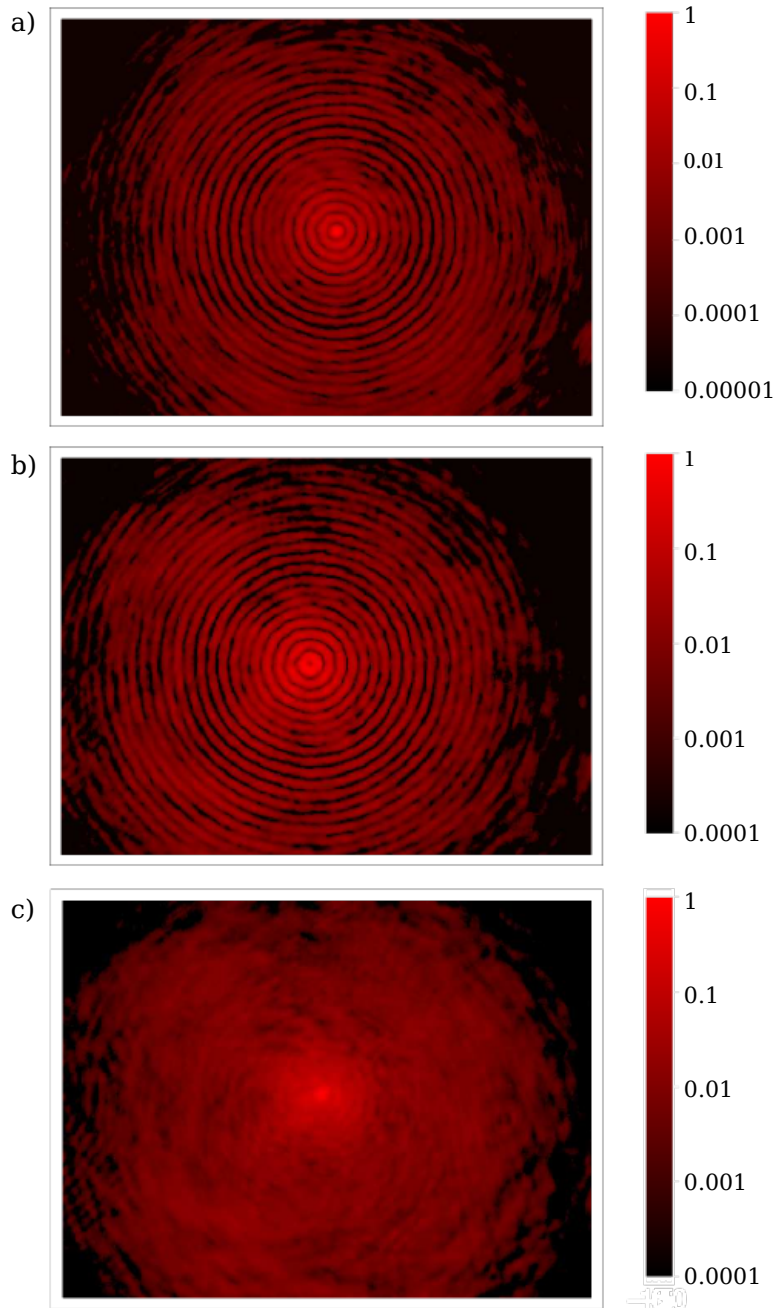


Figure 3.1: High dynamic range logarithmic images of Bessel-like components of conically refracted beam captured over a range of orders of magnitude. (a) $l = 0$ beam, (b) $l = 1$ beam and (c) superposition with $j_{1/2} = 1/2$. Intensity is plotted in arbitrary units in logarithmic scale, with highest intensity normalised to 1.

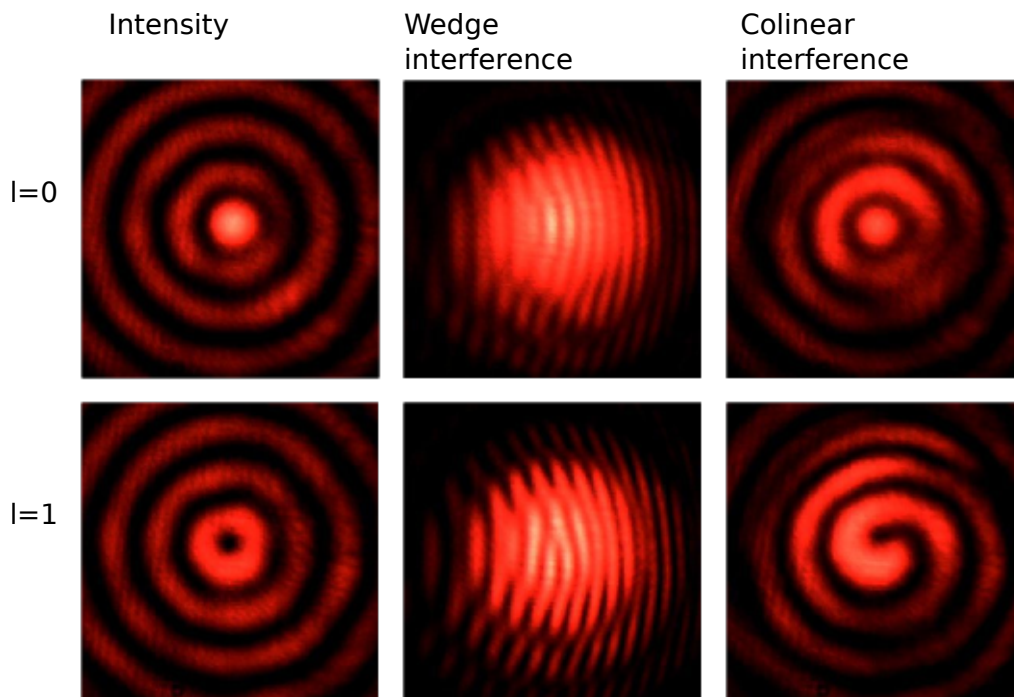


Figure 3.2: Interference patterns showing orbital angular momentum of the components of the conically refracted beam. The $l = 0$ Bessel beam has an on-axis intense spot. The wedge interference with a plane wave shows no fork dislocations. The colinear interference pattern has no spirals. This confirms that it is the $l = 0$ component. Meanwhile the orthogonal polarisation has zero intensity on-axis, consistent with a vortex carrying orbital angular momentum. The wedge interference shows a distinctive forking with an extra fringe on one side of the centre. The colinear interference shows a single spiral. All these confirm this has $l = 1$ orbital angular momentum.

An incoming ray parallel to the base of the prism undergoes three reflections, leading to an overall reflection through a plane parallel to the base. The angle of incidence of each reflection is α , $2\alpha - \pi/2$ and α respectively, where α is the top angle of the prism.

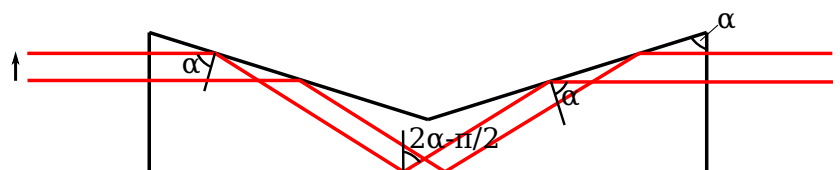


Figure 3.3: Illustration of rays passing through a fixed polarisation Dove prism. Orthogonal polarisations gain a different phase on each reflection. The angle of incidence of each reflection is proportional to the upper angle of the prism.

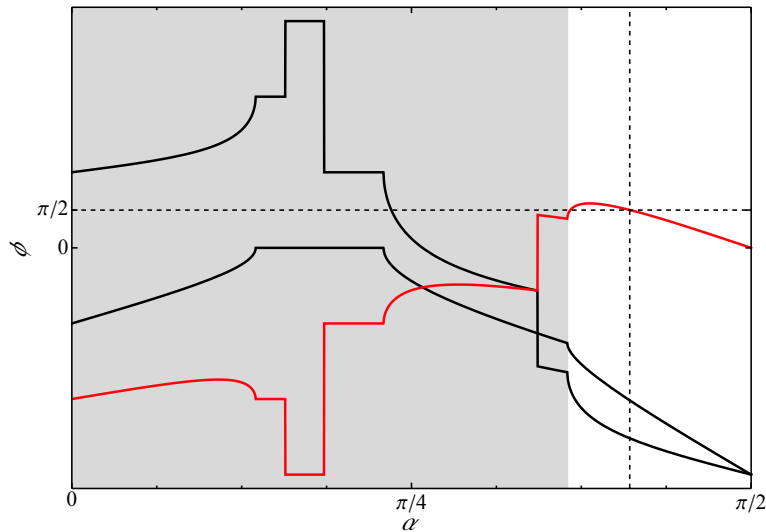


Figure 3.4: Phase of the two orthogonal polarisations (black) and the difference between them (red) due to three reflections on passing through the Dove prism, as a function of the angle of the prism. The greyed out region is where one of the angles is less than the critical angle and so reflection will not occur. The phase difference is $\pi/2$ for an angle $\alpha = 74^\circ$ for material used (crown glass with refractive index $n = 1.515$).

At each reflection the s and p polarisations have a different phase on reflection due to the complex Fresnel coefficients. This is shown in Fig. 3.4 for the specific material we used, crown glass with refractive index $n = 1.515$. The difference between the two phases is only zero when the angle is 90° . Hence it is not possible to design a prism using this geometry which has no effect on polarisation. However, the angle α can be chosen so that the total phase difference between the two polarisations, over the three reflections, is $\pi/2$. Hence the Dove prism acts as a quarter-wave plate with a fast axis perpendicular to the base. Its effect on the polarisation is thus fixed and can easily be accommodated into the beam propagation or cancelled with a quarter-wave plate with orthogonal fast axis.

3.4.2 Interferometer

The experiment was set up as shown in Fig. 3.5. Light from a Helium-Neon laser with wavelength 633 nm is passed through a Glan-Thompson polariser, and then a wavelength specific quarter-wave plate, which is mounted on a stepper motor rotation stage, to create a combination of circular polarisations (see Eqs. 3.14 to 3.15). This combination is passed through a biaxial crystal and lens (not shown) to create a collimated conical beam with the focal image plane at infinity. This beam contains

a superposition of the $|j = \pm 1/2\rangle$ states. An optional circular analyser, consisting of a quarter-wave plate and polariser, can also be inserted after the crystal to filter the integer orbital angular momentum components instead.

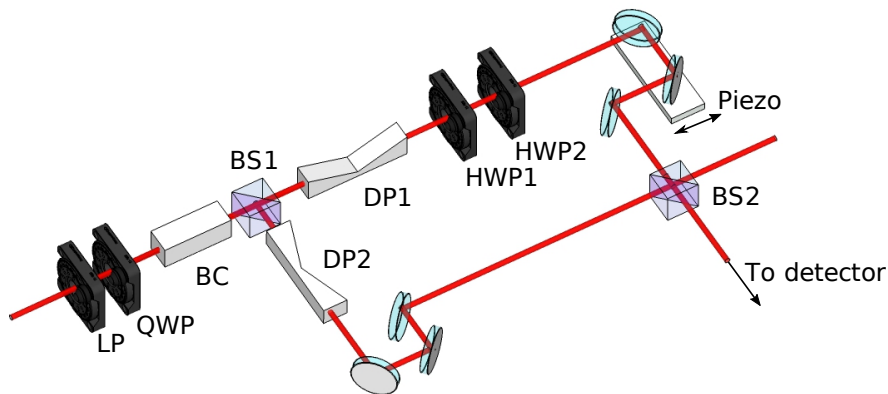


Figure 3.5: Illustration of optical sorting of generalised angular momentum states. An interferometer can act as the equivalent of a polarising beam-splitter. A relative rotation between the two arms adds a phase to each angular momentum eigenstate, leading to destructive or constructive interference in either output port. Initial beam passes through a linear polariser (LP), a quarter-wave plate (QWP), and a biaxial crystal (BC) to create a variable superposition of $|j = \pm 1/2\rangle$ states, before being split by a beamsplitter (BS1) to enter two arms of a Mach-Zehnder interferometer. The image is rotated by polarisation preserving Dove prisms (DP1) and (DP2) while the polarisation is rotated by two half-wave plates (HWP1) and (HWP2). Two mirrors on a piezo stage add a controllable phase delay. The beams are recombined at a second beam-splitter (BS2) to form constructive or destructive interference

This input beam is then incident on a 50% beam-splitter which separates it into the two arms of a Mach-Zehnder interferometer. Due to space constraints, the relative rotation is performed by placing a Dove prism in each arm, at 90° , which has the overall effect of rotating the image in one arm by 180° relative to the other. This is followed in one arm by two half-wave plates at a 45° angle, rotating the polarisation by 90° . The top arm has a pair of mirrors, acting as a delay line, on a piezo translation stage. This stage can be varied with a resolution ≈ 10 nm leading to a resolution in the path length of 20 nm. There is a similar delay line element in the second arm, on a manual translation stage, allowing for roughly equal path lengths. (This is necessary as the conical beam has some spatial evolution along the beam axis, and so the path lengths must be approximately equal for the beam profiles to overlap. The interferometer does not need to be at the zero order fringe.) If we wish to measure only the orbital or spin angular momentum, we can remove either the half-wave plates or the Dove prisms leaving either the polarisation or the image invariant respectively.

The two arms are recombined by a beam-splitter and the resulting intensity exits the interferometer into one of two output ports. The output of one port is imaged onto a CCD which is used for alignment. The output of the second port is focused onto a photodiode which is used to measure both the intensity and the noise in the photocurrent and hence the angular momentum current. The CCD and photodiode characteristics are discussed in section 3.4.3. The interferometer is aligned by choosing the input beam as one of the two components we wish to filter. The mirrors are adjusted until the wedge interference pattern disappears and the beams are both fully overlapping and fully parallel. The piezo stage is then adjusted until the input beam experiences the maximum constructive interference at one of the outputs. The interferometer is now set up to filter this component and its orthogonal partner. The input beam can then be varied and the angular momentum current, modulo the projection onto two orthogonal subspaces which the interferometer makes, can be read off as the sum of the photocurrent in each output times the angular momentum per unit photocurrent of the component which has been selected by that output.

Photographs of the exact setup are shown in Fig 3.6 with annotated laser beam path and component labels.

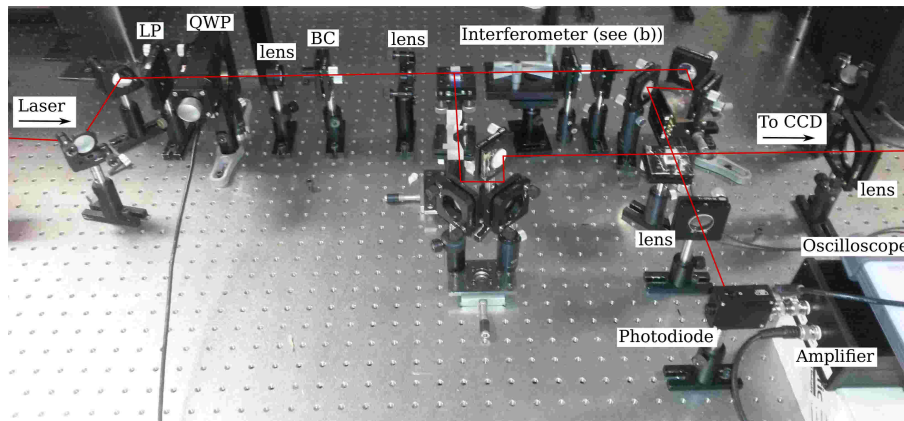
At this stage it is worth including a detailed calculation of the field in the interferometer for a particular setup, namely that to filter the generalised angular momentum $L + S/2$ into the components $j = \pm 1/2$ modulo an interval of 2 (so that one output contains $j = -1/2, 3/2, 7/2 \dots$ while the other contains $j = 1/2, 5/2, \dots$). In particular we need to account for the quarter-wave action of the Dove prisms. Consider an eigenstate $|l, s\rangle$ of orbital and spin angular momentum entering the interferometer. In the top arm an ideal Dove prism sends ϕ to $\pi - \phi$ and hence $|l, s\rangle \rightarrow e^{il\pi} |-l, s\rangle$. However, the Dove prism also creates a quarter-wave relative phase delay which sends $|R\rangle$, with $s = 1$, to $|D\rangle$, linearly polarised diagonal to the axis of the prism and $|L\rangle$, with $s = -1$, to $|A\rangle$, anti-diagonal polarisation. The two half-wave plates at 45° act on the Jones vectors through the combined matrix

$$\begin{pmatrix} 0 & 1 \\ -1 & 0 \end{pmatrix} \quad (3.20)$$

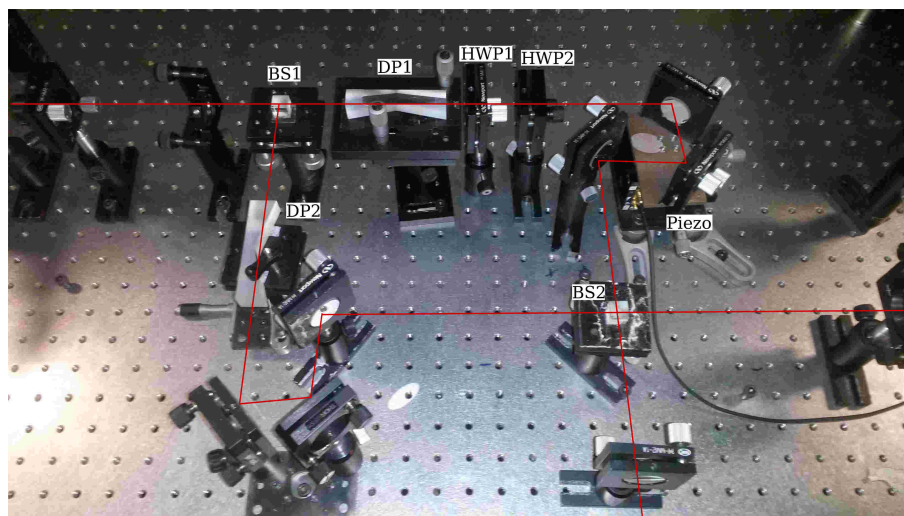
which not only adds a phase as they would to circularly polarised light but also reflects the axis of polarisation

$$|D\rangle \rightarrow |A\rangle, \quad (3.21)$$

$$|A\rangle \rightarrow -|D\rangle. \quad (3.22)$$



(a)



(b)

Figure 3.6: Photo of experimental setup with labels and indicated laser path. (a) Wide view of experiment including input beam preparation, interferometer and output ports. (b) Close-up of interferometer showing Dove prisms, wave-plates and retro-reflector stages. Labels are as explained in caption of Fig. 3.5.

The overall transformation from the elements in the top arm is thus

$$|l, 1\rangle \rightarrow e^{il\pi} |-l, A\rangle \quad (3.23)$$

$$|l, -1\rangle \rightarrow -e^{il\pi} |-l, D\rangle. \quad (3.24)$$

The light in the second arm undergoes a reflection through an axis at 90° to the original sending $\phi \rightarrow -\phi$ so $|l, s\rangle \rightarrow |-l, s\rangle$, and an equivalent quarter-wave plate at 90° which sends $|R\rangle$ to $|A\rangle$ and $|L\rangle$ to $|D\rangle$. It also picks up a phase delay $e^{i\delta}$ which includes the controlled piezo stage delay as well as a constant offset accounting for any other relative phases between the two paths due to distance, reflections etc. The overall transformation for light which traverses this arm is

$$|l, 1\rangle \rightarrow e^{i\delta} |-l, A\rangle \quad (3.25)$$

$$|l, -1\rangle \rightarrow e^{i\delta} |-l, D\rangle \quad (3.26)$$

Hence the recombined light at each output is linearly polarised in a direction depending on the input polarisation. Since the two beam-splitters each split the amplitude with a factor $1/\sqrt{2}$, the beam at one output is proportional to the sum of Eqs. 3.23 and 3.25

$$|l, 1\rangle \rightarrow \frac{1}{2} |-l, A\rangle [e^{i(l\pi-\delta)} + 1], \quad (3.27)$$

$$|l, -1\rangle \rightarrow -\frac{1}{2} |-l, D\rangle [e^{i(l\pi-\delta)} - 1]. \quad (3.28)$$

while the beam at the other output is identical, but with a δ which must differ by π due to the differing number of reflections of each beam.

The sign difference between Eqs. 3.27 and 3.28 can be accounted for by writing

$$\pm 1 = e^{i(\pi/2 \mp \pi/2)} = e^{i(\pi/2 - \sigma\pi/2)} \quad (3.29)$$

and absorbing a phase $\pi/2$ by redefining δ . The overall transformation from the input to one of the outputs is

$$|l, 1\rangle \rightarrow \frac{1}{2} |-l, A\rangle [e^{i(l\pi-\delta)} + e^{-i\sigma\pi/2}], \quad (3.30)$$

$$|l, -1\rangle \rightarrow \frac{1}{2} |-l, D\rangle [e^{i(l\pi-\delta)} + e^{-i\sigma\pi/2}]. \quad (3.31)$$

Hence regardless of the final polarisation the intensity of the output is

$$|E|^2 = \cos^2 \left(\frac{1}{2} ([l + \sigma/2] \pi - \delta) \right). \quad (3.32)$$

By choosing $\delta = \pi/2$, we thus have full transmission when $l + \sigma/2 = 1/2, 5/2, \dots$ and full reflection when $l + \sigma/2 = -1/2, 3/2, \dots$. The fractional eigenstates consist of two components $|l, 1\rangle$ and $|l + 1, -1\rangle$ which are orthogonal, and hence pass through the interferometer independently. Hence at the output both components of $j = 1/2$ are transmitted and both components of $j = -1/2$ are reflected. Choosing $\delta = -\pi/2$ reverses this selection.

3.4.3 CCD and photodiode

The results presented in this chapter were measured using two devices, a CCD and a photodiode. The photodiode, a Thorlabs DET10A silicon photodiode, was chosen due to its large bandwidth, allowing a range of frequencies to be measured, and its low noise equivalent power, meaning it should be possible to distinguish the small shot noise from the background dark noise. The rise time is 9 ns allowing high frequency measurement. The silicon material allows a large response over the visible range with a responsivity at 633 nm of 0.39 A W^{-1} corresponding to a high quantum efficiency of 0.77.

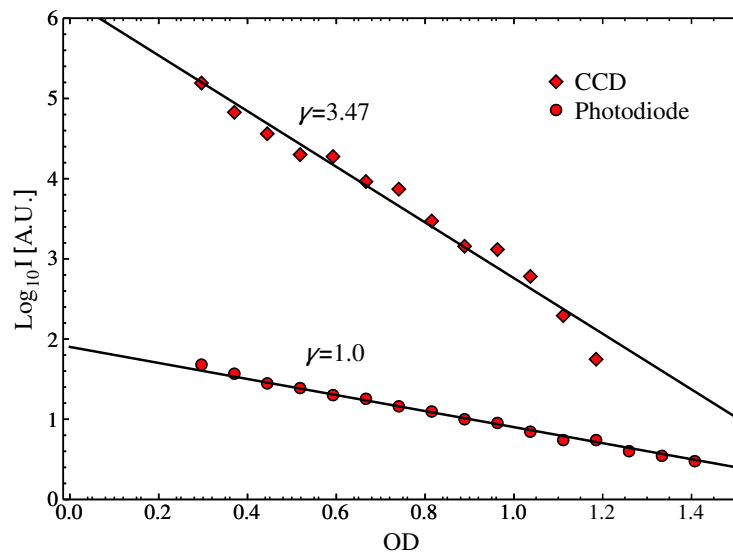


Figure 3.7: Scaling of the intensity measured by the CCD and the photodiode as a function of optical density on a log scale. Both measurements show power law scaling with power γ given by the negative of the slope. The CCD is not linear but the photodiode is to a high degree.

The photodiode is operated under a reverse bias of 10 V. This bias increases the width of the depletion region of the diode, thereby decreasing the junction capacitance and increasing the bandwidth.

The photodiode is the main source of quantitative measurements in this section. However, a 640×480 pixel colour CCD was also used for imaging the output beam. The linearity of the CCD and photodiode was measured by shining laser light through a series of neutral density filters of known optical density, with the intensity of the CCD image extracted by simply summing the value of all pixels. The results are plotted on a log scale in Fig. 3.7. Since the intensity is $I = I_0 10^{-OD}$, the measured intensity, with a non-linear response to the power γ , will be $I^\gamma = (I_0)^\gamma 10^{-\gamma OD}$. Hence the negative of the slope of each line gives γ . The slope shows that the response of the CCD is proportional to $\approx I^3$ while the photodiode is linear to a good approximation.

3.4.4 Amplifier design

The signal from the photodiode consists of a DC current, proportional to the intensity of the light, and an AC current which contains the shot noise component, as well as classical noise in the light and electronic noise from the photodiode. Because the photodiode acts as a current source, and because the shot noise is small,

an amplifier is necessary to convert the incoming current to a voltage which could be read on an oscilloscope or spectrum analyser.

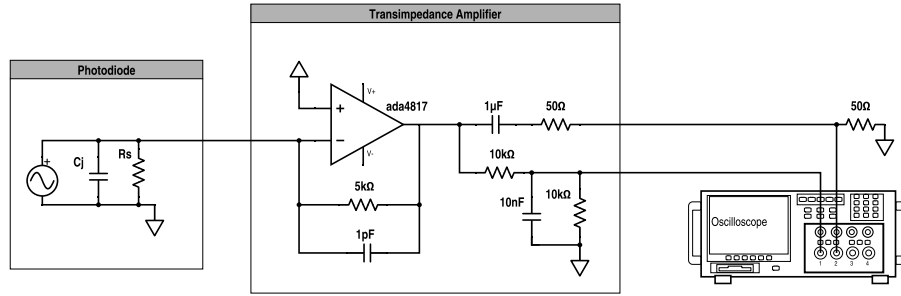


Figure 3.8: Schematic of the electronic equivalent circuit of the photodiode and the designed transimpedance amplifier with AC and DC output to oscilloscope.

For design purposes, the photodiode was taken to be an ideal current source in parallel with a fixed junction capacitance and a large shunt resistance. The designed transimpedance amplifier, shown in Fig. 3.8, converts the current to a voltage large enough to measure. This amplifier consists of two parts, an op-amp with feedback to convert the current to a voltage and an additional RC circuit to split the signal into AC and DC parts which can again be measured separately. The input from the photodiode is connected to the inverting input of the op-amp, with a $5.1\text{ k}\Omega$ feedback resistor and a 1 pF feedback capacitor to smooth the response.

The output from the op-amp is split into two parts. The DC signal is measured across the second of two $10\text{ k}\Omega$ resistors in series, with a 10 nF capacitor in parallel with the second one. This allows any AC signal a path to ground while also ensuring that any noise introduced by the measuring device does not couple back to the AC branch. The AC signal meanwhile is passed through a $1\text{ }\mu\text{F}$ capacitor and a $50\text{ }\Omega$ resistor in series. This filters any remaining DC signal and matches the impedance to a $50\text{ }\Omega$ input. The $50\text{ }\Omega$ termination leads to a nominal transimpedance of $2550\text{ }\Omega$. This setup allows the DC and AC signals to be measured separately, for example on a multimeter and a spectrum analyser. In the experiment presented here however, both signals were measured on different channels of a digital oscilloscope. The AC signal was terminated by a $50\text{ }\Omega$ resistor to match the output impedance of the amplifier.

The amplifier was simulated using LTSpice, a freeware spice simulator for electronic circuit design [120]. Figure 3.9(a) shows the result of a small signal AC analysis for the transimpedance amplifier. This shows that the transimpedance is $2550\text{ }\Omega$ over a large range of frequencies. The AC output has a band-pass behaviour with 3 dB points at approximately 1.6 kHz and 22.4 MHz allowing amplification of a broad spectrum. Fig. 3.9(b) shows the predicted electronic noise from the transimpedance amplifier over the same range. The noise is a constant $4.8\text{ nV}/\sqrt{\text{Hz}}$ below a few MHz before rising at higher frequencies, as expected for a transimpedance amplifier.

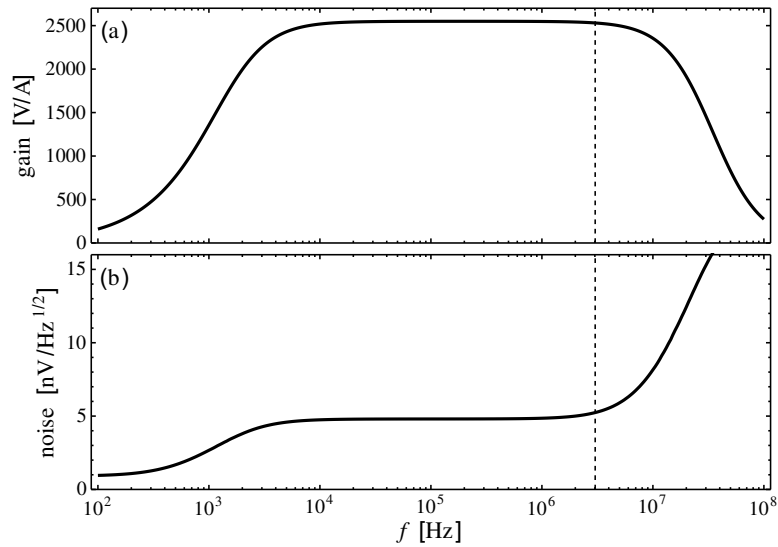


Figure 3.9: (a) Transimpedance gain as a function of frequency for AC signals showing constant transimpedance of 2550Ω over a large bandwidth. (b) Predicted noise from transimpedance amplifier as a function of frequency, which is constant below ~ 10 MHz. The dashed line is at 3 MHz where the experiment was performed,

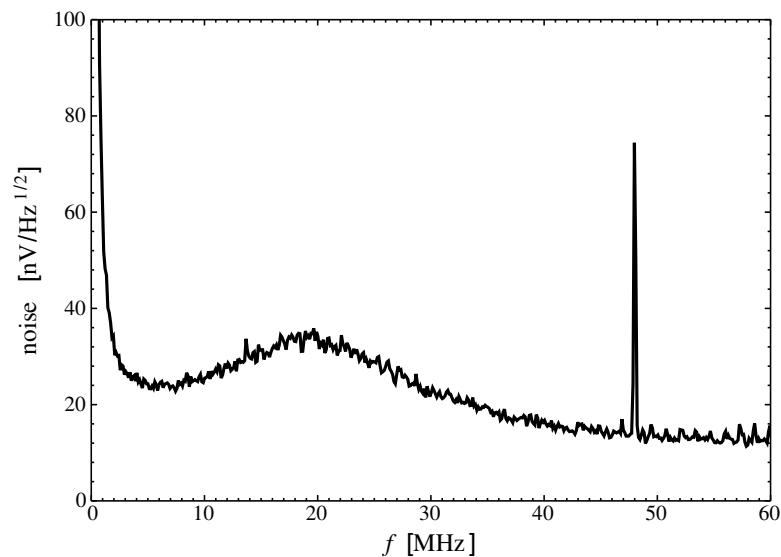


Figure 3.10: Measured background noise of transimpedance amplifier. The noise shows the transimpedance peak at ~ 10 MHz before falling due to filtering at higher frequencies. There is also electronic noise at low frequencies. However, there is a range of low noise over the range of 2 to 8 MHz.

The measured background noise from the transimpedance amplifier is shown in Fig. 3.10. Although it is higher than predicted it is within the same range of several nanovolts per root hertz. Above ≈ 5 MHz the noise rises as expected resulting in the transimpedance peak. However, due to additional filtering of higher frequencies in the circuit the noise rolls off above ≈ 20 MHz. There is a level, reasonably low noise floor of $\approx 25 \text{ nV}/\sqrt{\text{Hz}}$ around 3 MHz where we measure the spectrum.

3.4.5 Measuring shot noise

The shot noise was measured by taking a time series of voltages from the output of the amplifier, and performing a fast Fourier transform to convert to a spectrum, or periodogram. This spectrum contains several different contributions. We wish to measure the quantum shot noise, the unavoidable noise due to the discrete quanta carried by each photon. Most of the power of the spectrum comes from classical noise. This is from a variety of sources, predominantly the power supply of the laser. This is mainly found in certain regions of the spectrum, in our case usually < 1 MHz, so it can be avoided by measuring at a higher frequency. In addition this also eliminates other classical so-called pink or $1/f$ noise, which is inversely proportional to frequency. There can also be isolated noise features from the laser at higher frequencies, so a band must be chosen that is relatively noise free on a case by case basis. The noise spectrum of the He-Ne laser used is shown in Fig 3.11 showing the large peaks at low frequency followed by a constant, frequency independent spectrum at the quantum noise limit.

After the light is detected from the photodiode, there is an additional input of noise, the dark noise of the photodiode. This is noise generated by the internal circuit of the photodiode, and is present even when there is no incident light. However, for optical powers of a few milliwatts this is not significant. Finally the current from the photodiode is passed through the transimpedance amplifier. This amplifies all the previous noise, so the shot noise must be the largest part before this stage. However, it also adds additional amplifier noise, as discussed previously. Comparing Figs. 3.10 and 3.11, we see that there is a range between the low frequency classical noise in the laser spectrum and the transimpedance peak in the background noise of the amplifier. To measure the quantum noise in the signal we choose a frequency of 3 MHz which avoids classical noise, has a low background of electronic noise, and is not excessively filtered at any stage of the amplification and measurement.

The output of the amplifier is connected to a USB digital oscilloscope (Picoscope 5242A), with the DC and AC measured on separate channels. The scope used has 16 bit resolution allowing for accurate sampling, plus a 60 MHz bandwidth and a high sampling rate for high frequency resolution. The oscilloscope is controlled by a PC running LABVIEW 2012, which also controls the CCD and the rotation stage

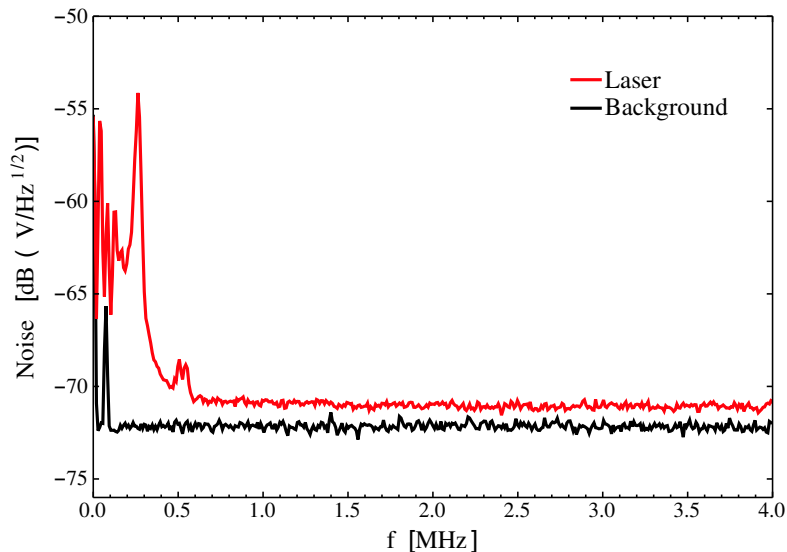


Figure 3.11: Measured spectrum of output directly from He-Ne laser at 1 mW. The spectrum is dominated by classical noise below ≈ 1 MHz. Above this the main contribution is shot noise, which is frequency independent. The noise is shown in logarithmic power units referenced to $1 \text{ V}/\sqrt{\text{Hz}}$. (Note the background noise density is higher than that shown in Fig. 3.11 due to aliasing of the transimpedance peak at higher frequencies.)

holding the quarter-wave plate which controls the input beam. For each angle of the quarter-wave plate the oscilloscope records $1024 \times N$ points in time, with a sampling rate of 125 MHz equivalent to a time per sample of 8 ns. Here N is the desired number of spectra to average over, normally 1000. Each spectra hence comprised $1024 = 2^{10}$ samples. Because the fast Fourier transform comprises positive and negative frequencies, the resulting power spectrum has 512 frequency bins with a resolution of 122 kHz and a Nyquist frequency of 62.5 MHz. Although a window function is not necessary to measure the white noise itself, there are very large peaks in the laser spectrum at low frequency which can leak across the spectrum. Hence a Hanning window function was used. This has a noise equivalent bandwidth equal to 1.5 times the actual bandwidth. The component closest to 3 MHz is selected during run time and the rest of the spectrum is discarded. The average DC voltage over the same time is also calculated and saved. The electronic noise, with no light falling on the detector, is also recorded and subtracted from the measured noise.

3.5 Classical results

3.5.1 Spin and orbital angular momentum

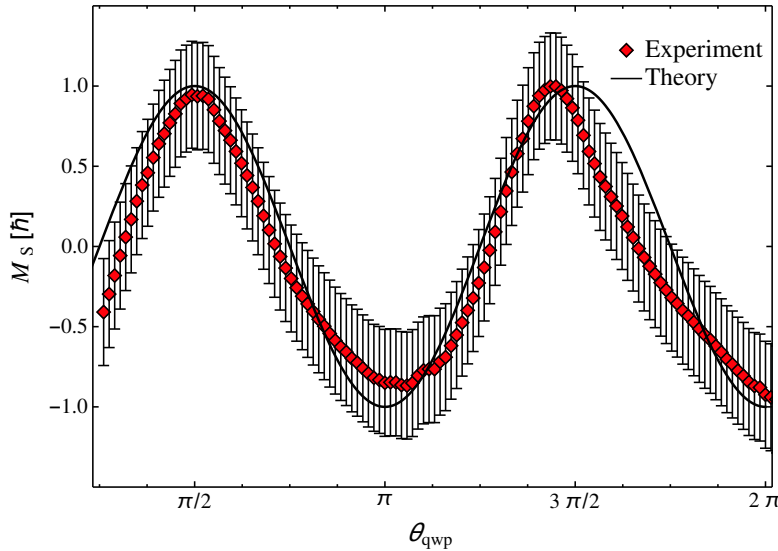


Figure 3.12: Average spin angular momentum current per photon, as measured by interferometer as function of quarter-wave plate angle as the input beam varies between right and left circular polarisation.

To test the interferometer we first demonstrate filtering according to the known spin and orbital angular momentum of light. Firstly we proceed with no biaxial crystal, but simply an input beam which is first linearly polarised, and then passes through a varying quarter-wave plate. The resulting beam varies between right and left circular polarisation according to Eq. 3.15 as the quarter-wave plate is rotated. The measured spin angular momentum current is shown in Fig. 3.12. In this case the angular momentum current $M = \hbar(I_1 - I_2)/e$, where $I_{1,2}$ is the photocurrent (in amps) measured at the first and second output. Only the output from one port of the interferometer is measured in practice. However, as the total power is constant, the output of the other port can be calculated as $I_2 = I_0 - I_1$ where I_0 is the photocurrent corresponding to total power. The average angular momentum current per photon is therefore $\hbar(I_1 - I_2)/I_0$.

The visibility of the interference pattern

$$v = \frac{I_{\max} - I_{\min}}{I_{\max} + I_{\min}}, \quad (3.33)$$

a measure of the quality of the interference pattern, is 99.8%. The error bars are discussed in more detail in Sec. 3.7. However, the main source in this case

is vibrations in the interferometer, particularly in the piezo stage controlling the relative phase delay, which does not have any feedback. Since this is a replication of well understood results [78] we did not fully optimise the interferometer in this configuration. Nevertheless we can clearly see the spin angular momentum vary between 1 and -1 in units of \hbar as the quarter-wave plate is rotated.

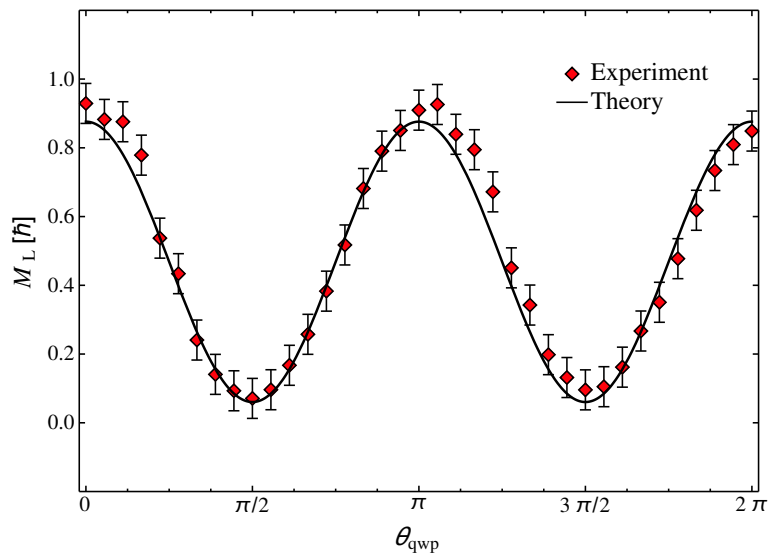


Figure 3.13: Measured orbital angular momentum current as function of the quarter-wave plate angle controlling the input beam. The angular momentum varies between zero and \hbar per photon as the input beam is varied.

The next quantity which we wish to investigate is orbital angular momentum. A beam was prepared by aligning the biaxial crystal so that the input beam undergoes conical diffraction, resulting in a superposition of different spin and orbital angular momentum modes. The resulting beam is passed through a circular polarisation analyser, selecting e.g. the left circular polarisation. This leaves the input beam consisting of two identically polarised components, one with no orbital angular momentum and the other with $l = 1$ per photon. The relative amplitudes are again given by Eq. 3.15. The interferometer consists of two Dove prisms but no wave plates and is aligned to filter $l = 1$ from $l = 0$. In this case one output has no orbital angular momentum so the average angular momentum current per photon is $M_L = \hbar I_1 / I_0$. The result is shown in Fig. 3.13. Because in this case the current only depends on the output of one port at a single time, the noise in the angular momentum current is small when the photocurrent is small. It was therefore necessary to average over more spectra to obtain the noise results presented in Sec. 3.6 and so the angular resolution is lower.

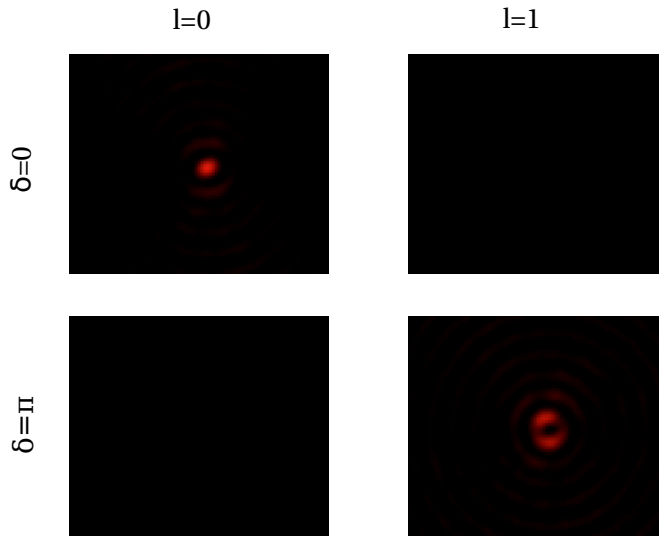


Figure 3.14: Images at one of the outputs of the interferometer for different phase delay showing transmission or reflection of different orbital angular momentum components. δ is the relative phase delay between the arms of the interferometer.

Figure 3.14 shows the image in one of the output ports for incident light with $l = 0$ and $l = 1$, and two settings of the phase delay piezo stage. This shows that the interferometer is filtering the orbital angular momentum components of the input beam. The visibility in this case is 86%. This is lower than that for spin angular momentum. Due to the rotation of the beam by the Dove prisms, any departure from circular symmetry due to slight misalignment etc. will lower the quality of the interference. Note that in Figs. 3.12, 3.13, and 3.15 the theory line accounts for the imperfect visibility and so does not reach the maximum or minimum values.

3.5.2 Generalised angular momentum

We now come to the measurement of the generalised angular momentum theoretically investigated in chapter 2. This time the circular analyser, which transmitted states with different orbital angular momentum but the same spin, is removed. The input beam now varies between the two different states

$$|1/2\rangle = \frac{1}{\sqrt{2}} (|l = 0, s = 1\rangle + |l = 1, s = -1\rangle), \quad (3.34)$$

$$|-1/2\rangle = \frac{1}{\sqrt{2}} (|l = -1, s = 1\rangle + |l = 0, s = -1\rangle). \quad (3.35)$$

Each of these states has a definite value of $L + S/2 = \pm 1/2$. However, neither has a definite value of L or S , with each being a combination of different eigenstates of

these quantities.

The total input beam is given by

$$\vec{E} = A_1 |1/2\rangle + A_2 |-1/2\rangle \quad (3.36)$$

again with

$$A_1 = e^{i(\theta+\pi/4)} \cos \theta, \quad (3.37)$$

$$A_2 = e^{-i(\theta+\pi/4)} \sin \theta. \quad (3.38)$$

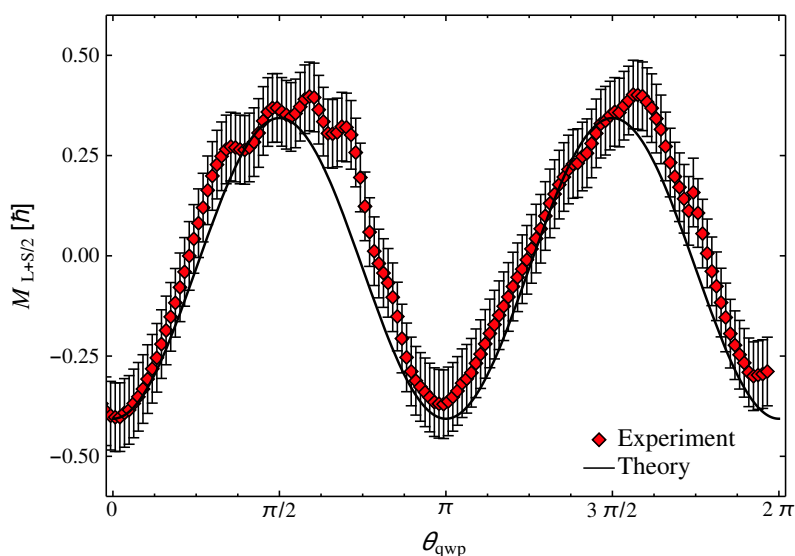


Figure 3.15: Measured generalised angular momentum current as a function of the angle of the quarter-wave plate controlling the input beam. As the quarter-wave plate is rotated the generalised angular momentum in the input beam varies between $\hbar/2$ and $-\hbar/2$. The visibility of the interference pattern is 81%.

The exact path of the fractional angular momentum components through the interferometer is as described in section 3.4.2. Figure 3.15 shows the resulting generalised angular momentum current, showing a close fit to the line predicted by theory, in particular by Eq. 2.137, accounting for imperfect visibility. The oscillations are caused by vibrations in the delay stage. The average angular momentum per photon goes from $\hbar/2$ to $-\hbar/2$ as the input beam is varied between $|1/2\rangle$ and $|-1/2\rangle$. The visibility is 81%, again lowered slightly due to superimposing a rotated beam and polarisation with the original.

Figure 3.16 shows the transmission and reflection of the $j = \pm 1/2$ beam for different phase delays. This shows clearly the ability to filter according to the value of the generalised angular momentum. Comparing to Fig. 3.14, we see that we can

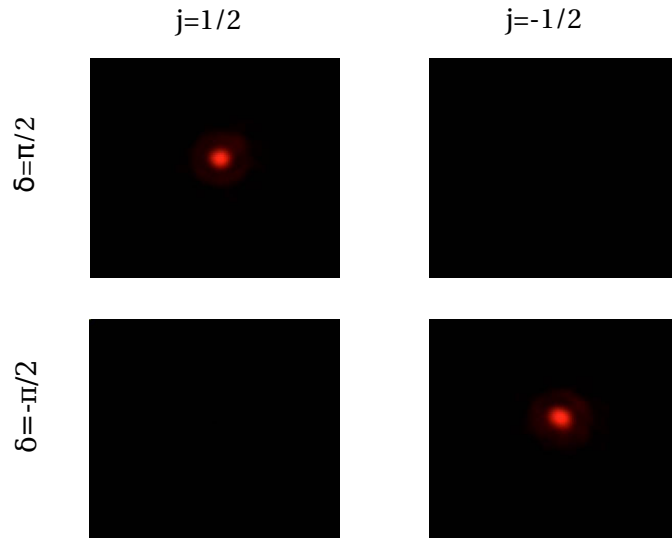


Figure 3.16: Images of output of interferometer for different phase delay showing transmission or reflection of different generalised angular momentum components. The interferometer acts as a filter separating the beam into its constituent generalised angular momentum components.

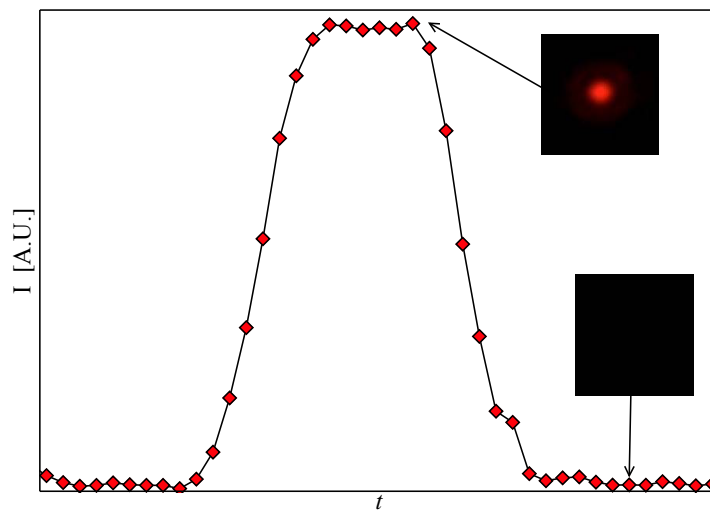


Figure 3.17: Total CCD intensity showing switching between $j = 1/2$ and $j = -1/2$. This image illustrates the two clearly distinguishable states at the output of the interferometer as the input beam is switched between them. Note the CCD intensity is non-linear so the image should be taken qualitatively.

use a modified version of the same interferometer to filter orbital, spin or generalised angular momentum with minimal changes.

Figure 3.17 shows the CCD response when the input beam is switched between $|j = 1/2\rangle$ and $|j = -1/2\rangle$ showing it is easy to distinguish the two states. The response of the CCD is nonlinear, but the image shows qualitatively that the two states can be clearly distinguished. Although this is based on an input beam containing only two components, additional interferometers could filter over a larger subset. This illustrates the possibility of using generalised angular momentum modulation for encoding information and communications, with clearly distinguishable on and off states.

3.6 Quantum results

3.6.1 Spin and orbital angular momentum

We now move on to examining the shot noise in each of the spin, orbital and generalised angular momentum types, again for varying input beams. As before it is not the noise itself, but the Fano factor, that is the noise power divided by the angular momentum current, which gives the amount carried by each individual photon. We first examine the known case of spin and orbital angular momentum. In these cases the quanta of angular momentum carried by each photon are known from a variety of quantum measurements, although to our knowledge noise measurements have not previously been used to determine this.

The case of the spin angular momentum illustrates the general principle of calculating the noise in the angular momentum current. We know from the classical results, section 3.5, that the angular momentum current is related to the electronic current measured by the photodiode in each output by

$$M = \hbar (I_1 - I_2) / e. \quad (3.39)$$

The noise is thus calculated as

$$\sigma_M^2 = (\hbar^2/e^2) [\langle I_1 - I_2 \rangle^2 - \langle (I_1 - I_2)^2 \rangle] \quad (3.40)$$

$$= (\hbar^2/e^2) [\langle I_1 \rangle^2 - \langle I_1^2 \rangle + \langle I_2 \rangle^2 - \langle I_2^2 \rangle] \quad (3.41)$$

$$= (\hbar^2/e^2) [\sigma_1^2 + \sigma_2^2] \quad (3.42)$$

because, as explained in section 3.2.1,

$$\langle I_1 I_2 \rangle = \langle I_1 \rangle \langle I_2 \rangle. \quad (3.43)$$

The Fano factor

$$F = \frac{\sigma_M^2}{|M|} \quad (3.44)$$

is thus related to the photocurrent noise

$$F = \frac{\hbar(\sigma_1^2 + \sigma_2^2)}{e|I_1 - I_2|} \quad (3.45)$$

with the quanta of angular momentum, as in Eq. 2.137, given by

$$j_s \leq T \frac{\sigma_M^2}{|M|} = \frac{\hbar}{2e\Delta f} \frac{\sigma_1^2 + \sigma_2^2}{|I_1 - I_2|}, \quad (3.46)$$

with the lower bound achieved when the beam is in one of the eigenstates of the operator S . Here the effective response time of the system is twice the frequency resolution, with the factor of two due to the two sided power spectrum.

Again since we only measure I_1 for any given input, we must rely on the symmetry between the two ports. The DC photocurrent is assumed to be $I_2 = I_0 - I_1$. However, we will not assume that the total noise is constant, and so instead we take $\sigma_2^2(\theta) = \sigma_1^2(\theta + \pi/2)$. By the rotational symmetry of the input beam and the interferometer elements, rotating the quarter-wave plate by 90° interchanges the role of right and left handedness and so interchanges the port from which each handedness emerges.

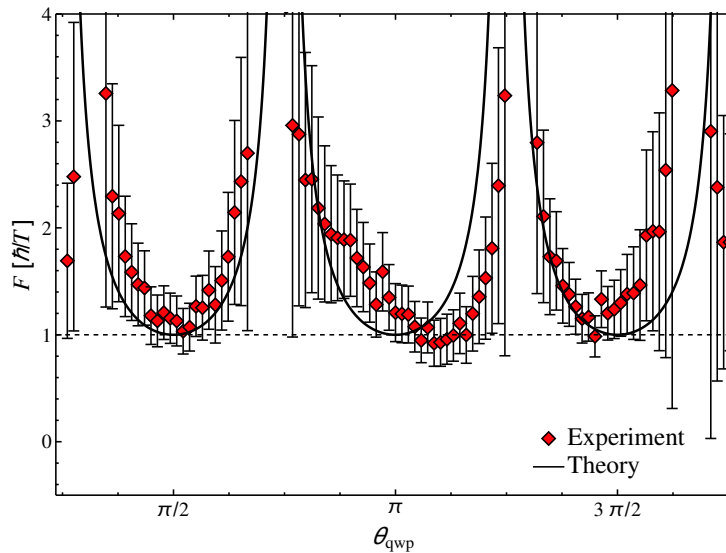


Figure 3.18: Fano factor of spin angular momentum selection showing lower bound of 1, achieved when the beam is in an $s = 1$ or $s = -1$ eigenstate. This shows that the spin angular momentum is carried in discrete units of \hbar .

The result, showing the Fano factor for spin angular momentum as the helicity varies, is plotted in Fig. 3.18. The noise is consistently limited by the absolute bound of $F = 1$, consistent with the claim that each photon carries $\pm 1\hbar$ of angular

momentum. Note that in Figs. 3.18, 3.19, and 3.20, unlike the plots of classical current, the visibility is not included in the theory plot. Instead this reflects the absolute shot noise limit.

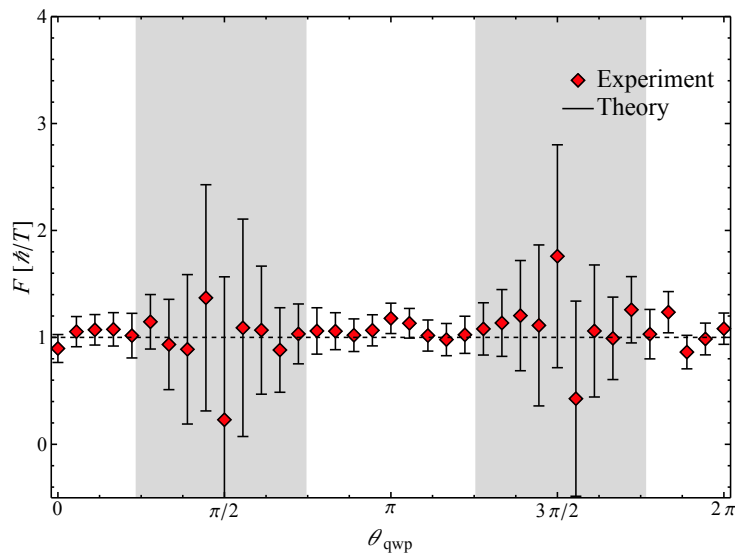


Figure 3.19: Fano factor of orbital angular momentum selection showing lower bound of 1. Greyed areas are those where the majority of the intensity is in the port which is not measured, and hence the error is large.

The experiment was repeated for orbital angular momentum, with an input beam ranging from $l = 0$ to $l = 1$. This time since one of the beams has no angular momentum we have

$$M = \frac{\hbar}{e} I_1 \quad (3.47)$$

and

$$F = \frac{\hbar}{2e\Delta f} \frac{\sigma_I^2}{|I|} \quad (3.48)$$

without needing to calculate the output of the other port. This gives a flat noise Fano factor $F = 1$, unlike the peaks and troughs in the case of spin angular momentum (Fig 3.18). However, now the angular momentum current can approach zero, and so although the Fano factor $F \rightarrow 1$ in this limit, the measured noise is small compared to the background and the error is very large in these cases. Despite this the result is consistent with angular momentum being carried in discrete units of \hbar .

3.6.2 Generalised angular momentum

The main result of this chapter is the measurement of the shot noise of a beam with half-integer general angular momentum. We have already seen the classical result

in the previous section, which confirms that the beam is separated into two outputs depending on the value of $j = \pm 1/2$. Hence the angular momentum current is

$$M = \frac{\hbar}{2e} (I_1 - I_2) \quad (3.49)$$

As with the spin angular momentum case, the output of each port carries angular momentum so we must include both; we do this by replacing the value of the second output with the first output delayed by $\pi/2$. The noise is

$$\sigma_M^2 = \langle M^2 \rangle - \langle M \rangle^2 \quad (3.50)$$

$$= \frac{1}{4} (\sigma_1^2 + \sigma_2^2) \quad (3.51)$$

as once again the two outputs are uncorrelated. The Fano factor is

$$F = \frac{\hbar}{4e\Delta f} \frac{\sigma_1^2 + \sigma_2^2}{I_1 - I_2}. \quad (3.52)$$

The quantum of angular momentum is the lower bound of the Fano factor multiplied by the detection time. Expressed in terms of the measured voltage V_1 and its associated noise

$$j_\gamma \leq TF = \frac{\hbar}{2eG\Delta f_e} \frac{(\sigma_1^2(\theta) + \sigma_1^2(\theta - \pi/2))}{2V_1 - V_0}, \quad (3.53)$$

where G is the transimpedance of the amplifier. Equation 3.53, when expressed in units of \hbar , has a lower bound of $1/2$ rather than 1 , showing the quanta of the generalised angular momentum is $\hbar/2$.

Figure 3.20 shows the measured value compared to the theoretical lower bound. The measured noise is slightly above the lower bound due to the imperfect visibility and to any additional noise. However, at each extrema of the current, when the beam is a pure state of either $j = 1/2$ or $j = -1/2$, the Fano factor dips clearly and consistently below 1 , and close to $1/2$. Indeed, given the visibility is 81% the minimum Fano factor expected is actually 0.62 , which is consistently achieved.

3.7 Error analysis

Considering the plots of the DC signal, Figs 3.12, 3.13 and 3.15, we can see some variance from the expected behaviour. However, the DC signal itself is measured to a high accuracy, typically $< 0.25\%$. The measured signal deviates from the theory due to vibrations of the interferometer, particularly in the piezo stage which controls the relative phase delay. The total power $I_0 = I_1 + I_2$ is a constant, but because the angular momentum current is calculated from the photocurrent at one output port at two different times, changes in the position of the piezo stage can lead to both I_1 and I_2 being higher or lower than would be expected. This instability can therefore

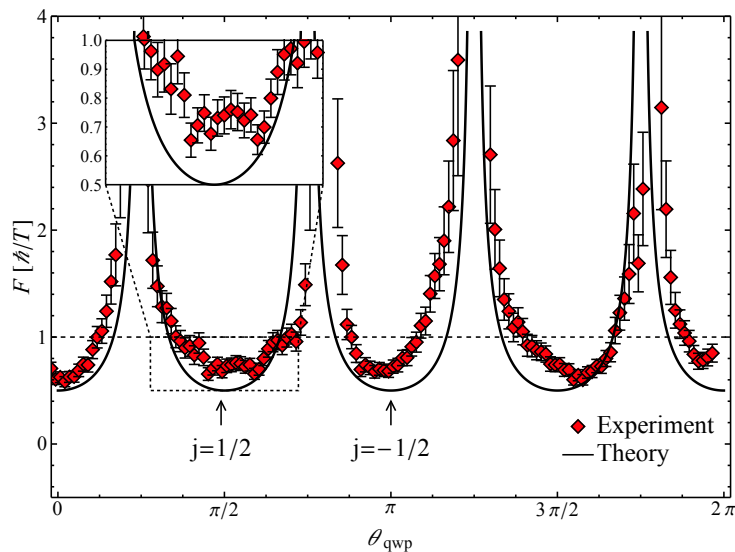


Figure 3.20: Measured Fano factor of generalised angular momentum for a varying input beam. The lower bound of the Fano factor is $1/2$, showing that this is the quantum, in units of \hbar , of this observable. The dashed line at $F = 1$ shows that the data clearly dip below this line, which would be the limit if the quantum was \hbar , whenever the beam is in an eigenstate of $J_{1/2}$.

be included as an error in the photocurrent corresponding to the total power. This is done by taking the total intensity at each angle of the quarter-wave plate to be the sum of the measured intensity for that angle and that at an angle $\pi/2$ greater. The standard deviation of these values is taken as the error in the total intensity and used in the calculation of dependent variables as usual.

The second significant source of error in the shot noise calculations presented here is variance in the noise. Taking a single time series and calculating the Fourier transform gives the frequency components that are present during that short time. Over longer time scales other frequency components may be present in greater or lesser amounts. As the total sample time gets longer, the frequency resolution will increase (for fixed sampling rate) which will allow periodic signals to be further and further isolated. However, white noise has no time correlation, and so there is no time scale over which we can accurately measure the precise power in a particular frequency bin.

The error in the measured shot noise at a particular point is of the order of the noise itself [121]. It is therefore necessary to average this value. One possibility is to sample for a time which gives a higher frequency resolution than required and average nearby frequency bins. The solution we opt for is to break up the sample into many shorter time series and take the FFT of each one individually, to give

many spectra each with the required resolution. The resulting spectra are then averaged at each frequency point. This is known as Bartlett's method, and it can be proved that this approaches the true power spectral density as the number of samples grows [122]. The fractional error of the noise is thus approximately the inverse of the square root of the number of periodograms.

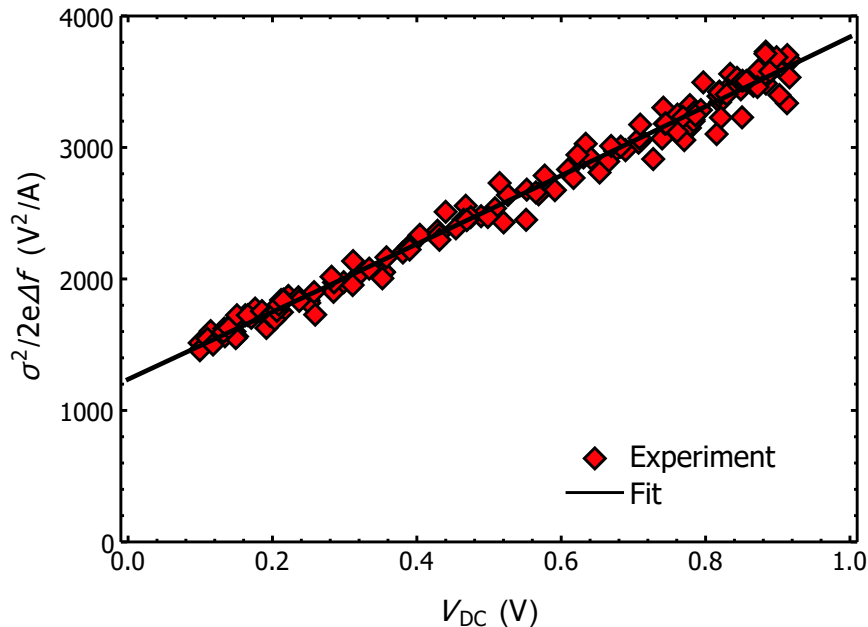


Figure 3.21: Shot noise, normalised by $2e\Delta f_e$, in the measured voltage as a function of the DC voltage, fit to a quadratic with linear coefficient given by the transimpedance G . The straight line fit confirms that we are measuring in the quantum noise limit regime and that the transimpedance is as predicted. The data has a quadratic dependence due to classical noise which is small on this scale and is included in the error, given by the standard deviation of the residuals of this fit.

We can write the measured noise

$$\sigma_m^2 = \sigma_0^2 + \alpha V + \beta V^2 + r \quad (3.54)$$

as the sum of a background noise σ_0 , a shot noise which depends linearly on the signal, a classical noise term that depends quadratically on the signal and a random error r due to the fluctuations in the noise as it is measured. The linear term should have a coefficient

$$\alpha = 2e\Delta f_e G \quad (3.55)$$

where G is the transimpedance of the amplifier and Δf_e is the effective frequency resolution, i.e. the actual frequency resolution multiplied by the normalised equivalent noise bandwidth of the window function. The measured noise power is shown as a function of the DC voltage in Fig. 3.21, fitted to a quadratic with fixed linear coefficient $2e\Delta f_e G$. Firstly the close fit confirms the transimpedance is 2550Ω as

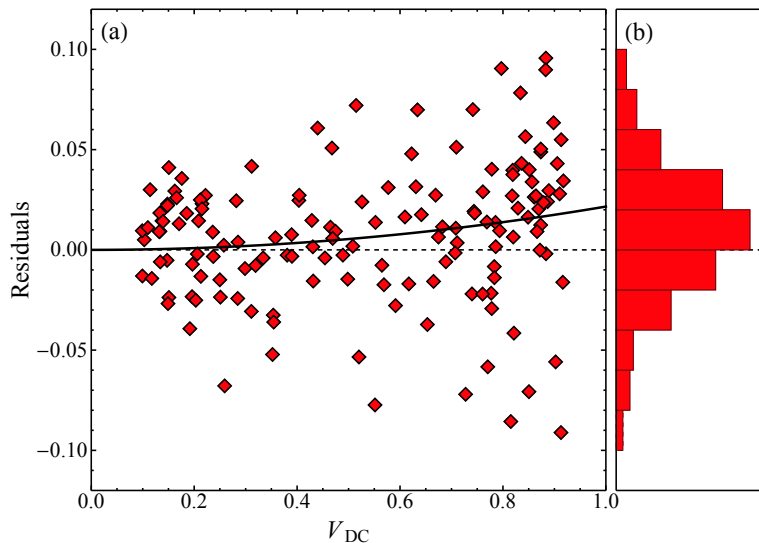


Figure 3.22: Residuals of measured noise from linear fit (given as fraction of measured noise). The error consists of a random error plus a small quadratic classical noise leading to a distribution skewed slightly towards positive values. The standard deviation is taken as the relative error.

expected. More importantly the good linear fit confirms that we are indeed measuring in the quantum shot noise regime. The scaling with power is a standard way to confirm if noise is quantum or classical, as shot noise scales linearly with power and classical noise scales quadratically [123].

Although we could fit the measured noise to a free quadratic function, the difference in scale between the linear and quadratic term lead to a large uncertainty in the coefficients using this method. Instead, taking the linear coefficient as fixed we find that the residuals are randomly distributed around a quadratic trend, due to the classical noise, which is small compared to the error in the noise. The standard distribution of the residuals is approximately $90 V^2/A$. Comparing to the scale on Fig. 3.21, we see that this is close to the predicted error of 3% for an average over a thousand samples.

3.8 Conclusions

In this chapter we have described an experiment which can filter a beam of light according to its angular momentum. This angular momentum may be either the spin, orbital, or the generalised angular momentum described theoretically in the previous chapter. We have shown that it is possible to generate beams with half-integer

generalised angular momentum, and to filter them according to this fractional value. This interferometer, with a detector in both outputs, can act as a generalised angular momentum detector, or as a filter to separate the components for further processing.

In this experiment we have not only measured the average angular momentum current of a beam of light, but also its quantum fluctuations. By computing the Fano factor, the quantum noise normalised by the current, we measured the quantum of angular momentum carried by each photon in a beam which is an eigenstate of $L + S/2$ with eigenvalue $\pm 1/2$. The reduced shot noise bound in the angular momentum current of these beams shows clearly that the quantum is $\hbar/2$, and hence that the classical current is not simply the result of averaging over many photons in the beam. This scheme can be similarly extended to measure other generalised angular momentum currents by varying the ratio between the angle of rotation of the image, specified by the angle between the Dove prisms, and the angle of rotation of the polarisation, specified by the angle between the half-wave plates. Furthermore a larger subspace could be explored by the cascading of multiple interferometer stages.

Chapter 4

Biaxial hyperbolic metamaterials

4.1 Introduction

In this chapter we move on from the concept of generalised angular momentum. We turn instead to the study of conical refraction in a new setting, which leads to a theory which is topologically distinct from that of a conventional biaxial crystal. This setting is an anisotropic hyperbolic metamaterial, which has an isofrequency surface which is an open hyperboloid, in contrast to the closed ellipsoid of conventional optical materials.

Metamaterials are composite materials which use sub-wavelength building blocks to create bulk properties which can vary significantly from those which commonly occur in nature [124], including negative permittivity or permeability [125]. Of these one of the most important classes is that of hyperbolic metamaterials (HMMs) [9] which have recently been the subject of intense interest [126]. Using metal and dielectric elements, these materials have a negative principal dielectric constant in at least one direction [8]. Although naturally occurring crystals can be found with this property [127], this is more commonly achieved with artificial nano-structured designs. Common structures include planar layers of metal and dielectric, or metal rods in a dielectric background (see Fig. 4.1). The differing boundary conditions for electric fields which lie along or across the metal-dielectric interfaces leads to a differing sign for the dielectric constant in these directions [128]. Hyperbolic metamaterials are particularly suitable for applications due to their simple design, ease of fabrication at deeply sub-wavelength scales and non-resonant response across a range of wavelengths [129].

The many unique properties of hyperbolic metamaterials stem from the iso-

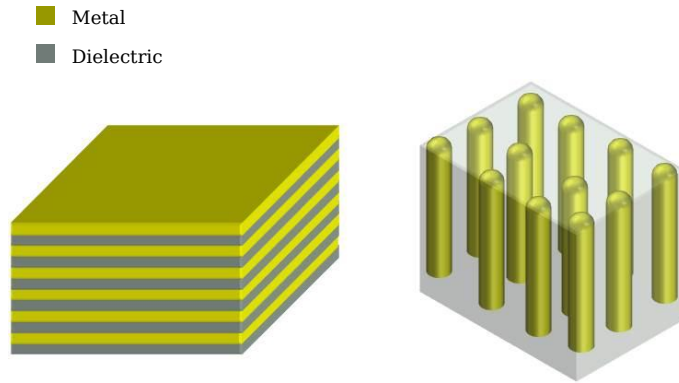


Figure 4.1: Example of common hyperbolic metamaterial configurations. Common arrangements include alternating layers of metal and dielectric and rods of metal embedded in a dielectric background. These can be made anisotropic in the plane by using a uniaxial dielectric material or having a non-square unit cell respectively.

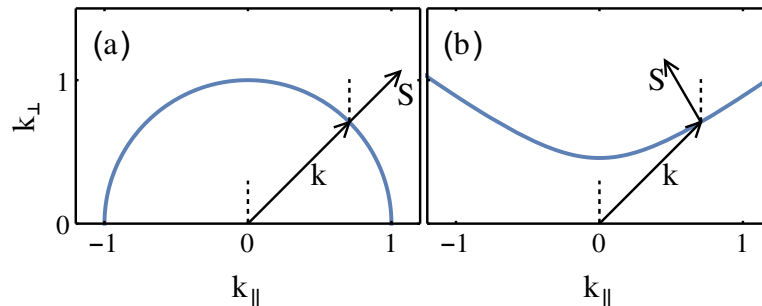


Figure 4.2: Illustration of negative refraction in a hyperbolic metamaterial. The Poynting vector \vec{S} , which gives the direction of ray propagation, is orthogonal to the iso-frequency surface, which gives the direction of the wave-vector \vec{k} . In a positive index material (a), the Poynting vector will lie on the same side of a normal to the interface as the wave-vector. In a HMM (b) the Poynting vector and the wave-vector lie on opposite sides of the normal.

frequency surface of the medium, i.e. the surface in k -space at which waves can propagate at a specific frequency. This surface, which is closed and finite when all three principal indices are positive, becomes hyperbolic when at least one index is negative. This means that for some angle of \hat{k} there is a divergence in $|\vec{k}|$, leading to a formally infinite density of states and modes with extremely short wavelength in the material. Furthermore the curvature of the hyperbola, being opposite to the normal curvature of an ellipse, leads to negative refraction, whereby a ray approaching the interface with a hyperbolic metamaterial is refracted back on to the same side of the normal [130]. This is illustrated in Figure 4.2. The iso-frequency surface gives the allowed values of \vec{k} for a given frequency. When light is incident on an interface the parallel momentum k_{\parallel} is conserved. However,

the Poynting vector is always normal to the iso-frequency surface, so when the iso-frequency surface curves away from the plane of incidence the Poynting vector will lie on the opposite side of the normal to the wave-vector of the incoming light. (Note however, that negative refraction also refers to negative phase velocity which is not present in this case.) Because these properties result from the general shape of the iso-frequency surface they will exist across a range of frequencies and do not depend on precise tuning.

Such unique properties lead naturally to many applications. The formally infinite density of states will cause a broadband Purcell effect which increases the efficiency of many quantum nano-photonics devices, such as single photon sources and broadband quantum emitters with high yield [131, 132, 133]. Negative refraction has been proposed to lead to super resolution, imaging nanoscale objects at resolutions higher than the diffraction limit [134, 132]. Conversely the existence of extremely high $|\vec{k}|$ modes allows light to be focused to extremely small spots, with applications from scanning microscopy to heat assisted magnetic recording [135].

4.2 Biaxial hyperbolic metamaterials

The most common HMMs considered are uniaxial materials for which $\epsilon_1 < 0 < \epsilon_2 = \epsilon_3$ where ϵ_i are the principal dielectric constants, i.e. the elements of the dielectric permittivity tensor in a frame in which it is diagonal. The general case, however, is a biaxial HMM, where $\epsilon_1 < 0 < \epsilon_2 < \epsilon_3$. Such a material could be realised as layers of metal and dielectric, where the dielectric material has uniaxial isotropy in the plane, or as rods of metal embedded in a dielectric with different rod spacings in the x and y directions [136]. The iso-frequency surface for the extraordinary ray is then an asymmetric hyperboloid [137].

In this chapter we describe the full two-sheeted dispersion surface (constant-frequency surface) of a generic HMM with no equal dielectric constants. In section 4.3 we describe this surface for the full range of materials described by positive or negative real dielectric constants. The iso-frequency surface describes the propagation of both the ordinary and the extraordinary rays with orthogonal polarisations. As with biaxial positive-index materials [138] we find conical singularities where the two sheets intersect. However, these points now resemble the intersection of a hyperbola and an ellipsoid, rather than two ellipsoids.

In section 4.4 we use geometrical optics to obtain a description of rays with wave-vector close to the degeneracy. We derive the polarisation and the Poynting vector, or energy flow of these rays as a function of the direction of the wave-vector. This predicts refraction of an incoming beam into two intersecting rather than concentric cones, an effect topologically distinct from that in a conventional biaxial crystal and

completely lacking from a uniaxial HMM.

In section 4.5 we extend the theory to include small absorption in the material and show explicitly that the conical intersections remain. We also develop a wave optics description of propagation near the optic axis allowing us to calculate the full diffraction pattern formed for an incident beam, for example a Gaussian beam. These patterns are qualitatively different from those obtained in positive index materials, in particular lacking circular symmetry.

An important feature of our results is the identification of conical singularities in HMMs. Similar linear intersections, which have been reported previously in systems with sub-wavelength patterning such as photonic crystals [139, 140] and frequency dependent metamaterials [26, 141, 137]. In these cases, a degeneracy occurs at a particular frequency, due to fine-tuning the frequency to match the sub-lattice periodicity, or to match a zero of the frequency dependent dielectric constant. At other nearby frequencies there is generally no singularity, and the constant frequency contours in k -space do not feature any intersections. In contrast biaxial materials have intersections in the iso-frequency contours mapped in k -space, which are directly comparable to the Fermi surface of a solid. These depend on the general symmetry of orthogonal polarisations throughout the crystal and do not rely on fine-tuning of any parameter. In particular we show that in the effective medium theory these degeneracies exist over a continuous range of frequencies and are protected by a topological argument. In the whole $\omega - \vec{k}$ space they would appear as line rather than point degeneracies.

Because the HMM is built from deeply sub-wavelength structures, it is possible to describe propagation of light in such a metamaterial using effective medium theory, which describes the effect of the sub-structure in terms of an average dielectric tensor. This average is taken in a way which accounts for the anisotropy of the structure. It is important to realise however, that this method has strong limitations [128, 142]. Clearly it will only be valid when the scale of the structure is much less than the wavelength, but crucially the valid comparison is to the wavelength in the medium. Since the high- $|k|$ states will have a very short wavelength in the material, at some point the approximation will break down and the iso-frequency surface of the actual composite material will not go to infinity. Furthermore due to the extreme anisotropy the wavelength, and hence the validity of the approximation, can vary with direction and polarisation. Finally the approximation describes the bulk properties and coupling of light to real samples can depend on the edge, e.g. for layered materials it can depend on which material the structure terminates on. In the majority of this work we consider only an effective medium theory, assuming that a material can be constructed with the required properties. However, in section 4.6 we will discuss how such a system would be implemented and what

conditions would be necessary for a valid effective medium theory to hold.

4.3 Fresnel equation and dispersion surfaces

4.3.1 Dispersion surfaces

We can describe a nano-structured metamaterial in the effective medium theory by a three-dimensional dielectric tensor ϵ_{ij} or by the principal dielectric constants, ϵ_i , which are its components in the frame in which it is diagonal [61]. Effective medium theory describes the sub-wavelength patterning of different materials by an average, anisotropic dielectric tensor according to the Maxwell-Garnett formulas [142]. Plane wave solutions to Maxwell's equations in the medium lead to the Fresnel equation for the refractive index,

$$\sum_i \frac{\epsilon_i \eta_i^2}{n^2 - \epsilon_i} = 0, \quad (4.1)$$

where $\vec{\eta}$ is a unit vector in the direction of the wave-vector \vec{k} . The two solutions for n^2 for a given direction $\vec{\eta}$ form a two-sheeted dispersion surface [61]. At a fixed frequency, these surfaces give the phase velocity, or equivalently the wave-vector magnitude, in the medium, for a given wave-vector direction. The ray or energy flow direction will be orthogonal to the dispersion surface at the point defined by that wave-vector [143]. In the following we assume without loss of generality that $\epsilon_1 < \epsilon_2 < \epsilon_3$.

This chapter contains multiple plots of solutions of Eq. 4.1 so we give here a brief explanation of their meaning. To follow this explanation, the reader may consider Fig. 4.4 or Fig. 4.3. They are most easily thought of as surfaces in \vec{k} -space, of the allowed \vec{k} vectors at a fixed frequency. For example in free space, $k = \omega/c = k_0$, and the surface is a sphere. This means that in all directions light propagates with a wave-vector of magnitude k_0 . In an isotropic medium, this is simply modified by changing the length of this wave-vector, $k = nk_0$ for some scalar refractive index n . The resulting surface is a larger sphere with radius nk_0 . A non-isotropic medium will have different refractive index in different directions, and the surface will be an ellipse. A birefringent medium will have a different refractive index for each polarisation, and so there will be two surfaces, rather than one. In this way more complex surfaces represent more complex materials. Important properties are the distance of the surface from the origin in a particular direction, representing the refractive index, whether a surface is symmetric around some axis, representing isotropy under rotations, and whether a line from the origin in a particular direction intersects a surface once or twice, representing whether or not the material is birefringent in that direction.

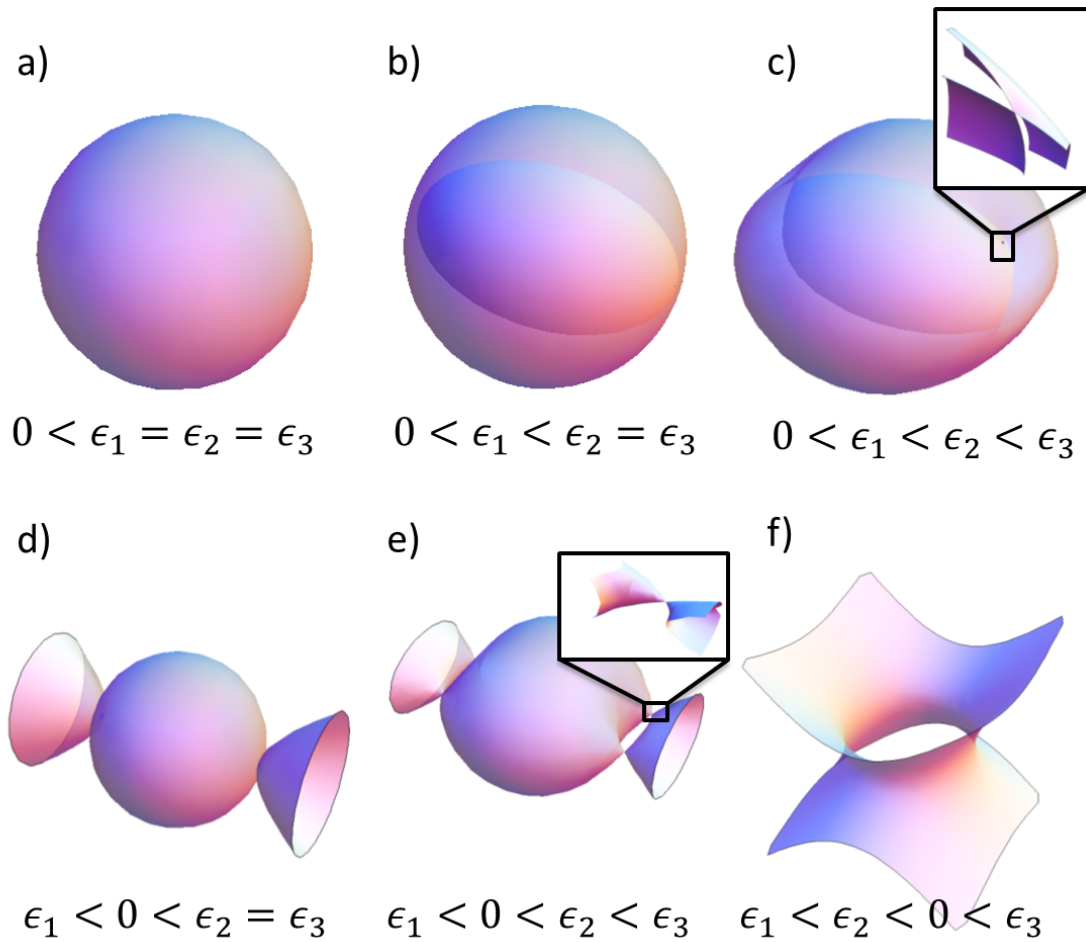


Figure 4.3: Iso-frequency surfaces for various effective index materials: (a) isotropic (b) uniaxial (c) biaxial (d) uniaxial-hyperbolic (e) biaxial-hyperbolic type-1 (f) biaxial-hyperbolic type-2. Shading is for perspective only. Additional cases not shown include $\epsilon_1 = \epsilon_2 < 0 < \epsilon_3$, which is identical to (f) but with circular cross-sections, and $\epsilon_3 < 0$, in which case there are no real solutions. These surfaces are polar plots of refractive index as a function of ray direction \vec{n} . In the case of (b) and (d) the surfaces intersect at two points, at which they are parallel. In the case of (c) and (e) the surfaces have four conical intersections. Insets in (c) and (e) show cutaway close-ups of the intersection points.

Figure 4.3 shows sections of the dispersion surfaces for a variety of materials. These surfaces are polar plots where the radial distance represents the refractive index experienced by a ray propagating in that direction in \vec{k} -space. Equivalently, they are three-dimensional cuts of the four-dimensional $\omega(\vec{k})$ dispersion surface, taken at a constant ω . In the approximation where the dielectric constants depend weakly on frequency, these surfaces will simply contract or expand as ω is decreased or increased respectively, meaning the critical points will trace out lines. Outside of this approximation the dispersion surface will change shape but the basic features will remain until the dielectric constants cross each other or zero. Hence assuming a smooth dependence on frequency there will always be a continuous range of frequencies for which these singularities exist.

The classical cases, $0 < \epsilon_i$, are shown in the first row, and are the subject of conventional crystal optics. The surfaces have positive curvature and finite area. The hyperbolic cases, $\epsilon_1 < 0$ shown in the second row, are the result of nano-structured materials which have properties rarely found in nature at optical frequencies [9]. They have dispersion surfaces which are unbounded in $|k|$ at any frequency, and feature both positive and negative curvature [129].

The possible classical materials fall into three categories. Figure 4.3(a) shows an isotropic material which has a single, spherical dispersion surface. Once isotropy is broken, the surface splits into two as the two orthogonal polarisations experience different dielectric constants. For a uniaxial material, with two indices equal, these surfaces intersect at two points, along a single optic axis as shown in Fig. 4.3(b). However, the surfaces are parallel at the degenerate points, and so the normals remain well defined [144]. For a biaxial crystal, shown in Fig. 4.3(c), rotational symmetry is broken completely. The surfaces intersect at four points along two optic axes. The gradient of the surfaces is singular at the degenerate points and the normal is not well defined.

These singularities lead to the unique phenomenon of conical refraction [138]. For a general angle of incidence in an anisotropic medium, the two orthogonal polarisations of an incident ray are refracted into two rays with different wave-vectors, called the ordinary and extraordinary rays. In conical refraction, when the incident wave-vector coincides with the optic axis, the two orthogonally polarised incident rays are refracted into two concentric cones which contain all polarisations at different points around each cone [145, 61]. For a general review of polarisation singularities and vortices, see [146].

When one of the dielectric constants becomes negative, leading to a hyperbolic metamaterial, there is a topological transition of one of the surfaces, from an ellipsoid to a hyperboloid. Figure 4.3(d) shows a uniaxial HMM. The surfaces again intersect at two points where they are parallel.

In the case of a biaxial HMM, shown in Fig. 4.3(e), linear degeneracies occur. The hyperboloid and the ellipsoid intersect at four degenerate points. The propagation of light near these singularities is the main topic of this chapter. In the final case where two of the three indices are negative, Fig. 4.3(f), there is again a single dispersion surface which is a type-2 hyperboloid [129] with no singularities. This single dispersion surface describes one polarisation which can propagate in the material. For the orthogonal polarisation the material is metallic, and absorbing, hence there is no second real solution to the Fresnel equation.

In both Fig 4.3(b) and (d) the two sheets have a quadratic degeneracy. Including a perturbation $\epsilon_2 \neq \epsilon_3$ will either open a gap or cause the quadratic intersection to split into two linear intersections, in line with general band theory. If a gap were to open however, it would leave at least one closed surface which described the propagation of a different linear polarisation at each point. The field of polarisation directions described by this surface would form a tangential vector field on a closed two-dimensional surface, which is forbidden by the hairy ball theorem, unless the linear polarisation vanishes at least once. Comparing with the Poincaré sphere representation it can be seen that the tangential polarisation would vanish at a point of circular polarisation. However, in the presence of chiral symmetry it is not possible for the two circular polarisations to have different refractive indices, hence it is impossible for a gap to open. Introducing chirality however, will indeed open such a gap [55], although polarisation singularities will generally remain.

As noted at the beginning of the chapter, these surfaces describe the propagation of light in an effective medium, which matches the actual medium as long as the wavelength of light in the medium is large compared to any structure of the material. Hence the actual material will be described by these dispersion states for small $|k|$. For the cases where the Fresnel surface go to infinity, they should be truncated at some appropriate value of refractive index n for which $nk_0 > k_{\text{kmax}}$, where k_0 is the vacuum wave-vector and k_{kmax} is the largest wave-vector which we wish to consider in the effective medium theory. In these directions, it would be necessary to solve Maxwell's equations in the metal-dielectric unit cell to find exact solutions.

4.3.2 Intersection points

The transition from a conventional biaxial material to a biaxial type-1 HMM is shown in Fig. 4.4 as ϵ_1 goes from positive to negative. As rotational symmetry in the y_ϵ - z_ϵ plane is broken (note we use the subscript ϵ to denote the basis in which ϵ is diagonal), the degenerate points are free to move around the x_ϵ axis as ϵ_1 varies. The points start in the x_ϵ - z_ϵ plane and move closer to the x_ϵ axis as $\epsilon_1 \rightarrow 0$. Then as the topological transition occurs the critical points change direction and move away from the x_ϵ axis into the x_ϵ - y_ϵ plane.

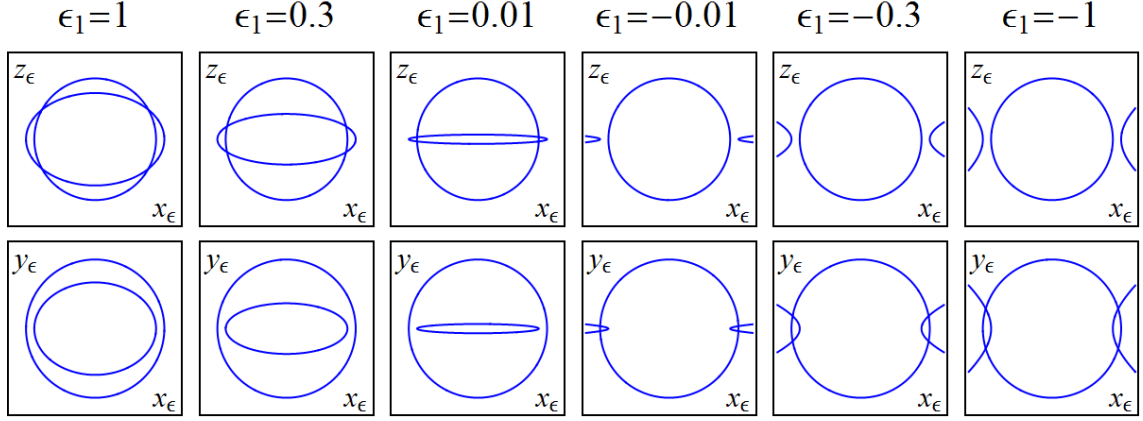


Figure 4.4: The transition from biaxial to biaxial-hyperbolic type-1 material as ϵ_1 passes through 0. One of the dispersion surfaces changes topology from an ellipsoid to a hyperboloid. The intersection points move from the x_ϵ - z_ϵ plane to the x_ϵ - y_ϵ plane. The first row shows the surfaces in the x_ϵ - z_ϵ plane ($y_\epsilon=0$). The second row shows the surfaces in the x_ϵ - y_ϵ plane ($z_\epsilon=0$). Note the subscript ϵ denotes the basis in which ϵ is diagonal.

The topological transition of the iso-frequency surface intersections is shown by calculating the solutions to the Fresnel equation (4.1) which are degenerate. We find two sets of solutions

$$\begin{aligned}\eta_1 &= \pm \sqrt{\frac{\epsilon_3 (\epsilon_2 - \epsilon_1)}{\epsilon_2 (\epsilon_3 - \epsilon_1)}} \\ \eta_2 &= 0 \\ \eta_3 &= \pm \sqrt{\frac{\epsilon_1 (\epsilon_3 - \epsilon_2)}{\epsilon_2 (\epsilon_3 - \epsilon_1)}}\end{aligned}\tag{4.2}$$

and

$$\begin{aligned}\eta_1 &= \pm \sqrt{\frac{\epsilon_2 (\epsilon_3 - \epsilon_1)}{\epsilon_3 (\epsilon_2 - \epsilon_1)}} \\ \eta_2 &= \pm \sqrt{\frac{-\epsilon_1 (\epsilon_3 - \epsilon_2)}{\epsilon_3 (\epsilon_2 - \epsilon_1)}} \\ \eta_3 &= 0.\end{aligned}\tag{4.3}$$

The first solution (4.2) is real, and therefore physical, when all ϵ_i are positive. As ϵ_1 becomes negative η_3 in (4.2) becomes imaginary. The second solution (4.3) then becomes the real, physically relevant, $\vec{\eta}$. In this way the transition through $\epsilon_1 = 0$ separates topologically distinct sets of degenerate solutions.

Figure 4.5 shows the cross-sections of the dispersion surfaces at the degenerate points, in the case of a conventional biaxial crystal and a biaxial hyperbolic material. For a conventional material, both surfaces have similar curvature. The normals to the surfaces close to the optic axis, i.e., the axis which passes through one of the degenerate points, are shown. These normals indicate the direction of refraction for

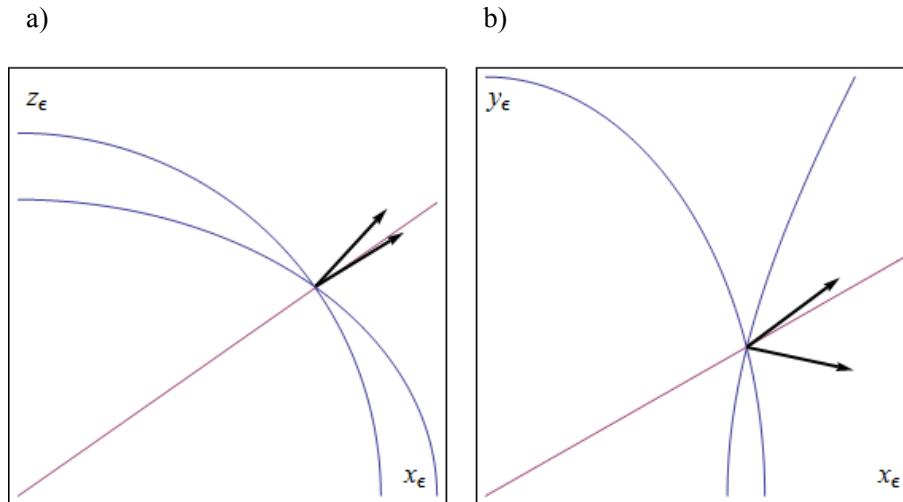


Figure 4.5: The degenerate points in the relevant planes for (a) a conventional biaxial material and (b) a hyperbolic biaxial material. The optic axis is shown by the straight line and the approximate normals to the surfaces for a \mathbf{k} -vector passing close to this axis are shown by the arrows, and are suggestive of the expected conical refraction.

rays which approximately coincide with the optic axis. In the positive ϵ case, one points close to the optic axis while the other points away from the x_ϵ axis. In the case of a biaxial HMM the surfaces have opposite curvature. This leads to one of the normals pointing towards the x_ϵ axis. When the full two dimensional surface is considered, the normals shown here contribute to a cone which is skewed away from the optic axis, in a different direction in each case. In figure 4.5(b), one of the normals points downwards, below the horizontal. If the material is cut so the interface is the y_ϵ - z_ϵ plane then this results in part of the cone being refracted on the opposite side of the normal to the incoming ray, a phenomenon sometimes known as negative refraction. However, this term is also used to refer to negative phase velocity, which is not present in this case.

4.4 Geometric optics of conical diffraction in a hyperbolic metamaterial

4.4.1 Refractive index and polarisation

We now turn to describing the refraction of light in the geometrical optics picture when the initial wave-vector lies close to the optic axis as shown in Fig. 4.5. To achieve this we calculate the refractive index surface experienced by the ray and the resulting Poynting vector of the refracted ray. We describe the ray by polar coordinates in a frame where the x axis coincides with the optic axis, and the z axis

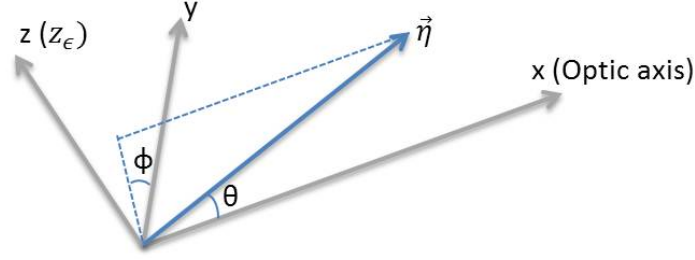


Figure 4.6: The coordinate system used to describe rays close to the optic axis. The x axis corresponds to the optic axis through the points (4.3) while the z axis corresponds to the z_ϵ axis. θ is the angular displacement of the ray from the optic axis while ϕ is the azimuthal angle of the ray in the transverse plane.

coincides with the z_ϵ axis, illustrated in Fig. 4.6. θ is the angle between the ray and the optic axis, while ϕ is the azimuthal angle from the y axis in the y - z (transverse) plane. Expressing $\vec{\eta}$ in terms of θ and ϕ and solving (4.1) we find the refractive index to first order in θ is

$$n^2 = \epsilon_3 - \theta\epsilon_\delta (\cos \phi \pm 1) \quad (4.4)$$

where

$$\epsilon_\delta = \epsilon_3 \sqrt{\frac{(\epsilon_3 - \epsilon_1)(\epsilon_2 - \epsilon_3)}{\epsilon_1 \epsilon_2}} \quad (4.5)$$

is a measure of the anisotropy of the medium. The surface described by (4.4) consists of two cones touching at their points, which is the linear approximation to the surface portrayed in Fig. 4.3(e) around one of the intersection points. Furthermore, we find the polarisation of the two refracted rays is

$$\frac{D_z}{D_y} = \frac{\sin \phi}{\cos \phi \pm 1} \quad (4.6)$$

where \vec{D} is the electric displacement field.

The results (4.4) and (4.6) describe the refractive index experienced by an incoming ray. A ray which comes from an azimuthal angle ϕ can be decomposed into the two orthogonal polarisations given by (4.6). These two polarisations experience the refractive indices (4.4). The polarisations are independent of θ , as long as θ is small. Thus for any ray not exactly coincident with the optic axis, there are two distinct polarisation modes. As ϕ varies, the direction of polarisation described by a given dispersion surface rotates, so that a ray with one linear polarisation and azimuthal angle ϕ undergoes the same refraction as a ray with the orthogonal polarisation and azimuthal angle $\phi + 180^\circ$. However, (4.6) is undefined when $\theta = 0$. Hence there is also a polarisation degeneracy at the conical singularity where all polarisations experience the same refractive index.

Equation (4.4) differs from the usual case of conical refraction in a biaxial crystal in two noteworthy ways. Firstly ϵ_3 plays the role of the average dielectric constant,

despite being the largest of the three indices, while for a conventional biaxial crystal the median index ϵ_2 plays this role. Secondly, the parameter ϵ_δ depends on $\sqrt{\epsilon_3 - \epsilon_1}$, which is a large parameter since ϵ_1 is negative. In the conventional, $\epsilon_i > 0$, case of conical refraction the corresponding form is $\epsilon_\delta = \epsilon_2 \sqrt{(\epsilon_2 - \epsilon_1)(\epsilon_3 - \epsilon_2) / \epsilon_1 \epsilon_3}$, which is usually small. The polarisation modes (4.6) are identical to the positive ϵ case.

4.4.2 Poynting vector

We now calculate the Poynting vector using equations (4.4) and (4.6) for the two orthogonal polarisations associated with each incident wave-vector. The Poynting vector is, up to an overall constant, given by

$$\vec{P} = \vec{E}^* \times \vec{H}. \quad (4.7)$$

\vec{E} and \vec{H} can be expressed in terms of D_z and D_y , given by (4.6), using Maxwell's equations and the constitutive relations. The result,

$$\begin{aligned} P_x &= \frac{1}{\epsilon_3^{3/2}} + \theta \frac{\epsilon_\delta}{\epsilon_3^{5/2}} (\cos \phi \pm 1) \\ P_y &= \frac{\epsilon_\delta}{2\epsilon_3^{5/2}} (1 \pm \cos \phi) + \frac{1}{\sqrt{\epsilon_3}} \theta \left[\pm \frac{\epsilon_\delta^2}{4\epsilon_3^3} (\cos \phi \pm 1)^2 \right. \\ &\quad \left. + \frac{1}{2} \left(\frac{1}{\epsilon_1} + \frac{1}{\epsilon_2} \right) (\cos \phi \pm 1) \mp \frac{1}{\epsilon_3} \right] \\ P_z &= \pm \frac{\epsilon_\delta}{2\epsilon_3^{5/2}} \sin \phi + \frac{1}{\sqrt{\epsilon_3}} \theta \left[\frac{\epsilon_\delta^2}{4\epsilon_3^3} (\cos \phi \pm 1) \sin \phi \right. \\ &\quad \left. + \frac{1}{2} \left(\frac{1}{\epsilon_1} + \frac{1}{\epsilon_2} \right) \sin \phi \right], \end{aligned} \quad (4.8)$$

is compared with the $\epsilon_i > 0$ case in Fig. 4.7 for three values of θ .

Equations (4.6) and (4.8) together describe the refraction of an incoming ray with wave-vector at a small angle θ to the optic axis, and an azimuthal angle ϕ in the perpendicular plane. As ϕ is varied, the resulting rays sweep out two intersecting cones while the polarisation component which is refracted into each cone also varies. For $\theta = 0$ a single ray of any polarisation is refracted into a complete cone, containing all polarisations. However, any realistic incoming beam will be a superposition of rays with the $\theta = 0$ ray contributing an infinitesimal amount to the resulting pattern [145].

Figure 4.7 shows the loci of the Poynting vectors at different fixed angles θ as the azimuthal angle ϕ is varied, for a biaxial conventional material and a biaxial HMM. This is indicative of the paths taken by refracted rays in the material. The figures show that the usual result of two concentric cones [145] changes to the topologically distinct case of two intersecting cones. At $\theta \approx 0$ the cones are degenerate, and skewed away from the optic axis. The degeneracy is clear from equation (4.8). For

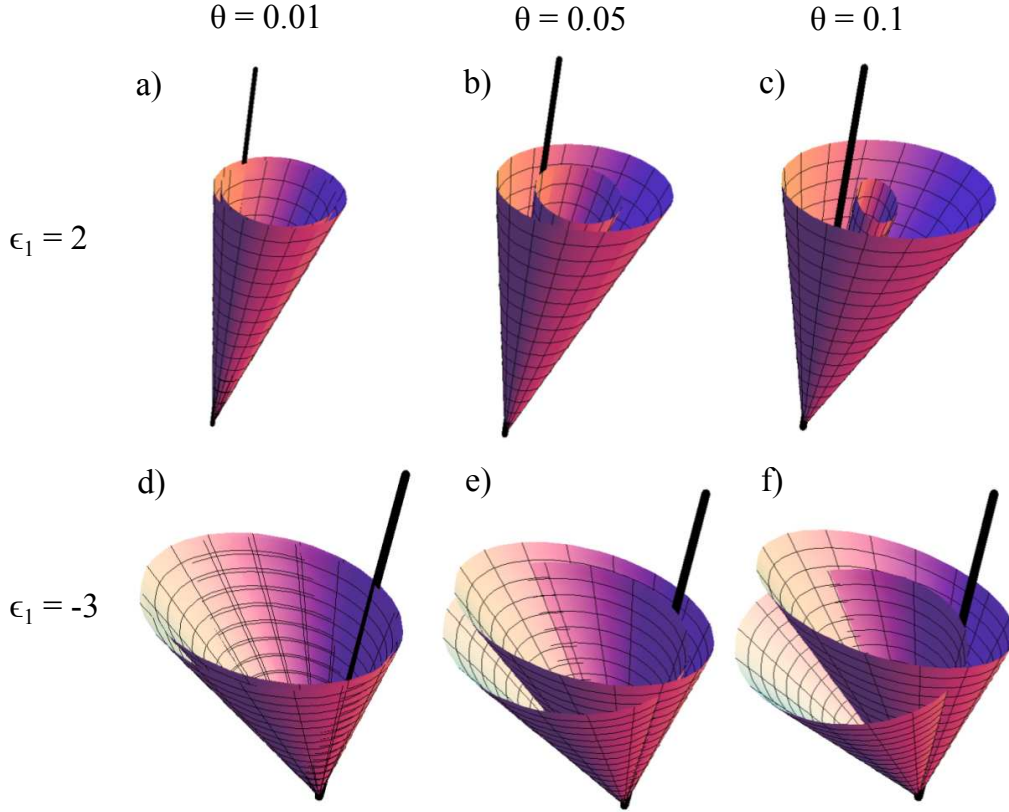


Figure 4.7: The set of possible Poynting vectors associated with each polarisation in a conventional biaxial material and a biaxial hyperbolic metamaterial, as ϕ varies from 0 to 2π . In the conventional case the cones are concentric, while in the hyperbolic case they intersect. For $\theta \rightarrow 0$ the cones are degenerate. As θ increases they move further apart. Parameters used are $\epsilon_2 = 3$, $\epsilon_3 = 4$, top row; $\epsilon_1 = 2$ (a) $\theta = 0.01$, (b) $\theta = 0.05$, (c) $\theta = 0.1$ and second row; $\epsilon_1 = -3$ (d) $\theta = 0.01$, (e) $\theta = 0.05$, (f) $\theta = 0.1$. The solid black line indicates the optic axis, while the shading is for perspective only.

$\theta = 0$ the terms which depend on ϕ take the same value for one mode at a given ϕ as for the other mode at $\phi + \pi$. As θ increases, the cones move in opposite directions along the y axis, so that they intersect and for large enough θ will separate entirely. We note that this is due to a particular term in the Poynting vector, (4.8),

$$P_y \propto \dots + \theta \left[\frac{1}{2} \left(\frac{1}{\epsilon_1} + \frac{1}{\epsilon_2} \right) (\cos \phi \pm 1) \mp \frac{1}{\epsilon_3} \right] \quad (4.9)$$

which is the dominant term for the movement of the cones as θ increases. For $\epsilon_1 \approx -\epsilon_2$, the first term in (4.9) is small, and so the two modes have terms $\approx \mp 1/\epsilon_3$ in P_y of opposite sign with little dependence on ϕ . This means the entire cones will move in opposite directions as θ increases. There is a corresponding term in the conventional case, but there if $\epsilon_1 \approx \epsilon_2 \approx \epsilon_3$ it is the constant terms $\pm 1/2\epsilon_1 \pm 1/2\epsilon_2 \mp 1/\epsilon_3$ which approximately cancel, leaving a term which is dominated by $\cos \phi$. Thus the centres of the cones do not move in this case.

4.5 Beyond geometric optics

4.5.1 Absorption

So far it has been assumed that although the permittivity may be negative it will always be real. Since hyperbolic metamaterials contain a large proportion of metal, they will always have some absorption, leading to an imaginary part of the effective permittivity. Although metals generally have high absorption, it is possible to design hyperbolic metamaterials with a small imaginary part of ϵ over a range of frequencies [147]. Nevertheless it is important to consider how losses will affect the basic theory. Previous figures have plotted the real solutions of the Fresnel equation. In directions in which only one real solution exists, the other solution is completely imaginary and thus evanescent. When the permittivity is complex, all solutions are complex, and represent waves which travel with some absorption, which depends on the size of the imaginary component.

Figure 4.8 shows the iso-frequency surface in the x_ϵ - y_ϵ plane when each principal dielectric constant has an imaginary part of $0.3i$, i.e. the absorption is isotropic. For anisotropic absorption, we would expect a splitting of each conical intersection into two branch-point degeneracies in accordance with the traditional, positive index case [148]. However, we will consider isotropic absorption here. Note a corresponding material with isotropic $\epsilon = 2 + 0.3i$ would have an imaginary refractive index of about 0.1, meaning the wave would be absorbed within ten wavelengths. Hence the imaginary part in this case is small but non-negligible. Crucially, the crossings identified in the case of real ϵ remain, and are not destroyed by the introduction of complex solutions. Furthermore they have small imaginary components meaning they describe mostly-propagating solutions with some absorption. The persistence of intersections is a result of the topological arguments described earlier, as absorption does not break the symmetry between left and right circular polarisations.

We also note that in the case of complex dielectric constants the refractive index no longer goes to infinity but is now bounded. This is purely a result of including losses, without leaving the effective medium theory. The dispersion surface bends back at finite \vec{k} , intersecting the ellipsoid surface again. This second intersection has a large imaginary component, meaning that rays in this direction will decay quickly. These new intersections also occur in other directions of $\vec{\eta}$, where they are also mainly evanescent. As the imaginary component of ϵ is increased, this finite hyperboloid shape will decrease in size, until the mostly-real and mostly-imaginary intersections approach each other and finally disappear. However, mostly-imaginary intersections also appear in the x_ϵ - z_ϵ plane which remain for large imaginary components, in keeping with our previous topological argument.

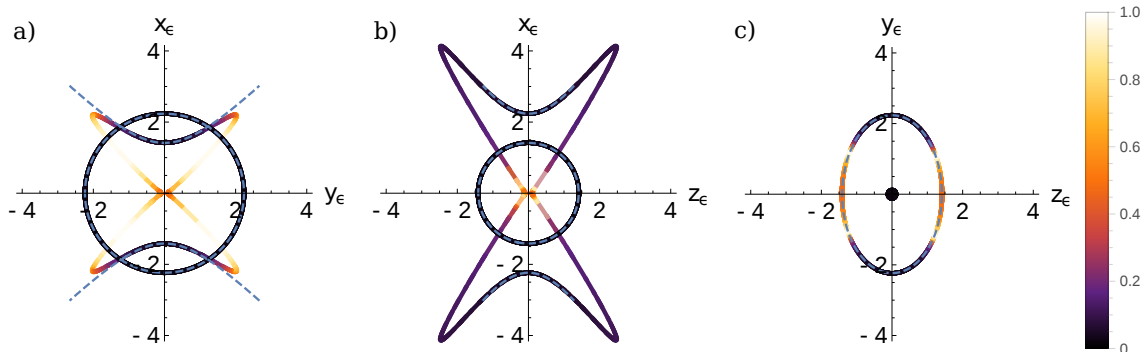


Figure 4.8: Iso-frequency surface in (a) the x_ϵ - y_ϵ plane ($z_\epsilon = 0$), (b) x_ϵ - z_ϵ plane ($y_\epsilon = 0$) and (c) y_ϵ - z_ϵ plane ($x_\epsilon = 0$) showing conical intersection in the presence of loss, with $\epsilon_1 = -2 + 0.3i$, $\epsilon_2 = 2 + 0.3i$ and $\epsilon_3 = 5 + 0.3i$, similar to the bottom right panel of Fig. 4.4. This is a polar plot of the real part of the refractive index with direction, with colour representing imaginary part of the refractive index, i.e. the absorption. White represents solutions with large absorption, and black those which are fully propagating. The original intersection remains a mostly propagating solution. An additional intersection appears which is mostly imaginary. The inclusion of an imaginary component to the effective medium theory is enough to prevent the dispersion surface becoming infinite. Dashed line shows continuation of hyperbola in case of real ϵ .

4.5.2 Diffraction

To include diffraction in the theory we follow the method of [71]. We use the angular spectrum representation to write the incoming beam as an integral of plane waves, each with a well-defined wave-vector. We can then calculate the result of propagation of each plane wave before transforming back to a real-space representation.

Describing beams propagating close to the optic axis, which we will continue to label as the x axis, the field at a position x in the crystal consists of a sum of plane wave components which pick up a phase on propagating

$$E_{\text{out}} = \iint dk_y dk_z E_{\text{in}}(k_y, k_z) \exp(i(k_y y + k_z z)) \exp\left(ix \sqrt{k_T^2 - k_y^2 - k_z^2}\right) \quad (4.10)$$

where $E_{\text{in}}(k_y, k_z)$ is the two-dimensional Fourier transform of the input field in the plane $x = 0$. However, the magnitude of the total wave-vector in the crystal k_T is nk_0 , with n depending on the direction of the ray, i.e. on k_y and k_z . We can express the refractive index (4.4) in terms of the relative transverse momentum $\vec{p} = k_\perp/k$, where $k = \sqrt{\epsilon_3}k_0$ is the magnitude of a wave-vector lying directly along the optic axis. For small θ the transverse momenta are related to the angles defined in Fig. 4.6 by $p_z = \theta \sin(\phi)$, $p_y = \theta \cos(\phi)$ and $p = |\vec{p}| = \theta$. The lowest order terms, linear in p , lead to refraction into a simple cone which dominates the diffraction pattern. To

reveal the fine structure we expand to second order giving

$$\begin{aligned} n^2 &\approx \epsilon_3 - \epsilon_\delta(p_y \pm p) + \left(\epsilon_\Delta p \pm \frac{\epsilon_\delta^2}{\epsilon_3} p_y \right) (p \mp p_y) \\ &\equiv \epsilon_3 [1 + \mu(p_y, p)] \end{aligned} \quad (4.11)$$

where

$$\epsilon_\Delta = \frac{\epsilon_3^2}{\epsilon_1 \epsilon_2} (2\epsilon_3 - \epsilon_1 - \epsilon_2). \quad (4.12)$$

Letting $k_T^2 = n^2 k_0^2 = k^2 (1 + \mu(p_y, p))$ we can expand the square root in the final exponent of equation (4.10), again to $\mathcal{O}(p^2)$ giving

$$\begin{aligned} \sqrt{k_T^2 - k_\perp^2} &= \sqrt{n^2 k_0^2 - k^2 p^2} \\ &= k \sqrt{1 + \mu(p, p_y) - p^2} \\ &\approx k \left(1 + \frac{1}{2} \mu(p, p_y) - \frac{1}{8} \mu(p, p_y)^2 - \frac{1}{2} p^2 \right) \end{aligned} \quad (4.13)$$

where we keep terms up to $\mathcal{O}(p^2)$ in μ^2 .

The integral (4.10) with the approximation (4.13) gives the paraxial approximation to the electric field at a plane $x > 0$, valid for small transverse momentum $p \ll 1$ or equivalently $k_\perp \ll k$. The term in the exponent proportional to $x p_y$ leads to a skew away from the optic axis in the cone, as suggested by figure 4.7, which can be included in the definition of a new transverse coordinate which follows the centre of the cone $\vec{r}'_\perp = \vec{r}_\perp + Ax \hat{e}_y$ such that $\vec{p} \cdot \vec{r}_\perp + Ax p_y = \vec{p} \cdot (\vec{r}_\perp + Ax \hat{e}_y) = \vec{p} \cdot \vec{r}'_\perp$. The remaining terms which depend on p_y cannot be absorbed in this way and lead to a non-circular asymmetry in the diffraction pattern.

We now consider a circularly polarised, or unpolarised, beam. The two orthogonal eigen-polarisations are present in equal amounts at each point and do not interfere with each other. If the crystal is of finite length $l < x$ then the field propagates a length l through the crystal before propagating a length $x - l$ in free space. Propagation beyond the crystal is described by an identical integral to (4.10) with the input field taken at the plane $x = l$ and with $k_T = k_0$. The intensity at a point (x, \vec{r}'_\perp) can then be written as the sum of two intensities due to each eigen-polarisation which gives

$$I = |b_+|^2 + |b_-|^2. \quad (4.14)$$

Expressing (4.10) in terms of p and using (4.13) gives

$$\begin{aligned} b_\pm(x, \vec{r}'_\perp) &= \frac{k}{2\pi} e^{ikx} \iint d^2 p a(\vec{p}) \exp(ik\vec{p} \cdot \vec{r}'_\perp) \\ &\quad \times \exp \left\{ -ikp^2 \left[\beta l + \frac{1}{2} \sqrt{\epsilon_3} (x - l) \right] \right\} \\ &\quad \times \exp(-ikl\alpha p_y^2) \\ &\quad \times \exp[\pm iklp(\gamma + \delta p_y)] \end{aligned} \quad (4.15)$$

where $a(\vec{p})$ is the Fourier transform of the input field. The parameters α , β , γ and δ can be expressed in terms of the principal dielectric constants ϵ_i as

$$\begin{aligned}\alpha &= \frac{\epsilon_\delta}{8} - \frac{\epsilon_\Delta^2}{2\epsilon_3} \\ \beta &= \frac{1}{2}(\epsilon_\Delta - 1) + \frac{1}{8}\epsilon_\delta \\ \gamma &= \frac{1}{2}\epsilon_\delta \\ \delta &= \frac{\epsilon_\delta^2}{2\epsilon_3} + \frac{\epsilon_\delta}{4} - \frac{\epsilon_\Delta}{2},\end{aligned}\tag{4.16}$$

recalling from Eqs. (4.5) and (4.12) that

$$\begin{aligned}\epsilon_\delta &= \epsilon_3 \sqrt{\frac{(\epsilon_3 - \epsilon_1)(\epsilon_2 - \epsilon_3)}{\epsilon_1 \epsilon_2}} \\ \epsilon_\Delta &= \frac{\epsilon_3^2}{\epsilon_1 \epsilon_2} (2\epsilon_3 - \epsilon_1 - \epsilon_2).\end{aligned}\tag{4.17}$$

These parameters can be used as the basic parameters of the diffraction theory and they have the following interpretations: β is a propagation constant, γ is proportional to the angle of the cone opening, and α and δ control the fine-structure of the diffraction pattern leading to circular asymmetry.

The resulting intensity Eq. 4.14 is plotted in Fig. 4.9 for a Gaussian input beam with

$$a(p) = kw^2 \exp(-k^2 p^2 w^2 / 2).\tag{4.18}$$

The beam waist w is taken as the unit length scale. The beam is plotted in the focal image plane for which $x = l - 2\beta l/n_3$ where the rings are sharpest. This is the plane in which the Gaussian beam waist would have occurred, accounting for the extra optical path length due to the crystal, and can be imaged with a lens if it occurs inside or before the material [71]. As α, β, γ , and δ all appear multiplied by l for propagation inside the crystal, the length of the crystal is only important relative to the overall scale of these parameters, e.g. a short, strongly diffracting crystal will have the same effect as a long, weakly diffracting one. The parameter γl is chosen to give a ring radius $r_0 \approx 50w$ to ensure well developed rings while the other parameters are $\alpha l = 10, \delta l = 0$. This choice allows us to show the asymmetry of the beam on the same scale as the overall conical refraction.

Like the positive ϵ case, the diffraction pattern consists of two rings. However, unlike that case these rings are broadened in the y direction but remain tight in the z direction, in agreement with Fig. 4.7 which shows the cones moving apart in the y direction with increasing p . The diffraction pattern is bounded approximately on the inside and the outside by the arcs of two intersecting circles, also in agreement with the ray diagram description. In addition there is a dark ring, called the Pogendorff ring, through the centre of the intensity pattern, which is purely an effect of

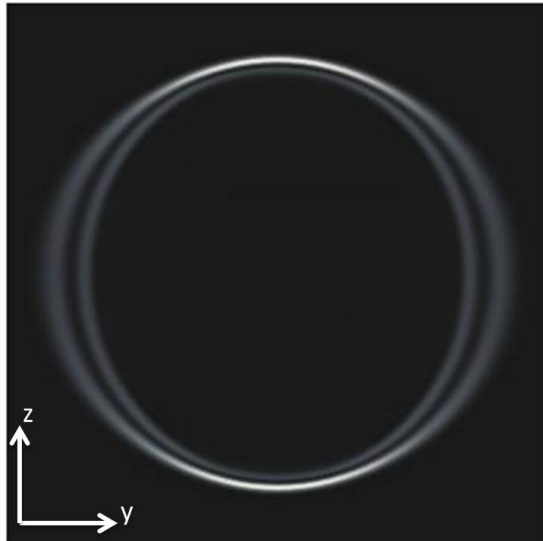


Figure 4.9: The diffraction pattern associated with conical diffraction in a hyperbolic metamaterial. The pattern is generated from the paraxial expansion (4.15) with $\alpha l = 10$ and $\delta = 0$. The transverse profile is taken at the point in the beam at which the incoming Gaussian would have been at its tightest focus.

diffraction and is not predicted by the geometrical optics theory [145]. This dark ring also appears in the conventional positive ϵ case.

4.6 Phase diagrams and possible implementation

The above results are based on an effective medium theory of a biaxial hyperbolic metamaterial $\epsilon_1 < 0 < \epsilon_2 < \epsilon_3$. These bulk dielectric constants are well defined when the features are much smaller than the wavelength. One method of constructing a biaxial HMM is to deposit an anisotropic material in thin layers with layers of metal. However, consistently depositing anisotropic material in a single crystal orientation will be difficult. Another common method of making hyperbolic metamaterials is by embedding metallic rods in a dielectric background. This leads to a negative index along the axis of the rods and a positive index in the orthogonal plane. By positioning these rods in a rectangular rather than a square pattern the two indices in the plane can be made unequal [136].

The principal dielectric constants can be calculated in the effective medium theory using the Maxwell Garnett technique [149, 150] as done for a rectangular array of metal rods in [136]. The effective dielectric constant along the axis of the rods is a simple weighted average of the metal and dielectric;

$$\epsilon_z = \rho\epsilon^m + (1 - \rho)\epsilon^d, \quad (4.19)$$

where ρ is the fraction of the unit cell which is composed of the metal element and ϵ^m and ϵ^d are the permittivity of the metal and dielectric respectively, which are

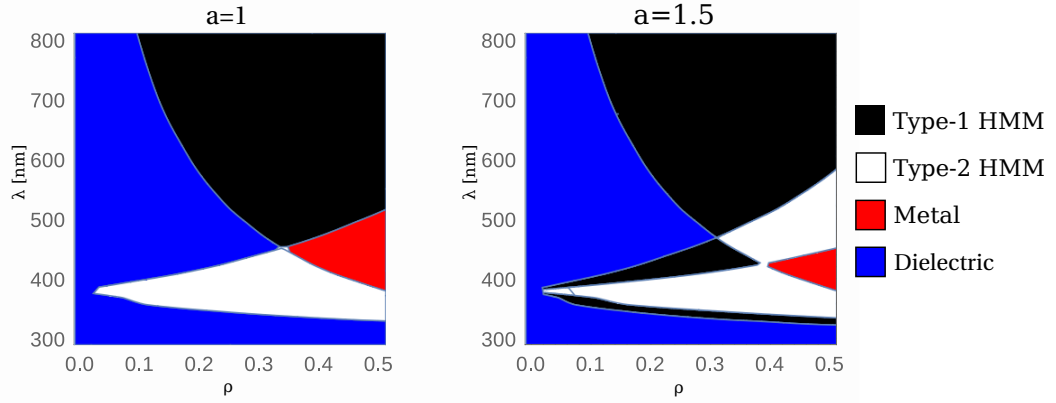


Figure 4.10: Phase diagram of silver rods in alumina in a rectangular unit cell with (a) aspect ratio $a=1$ and (b) aspect ratio $a=1.5$ as a function of filling fraction ρ , i.e. the fraction of the unit cell which consists of silver, and wavelength λ . The material is a hyperbolic metamaterial over a large range. The type-1 HMM, in which a hyperbola intersects an ellipsoid, is shown in black and is the material discussed in this chapter. When the unit cell is anisotropic additional regions open in the phase diagram as the in-plane dielectric constants can go from positive to negative at different points.

functions of the vacuum wavelength λ . The in plane components are considerably more complex. The full formula is

$$\epsilon_x = \frac{Q(\rho)\rho(a-1)\epsilon^d(\epsilon^m - \epsilon^d) + 2\pi\rho\epsilon^d\epsilon^m + \pi(1-\rho)\epsilon^d(0.32\rho(a-1)(\epsilon^m - \epsilon^d) + \epsilon^m + \epsilon^d)}{Q(\rho)\rho(a-1)(\epsilon^m - \epsilon^d) + 2\pi\rho\epsilon^d + \pi(1-\rho)(0.32\rho(a-1)(\epsilon^m - \epsilon^d) + \epsilon^m + \epsilon^d)} \quad (4.20)$$

where a is the aspect ratio of the rectangular unit cell and $Q(\rho) = \pi - 1 - \rho(\pi - 2)$. The in plane component in the other direction ϵ_y is identical with a replaced by $1/a$.

The exact implementation chosen will depend on a compromise between the desired wavelength range, transmission, biaxiality and ease of manufacturing. At visible to near infrared wavelength ranges silver has low optical losses and is a suitable metallic element [129]. Figure 4.10 shows the phase diagram for a range of metallic filling fractions and wavelengths for a rectangular array of silver nanowires embedded in an alumina background with aspect ratio of 1 and 1.5 respectively, generated by calculating the signs of ϵ_x , ϵ_y , and ϵ_z as given by Eqs. 4.19 and 4.20. The phase diagram is split into normal dielectric, normal metal, type-1 HMM and type-2 HMM. When the material is biaxial, the two in plane ϵ_{\perp} cross zero at different points, opening up additional HMM phases at lower wavelength.

The biaxiality in the type-1 regions is shown in Fig 4.11, where the figure of merit is $\sqrt{\epsilon_3} - \sqrt{\epsilon_2} = n_3 - n_2$. Also shown is the mean refractive index $n_3 = \sqrt{\epsilon_3}$. The larger this is the shorter the wavelength will be at the intersection point and the less

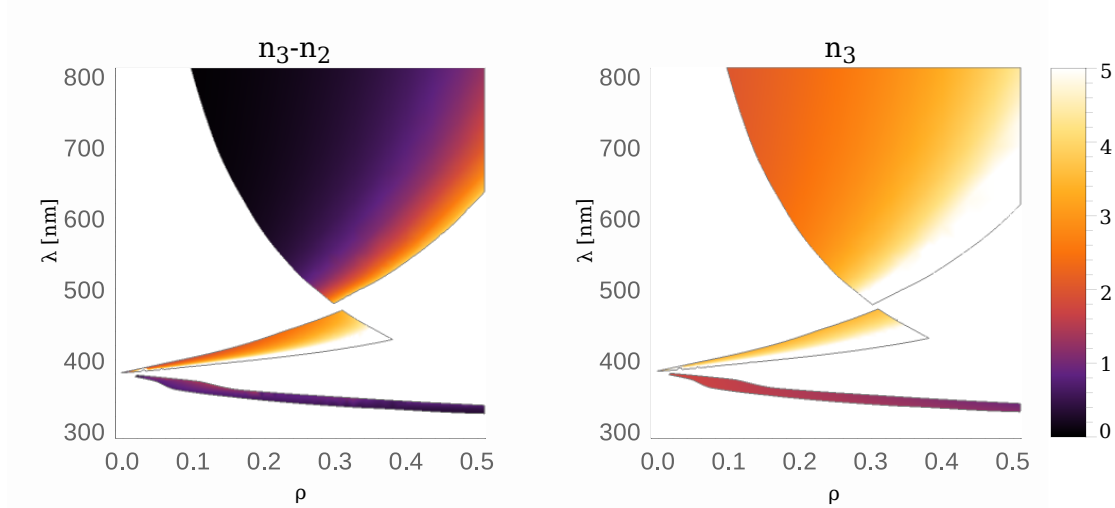


Figure 4.11: Density plots of (a) the biaxiality measured by the difference in the two positive refractive index $n_3 - n_2 = \sqrt{\epsilon_3} - \sqrt{\epsilon_2}$ and (b) the median index $n_3 = \sqrt{\epsilon_3}$ as a function of filling fraction and wavelength, in the regions where the material is a type-1 HMM, for aspect ratio $a = 1.5$. A design can be chosen from a range of values which achieves a reasonable compromise between biaxiality, median index and filling fraction.

applicable will be the effective medium theory. Again there is a range of possibilities which balance these requirements. One example is to take a rectangle with longest side 70 nm and shorter side 47 nm, with a circular rod of diameter 30 nm at the centre of each cell. This will be a type-1 HMM in the wavelengths around 700 nm. Putting $\rho = 0.18$, $A = 1.5$ we find that $\epsilon_\delta = 3.9$ which is comparable to $\epsilon_3 = 5.33$ giving strong biaxiality. The largest length scale is $70 \text{ nm} = \lambda_0/10 \approx \lambda/5$ in the material. The effective medium theory will therefore hold to a reasonable degree of accuracy close to the conical intersection. However the flexibility of HMM design means that many other compromises are possible and indeed the whole system can be replicated more easily at longer wavelengths by an appropriate material choice.

4.7 Discussion and conclusions

As discussed in the introduction of this chapter, an important feature of our results is the existence of linear intersections in the iso-frequency surface in HMMs. Such linear intersections are commonly known as Dirac points in condensed matter research, although they were identified by Hamilton in the dispersion surface of a biaxial crystal far earlier. The dispersion surface of light in a biaxial material can be related to that of a solid-state crystal in two ways. The full dispersion surface $\omega(\vec{k})$ may be compared directly with the dispersion relation of electrons in a periodic

lattice. The iso-frequency surface is then directly equivalent to a constant energy surface, such as the Fermi surface. Since the spin states of electrons are related by time reversal invariance, if the material obeys this symmetry then $\omega_+(\vec{k}) = \omega_(-\vec{k})$. Meanwhile inversion symmetry means $\omega_-(\vec{k}) = \omega_(-\vec{k})$. Hence if these two symmetries are present there can be only one sheet to each constant-energy surface. This is a case of Kramer's degeneracy. If one of these symmetries is broken then the spin up and spin down electrons can have different Fermi surfaces which may intersect, with the most common example being ferromagnetism [151]. For photons, the two polarisation states are not related by time-reversal symmetry, but by electric-magnetic duality. In the following chapter we will see that this has further consequences for the topological classification of fermionic and bosonic systems in the presence of time-reversal symmetry. Electric-magnetic duality is present if the electric and magnetic fields can be interchanged. In most materials it is broken, because $\epsilon \neq \mu$, and this allows full frequency gaps to open, for example in a photonic crystal [53]. Furthermore the topological argument employing the hairy ball theorem does not apply to the full set of allowed (ω, \vec{k}) points, as these will generically form three dimensional surfaces, and so there can be gaps between bands which describe orthogonal linear polarisations in every direction, even if these surfaces are closed.

However, the results are also closely related to condensed matter in a circuitous way via the paraxial Helmholtz equation. As we have seen in section 2.1.2 and used throughout this thesis, when we consider paraxial beams we can write the electric field as a plane wave times a slowly varying envelope function

$$E(\vec{r}) = A(\vec{r}) \exp(ikx) \quad (4.21)$$

with $A(\vec{r})$ depending weakly on x , and we have chosen x rather than z as the beam axis to be consistent with the notation in the rest of this chapter. The diffracted field given by (4.15) can then be expressed as the two-dimensional transverse input field evolving in the x-direction as

$$E(\vec{r}_\perp, x) = \exp\left(-ik \int_0^x dx' H(p, x')\right) E(\vec{r}_\perp, 0) \quad (4.22)$$

with the Hamiltonian in this case given by

$$H = \alpha p_y^2 + \beta p^2 + (\gamma + \delta p_y) \vec{s} \cdot \vec{p} \quad (4.23)$$

for $x < l$ and by the free Hamiltonian $p^2/2$ for $x > l$. Here $\vec{s} = \{\sigma_3, \sigma_1\}$ is a vector of Pauli matrices in a Cartesian basis and \vec{p} is formally represented by $-i\nabla_\perp/k$. This Hamiltonian is an extension of that for a positive index material given in section 1.3.1. The envelope function obeys the paraxial Helmholtz equation, which takes the form

$$HA = -\frac{i}{k} \frac{\partial A}{\partial x}. \quad (4.24)$$

The propagation with x of the two dimensional transverse beam is therefore equivalent to the evolution with time of a spin-1/2 wavefunction, and the paraxial Helmholtz equation is equivalent to the Schrödinger equation [152].

At a fixed frequency the propagation direction x plays the role of time and the propagation constant k_x plays the role of energy. The three-dimensional constant frequency slice of the dispersion relation can thus be seen as a dispersion relation for the propagation constant as a function of the two transverse momenta k_y, k_z . In this picture the point intersections in the iso-frequency surfaces correspond to the Dirac points for two-dimensional electrons. Dirac points in two dimensional materials have been used as a basis for topological insulators and topologically protected edge states [153, 154] due to the time reversal symmetry relation between the two sublattices [3]. This topological protection has been exploited in photonic systems using both the full frequency dispersion [51, 53] and more recently the paraxial dispersion of the propagation constant [54, 55]. Understanding the effects of different symmetries on these two dispersion relations could therefore help progress towards topologically protected photonic systems.

The results of this chapter illustrate the unique singularities found in hyperbolic metamaterials when all three indices are allowed to vary independently. By examining the full dispersion surface of a general, biaxial, hyperbolic metamaterial, we have identified conical singularities at which the refraction direction is not defined. We have found the approximate dispersion surface and the refracted Poynting vector for a ray travelling close to the axis of these singularities. We have shown that this leads to a new form of refraction which does not appear in the usual uniaxial HMMs and is topologically and quantitatively different from the phenomenon of conical refraction which occurs in ordinary biaxial materials. These propagating solutions remain when a small imaginary component is included, leading to a small amount of absorption, with additional mostly evanescent singular solutions also appearing. We have also calculated the diffraction pattern for a beam travelling through such a material. We have found that the diffracted beam is generally not circularly symmetric and that, similar to the positive ϵ case, a dark ring appears where ray optics predicts the largest intensity.

We have presented this work as a generalisation of the theory of hyperbolic metamaterials to the more general case where the two positive dielectric constants are unequal. However, it can also be seen in the context of extensions of conical diffraction to new materials. In this context this work joins a collection of important extensions to the theory including the consideration of chirality [155], anisotropic absorption [148], and nonlinearity [156].

Chapter 5

Gauge fields and topological invariants

5.1 Introduction

In chapter 4 we described a photonic medium in terms of the iso-frequency surface, which relates the frequency of light to the wave-vector and the polarisation. This surface also gives the phase of a plane wave under propagation, through the paraxial wave equation. Indeed, the full dispersion relation $\omega_n(\vec{k})$ usually provides a sufficient characterisation of any photonic system. In recent years however, topology has begun to emerge as another key ingredient. This originates from the study of electrons in periodic crystals. These are characterised by bands describing the discrete energy levels which exist at each value of the crystal wave-vector. Two energy bands which look similar at any point \vec{k} , can have a different global structure over the whole k -space which means one cannot be smoothly deformed into the other. This global property of each band has important implications. Properties which rely on the topology of the bands cannot vary smoothly and so will be extremely robust to disorder as long as there is a well defined bulk material [38].

In recent years the theory of topological order has emerged as a key ingredient in a range of new contexts, from cold atoms [157, 158] to paraxial optics [51, 52, 54]. Interest stems from the discovery of a new phase of matter, the topological insulator [159, 3, 160], characterised by edge states that are immune to backscattering [25, 161]. An important example is the edge states which carry current in the quantum Hall effect. Since this theory of topological order has been transcribed to photonic systems, it has led to applications such as topologically protected wave

guides which are robust against disorder [162, 163, 57, 56, 53, 55]. In particular, in a periodic system each band has an integer associated with it, known as the Chern number, which is invariant under smooth deformations of the system which do not close the gap between bands [38, 3, 164, 10]. Since this number cannot change without closing the gap, it follows that the gap must close at the interface between two materials whose bands have different Chern numbers. This is the origin of the edge states mentioned above.

In this chapter we present some initial work concerning the geometry and topology of the Hamiltonian in the paraxial wave equation, allowing for spin-orbit coupling which mixes polarisations. We first point out (section 5.2) that in the presence of such coupling the approach used to calculate a topological invariant in Refs [54, 57, 165] fails. We identify the formula required to compute this invariant in the case of a general paraxial Hamiltonian (section 5.3.2). This formula is linked to the presence of a non-Abelian gauge field, as discussed in section 5.3. As a first application, in section 5.4 we calculate both the gauge field and the invariant for a chiral biaxial material. In the remainder of this section we review some background literature on topological order in electronic and photonic systems.

The aim of this chapter is therefore to introduce the role of polarisation into the study of photonic topological insulators. To this end we review material which may be familiar in the context of polarisation and crystal optics, but rewritten in the context of topological invariants familiar from the study of topological phases in condensed matter. This re-framing however will lead to the novel result that the current topological classification of photonic materials is incomplete when non-uniform polarisation is to be considered, and also to the novel claim that a new invariant associated with the group $U(2)$ should be used instead. As this work is incomplete, the full implications are not explored, but it is included as a suggestion of a direction for further research.

5.1.1 Geometric phase

As discussed in the introduction, particularly section 1.2, and above, the Chern numbers depend on the concept of the geometric or Berry phase [23], which describes how the wavefunctions vary during some cyclic process. The topological quantity, which is a global property of the system, can be calculated from the geometric phase. When a quantum mechanical particle evolves in time it acquires a dynamic phase related to the Hamiltonian

$$\psi \rightarrow e^{-i \int \hat{H}(t') dt' / \hbar} \psi, \quad (5.1)$$

but the wave function can also acquire a phase due to its geometric path in configuration space. We will now justify the results we stated in chapter 1, in particular

Eqs. 1.4 to 1.8. Again, consider a state which depends on some slowly varying parameter λ with instantaneous eigenstates

$$H(\lambda) |n(\lambda)\rangle = \epsilon_n(\lambda) |n(\lambda)\rangle. \quad (5.2)$$

If the phase varies continuously as λ is varied, we can write

$$\begin{aligned} \langle \psi(\lambda) | \psi(\lambda + \delta\lambda) \rangle &= |\langle \psi(\lambda) | \psi(\lambda + \delta\lambda) \rangle| e^{-i\delta\phi} \\ &\approx e^{-i\delta\phi} \approx 1 - i\delta\phi \\ \Rightarrow \delta\phi &= i \langle \psi(\lambda) | (|\psi(\lambda + \delta\lambda)\rangle - |\psi(\lambda)\rangle) \\ &\approx i \langle \psi(\lambda) | \nabla_\lambda \psi(\lambda) \rangle \Delta\lambda. \end{aligned} \quad (5.3)$$

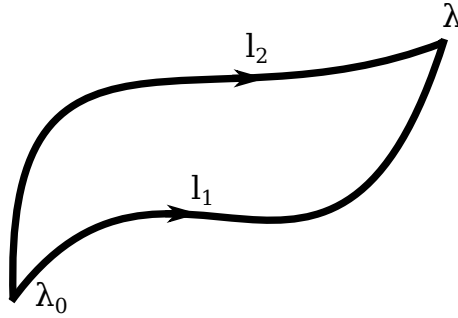


Figure 5.1: Illustration of how the phase at a given point can depend on the path. If the phase at the point λ when travelling along the paths l_1 and l_2 is not equal, then the phase gained when travelling along the closed loop composed of travelling along l_1 , then backwards along l_2 , will not be zero.

Of course, the phase at any value of the parameter can be absorbed into the definition of state by means of a gauge transformation

$$|\psi(\lambda)\rangle \rightarrow e^{if(\lambda)} |\psi(\lambda)\rangle. \quad (5.4)$$

Since only the relative phase between two fields is observable, Eq. 5.4 is equivalent to a local choice of reference phase at each point in the parameter space. If approaching a point along two different paths leads to different accumulated phases however, then the difference between these phases does not depend on the choice of gauge. The difference between the integrals along the two paths is equivalent to the integral along a loop first along one path then back along the other. Hence the integral over a closed loop,

$$\oint d\vec{\lambda} \langle \psi(\lambda) | \nabla_\lambda \psi(\lambda) \rangle \equiv \oint \vec{A} \cdot d\vec{\lambda}, \quad (5.5)$$

is gauge invariant and so is a physically meaningful quantity [166, 167]. By Stokes' theorem, the line integral of the Berry connection \vec{A} around a closed loop is equal to the integral of the Berry flux

$$\vec{F} = \nabla_\lambda \times \vec{A} \quad (5.6)$$

over the surface enclosed by that loop.

The phase picked up by an electron orbiting a solenoid, known as the Aharonov Bohm effect [32] and described in section 1.2.3, is an important example of the Berry phase. In fact, the similarity between the quantities A and F , and the description of an electromagnetic field in terms of a vector potential, is not a coincidence. We are calculating how the phase of a scalar function varies around a loop. It is just this ($U(1)$) gauge symmetry which couples charged particles to magnetic fields in quantum mechanics. This is done by demanding that the Hamiltonian is invariant under the local gauge transformation

$$\psi \rightarrow e^{if(\vec{x})}\psi \quad (5.7)$$

$$\vec{A} \rightarrow \vec{A} - \frac{1}{q}\nabla f(\vec{x}) \quad (5.8)$$

where in this context \vec{A} is the vector potential for a real magnetic field and q is the particle's charge. This is a symmetry of the Schrödinger equation with minimal coupling

$$(-i\nabla + q\vec{A})\psi \rightarrow (-i\nabla + q\vec{A} - \nabla f(\vec{x}))e^{if(\vec{x})}\psi \quad (5.9)$$

$$= e^{if(\vec{x})}(-i\hbar\nabla + q\vec{A})\psi. \quad (5.10)$$

Hence it is the $U(1)$ gauge symmetry of the wavefunction which couples it to the electromagnetic field.

5.1.2 Topological insulators

Historically, the first example of topological order was found in the quantum Hall effect. This effect is related to the Berry phase of electrons confined to two dimensions in a periodic potential [25]. For a periodic crystal, a natural parameter to consider is the crystal wave-vector \vec{k} . Bloch's theorem states that in a periodic potential the wavefunction can be written as a plane wave multiplied by a function with the same discrete periodicity as the potential. The total wavefunction is

$$\psi_{\vec{k}}(\vec{r}) = e^{i\vec{k}\cdot\vec{r}}u_{n,\vec{k}}(\vec{r}), \quad (5.11)$$

where $u(\vec{r})$ has the same periodicity of the medium. This follows from the required properties of the solution under a discrete translation operator (and so electromagnetic fields in a periodic medium also take this form). The wavefunctions are also periodic in k , and the Brillouin zone, which is the space of independent k vectors, is topologically equivalent to a circle, torus etc. depending on dimension [168]. The Berry connection in reciprocal space is defined by

$$\vec{A}_n(\vec{k})^j = i \left\langle u_n(\vec{k}) \left| \nabla_k^j \right| u_n(\vec{k}) \right\rangle, \quad (5.12)$$

as in equation (5.3), with \vec{k} now taking the place of the parameters $\vec{\lambda}$. Here n labels the bands while j runs over the two dimensions of \vec{k} . This describes how the phase of the Bloch state changes with \vec{k} in a small neighbourhood, and clearly depends on the choice of phase for the functions $|u_n(k)\rangle$. Again, however, the accumulation of phase around a closed loop is a gauge-independent quantity. In particular the phase change around an infinitesimal loop is

$$\vec{F}_n = \nabla_k \times \vec{A}_n(k). \quad (5.13)$$

By Stokes theorem, the flux of F through an enclosed area is equal to the line integral of A along its boundary, and this quantity is independent of the choice of phase for the state at each point. The flux of F through the entire Brillouin zone is equal to the phase accrued when a loop is completed around the entire edge, and hence must be equal to 2π times an integer, known as a Chern number [25],

$$C_n = \frac{1}{2\pi} \int_{BZ} d\Omega \cdot F_n(k) \in \mathbb{Z}. \quad (5.14)$$

It may seem like this integer must be zero, since the line integral traverses opposite edges of the Brillouin zone, which by Bloch's theorem are equivalent, in opposite directions. In fact, this would be the case if the Bloch functions could be smoothly defined everywhere. However, it may happen that it is impossible to choose a single smooth phase function, and this leads to coordinate singularities, which contribute a flux \vec{F} through the Brillouin zone [169]. This is equivalent to the condition mentioned previously for a non-trivial Berry phase to be acquired over a closed loop. If there is a point where the coordinates cannot be defined smoothly, then Eq. 5.4 cannot account for the phase picked up over a closed loop around this point, and the phase at any point depends on the path taken. Since the gauge transformation which changes the phase at each point \vec{k} consists of simply multiplying by a complex number of unit modulus, it is described by the group $U(1)$, and we will sometimes refer to the Chern number associated with the phase of a scalar field as a $U(1)$ invariant.

Because the Chern number is an integer, it cannot be varied continuously. The only possibility for a Chern number to change is when two bands cross, so that the Berry connection Eq. 5.12 is not defined for each band individually, as the separation of the states into two different levels is not unique. The link between band degeneracies and winding numbers was first pointed out by Simon [10]. When the gap between two bands closes the flux can be transferred from one to the other. However, the sum of the winding numbers of both bands is conserved [10, 154]. In this way insulators, or photonic crystals with a band gap at a certain frequency, are characterised not just by their band structure, but also by the Chern number of each band below that frequency. If two different insulators, each with a band gap

but with different topological quantities, are brought next to each other, then there must necessarily be a band closing, and therefore a conductive state, at the surface in order to rectify the topological mismatch [25, 39]. This is the basis of topological insulators in electronic, and more recently in photonic, systems.

Topological edge states of this kind require the breaking of time reversal symmetry. This is because time reversal symmetry requires $F(-\vec{k}) = -F(\vec{k})$ while spatial inversion symmetry requires $F(-\vec{k}) = F(\vec{k})$. Clearly the combination of these two requirements forces the Berry flux to be identically zero everywhere, while the presence of time reversal symmetry alone is enough to guarantee that the Chern number is zero, as the contributions from time reversed points cancel, and so the integral over the whole Brillouin zone will be zero.

5.1.3 Photonic topological insulators

In electronic systems such as the quantum Hall state, time reversal symmetry can be broken by an external magnetic field. However, it is worth noting that the term topological insulator may also refer to another type of topological invariant which has been proposed in the presence of time reversal symmetry [170, 160]. This is a \mathbb{Z}_2 invariant ($\nu \in \{1, 0\}$) which counts the number of phase windings in the half of the Brillouin zone containing independent \vec{k} vectors [153, 171]. This \mathbb{Z}_2 invariant is due to Kramer's theorem, which guarantees that every state of a time-reversal invariant fermionic system is doubly degenerate. Due to the differing nature of the time-reversal symmetry for bosons and fermions, however, Kramer's theorem does not apply to photons. Barring accidental degeneracies, the energies of left and right circular polarised photons are different for $k \neq 0$, even at time reversal invariant points, and so there is no \mathbb{Z}_2 topological invariant. Photons can scatter into their time reversed state [58]. It may be possible to have edge states which are protected by other, similar symmetries. One example is in a spin degenerate metamaterial, where permittivity and permeability are equal [53]. In this case the states are protected not by time reversal symmetry, but by symmetry under exchange of electric and magnetic fields.

Because photons are neutral particles, breaking time reversal symmetry is more difficult than it is for electrons. Explicit time-reversal symmetry breaking, using a magnetic field and the Faraday effect, has been considered [51, 52]. An alternative is to use an artificial gauge field [57, 172, 164]. These artificial gauge fields are obtained by creating a system where the phase of the particle changes during some cycle, with the equivalent magnetic flux through any closed loop given by the change of phase around that loop [173]. This can be achieved for example through a spatial lattice with position dependent hopping parameters [57] or by controlling an internal degree of freedom [174, 175]. These artificial magnetic fields have opened a new range of

applications for controlling light, and replicating the physics of electrons in magnetic fields [176, 177, 59].

A related idea can be understood by looking at the paraxial approximation to the Helmholtz wave equation, Eq. 1.26. The beam propagation direction z takes the place of time in the Schrödinger equation. Hence a material which breaks z -reversal invariance is the paraxial equivalent of a two-dimensional electronic system with broken time reversal invariance, leading to topological protection [54].

These current approaches to generating artificial gauge fields for light generally assume that two polarisations, or similar degrees of freedom, decouple. This allows artificial gauge fields to appear in each polarisation, but leaves open the possibility that the overall gauge field is trivial. For example, the proposal by Rechtsman et al., assumes that only one polarisation is present [54]. Similarly that by Hafezi et al [57], for topologically robust delay lines, assumes that countercirculating resonator modes are decoupled, and so it is possible to selectively drive one or the other. In these cases, Eqs. 5.12 to 5.14 can be applied to each polarisation individually. However, polarisation coupling might destroy the topological order. For example back-scattering from one polarisation into the other could mix edge states, causing a gap to open.

In order to be sure of true topological protection, we need to find an invariant which accounts for the propagation and coupling of both possible polarisations. In this chapter we will show that when both polarisation and phase vary we can describe the evolution with a non-Abelian gauge field, in contrast to the Abelian magnetic field which describes varying phase only. Non-Abelian fields play a central role in fundamental high-energy physics. Since being introduced by Wilczek [178, 179] artificial non-Abelian fields have been proposed in systems ranging from polaritons [180] to cold atoms [181, 182, 183, 184]. We show that there is an integer, derived from our non-Abelian field, which characterises the topological order of both orthogonal polarisations. This integer is a topological invariant even in the presence of polarisation mixing. Although this quantity is, we believe, a Chern number in the general sense [185, 186], it is not generally given by applying Eqs. 5.12 to 5.14 to a single sheet of the dispersion surface.

Non-Abelian gauge fields in optics have been studied previously, noticeably by Bliokh. Indeed [187] explicitly constructs a non-Abelian evolution operator for light rays in an anisotropic medium. Previous work concentrates on the dynamics of wavepackets travelling under the influence of such a non-Abelian field, and shows that rays of light experience a polarisation dependent deflection and a precession of the Stokes vector [187, 188]. We argue that this type of non-Abelian gauge field can be applied to the description of photonic bands in a periodic system in the paraxial approximation, and derive a topological invariant associated with the windings in

the gauge field. This invariant may be of use in future work designing systems with robust edge states in the presence of polarisation coupling.

5.2 $U(1)$ invariants in the presence of polarisation coupling

The $U(1)$ invariant discussed in section 5.1.2 describes phase windings in scalar fields. For a vector field, we may naively attempt to calculate the Chern number by applying Eq. 5.14 with a dot product over the vector index in Eq 5.12. Indeed when the two polarisations (or spins) are not coupled, we can treat each as a scalar field, and calculate the resulting band structure. Since the polarisations are decoupled, there will be edge states between trivial and non-trivial materials which lead to spin polarised transport. Since there is no coupling between polarisation, photons of one spin will not scatter into the orthogonal polarisation. However, when the polarisation is allowed to vary, and there is coupling between the two polarisations, these edge states will no longer be robust, and the bands of each polarisation cannot be treated separately. To illustrate this, we will consider a particular effective medium, where the polarisation described by each band is allowed to vary with \vec{k} . We will show that in this case the $U(1)$ winding number of a loop in k space may not be an integer.

5.2.1 Example: chiral biaxial material

As we have seen previously, for example in sections 1.3.1 and 2.1.2, the evolution of a paraxial beam of light along the axis of the beam (taken to be the z axis) is described by the paraxial wave equation with a form identical to the Schrödinger equation [50, 99] for a particle in two dimensions

$$\hat{H}\vec{E} = ik_z \frac{\partial \vec{E}}{\partial z}, \quad (5.15)$$

where the paraxial Hamiltonian, which depends on the material in question, acts on the two-dimensional transverse electric field envelope $\vec{E} = (E_x, E_y)^T$.

When we say that the polarisations decouple for a particular system, we mean that the Hamiltonian is simultaneously diagonalisable at each point in k -space. For example in a homogeneous, isotropic medium the Hamiltonian is simply that associated with a free particle $\hat{H} = -\nabla_{\perp}^2/2 \equiv k_0^2 p^2/2$, where $\vec{p} = \vec{k}_{\perp}/k_0$ is the transverse momentum divided by the vacuum wave vector. A more complex paraxial Hamiltonian describes materials which are inhomogeneous, chiral etc. However, as long as the Hamiltonian is diagonalisable we can treat each polarisation component

separately. For a material periodic in x and y we use the Bloch functions to calculate the Berry phase

$$A_\mu^\sigma = i \langle \sigma, k | \nabla_\mu | \sigma, k \rangle, \quad (5.16)$$

which gives the phase of each scalar field in terms of the phase at a fixed point k_0 and a path C linking the two points

$$|\sigma, k\rangle = \exp\left(i \int_C \vec{A}^\sigma \cdot d\mathbf{l}\right) |\sigma, k_0\rangle. \quad (5.17)$$

From this we can calculate the Berry curvature

$$\vec{F}^\sigma = \vec{\nabla} \times \vec{A}^\sigma. \quad (5.18)$$

The Chern number associated with each polarisation is the integral of the Berry curvature over the Brillouin zone divided by 2π and is an integer [38];

$$C_\sigma = \frac{1}{2\pi} \iint_{BZ} \vec{F}^\sigma \cdot d^2k. \quad (5.19)$$

We now consider a material which is not simultaneously diagonalisable at different k -points, a chiral biaxial material. We have already seen the paraxial Hamiltonian for propagation close to the optic axis of a biaxial material, Eq. 1.24. For convenience, it is repeated here;

$$\hat{H} = \frac{1}{2}p^2\mathbb{I} + \vec{S} \cdot \vec{Q}. \quad (5.20)$$

Here $\vec{S} = \{\sigma_1, \sigma_2\}$ is the vector of Pauli matrices in a circular polarisation basis and $\vec{Q} = \{Ap_x, Ap_y\}$ where A is a measure of the biaxiality of the medium. Since \hat{H} is a linear combination of Pauli matrices whose coefficients depend on p , it will not commute at different points;

$$\left[\hat{H}(\vec{p}), \hat{H}(\vec{p}')\right] = A[p_x\sigma_x + p_y\sigma_y, p'_x\sigma_x + p'_y\sigma_y] \quad (5.21)$$

$$= 2iA(p_x p'_y - p'_x p_y)\sigma_z. \quad (5.22)$$

Since this is generally non-zero, the matrix cannot be diagonalised simultaneously at different \vec{p} .

The bands for a biaxial material, which are the eigenvalues of the Hamiltonian 5.20 as a function of p , are plotted in Fig. 5.2(a). As we saw in chapter 4 in the absence of chirality, these bands are the paraxial approximation to the dispersion surface. They give the propagation constant k_z , which plays the role in the paraxial wave equation 5.15 played by energy in the Schrödinger equation. This propagation constant is expressed in terms of the (small) off-axis momentum \vec{p} , by solving the relation $\omega(\vec{p}, k_z) = \omega_0$, expanded in powers of p . As Eq. 5.20 stands, there are two bands, one for each polarisation. With the addition of a periodic potential

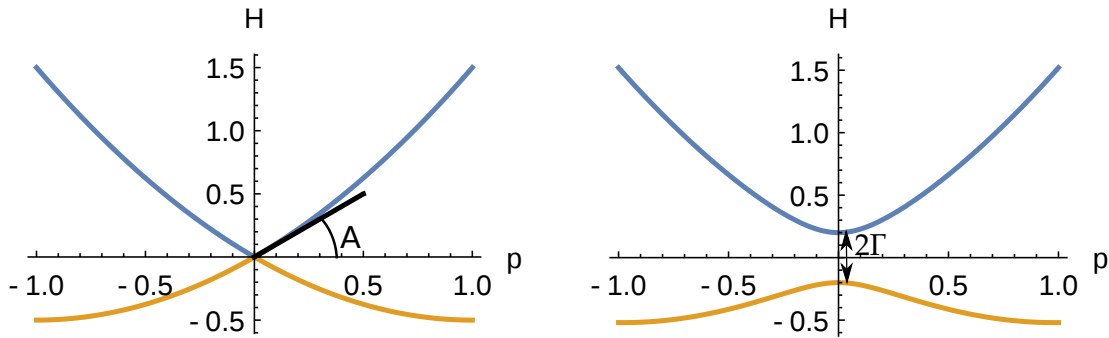


Figure 5.2: Energy levels of Hamiltonian Eq. (5.20), which represent the paraxial propagation constant nk_0 as a function of the transverse momentum p , with $\Gamma = 0$ and $\Gamma = 0.2$.

(varying average refractive index) these bands would fold back at the Brillouin zone boundary.

Since there is no gap we cannot unambiguously label each band and so we cannot calculate the Berry flux through each band. To open a gap we introduce a small chirality Γ [155]. The Hamiltonian, Eq. 5.20, has the same form but there is now a constant energy splitting between right and left circular polarisations given by a term proportional to σ_z ,

$$\vec{S} = \{\sigma_1, \sigma_2, \sigma_3\} \quad (5.23)$$

$$\vec{Q} = \{Ap_x, Ap_y, \Gamma\}. \quad (5.24)$$

The eigenvalues of this Hamiltonian, which give the propagation constant as a function of the perpendicular momentum for each polarisation, are

$$H_{\pm} = \frac{1}{2}p^2 \pm A\sqrt{p^2 + \gamma^2} \quad (5.25)$$

with $\gamma = \Gamma/A$. These are shown in Fig. 5.2(b). The chirality lifts the degeneracy between the two bands at $p = 0$ which would otherwise form a conical intersection, and allows us to consider the winding number of each band separately.

The bandstructure described by the eigenvalues, Eq. 5.25, is the paraxial approximation to the iso-frequency surface similar to those described in chapter 4, but with the addition of chirality. In this approximation the bands are infinite, but we will be primarily concerned with the Berry curvature in a region near $p = 0$. As we shall see the size of the non-trivial region is determined by γ . In the following we will mainly be concerned with loops in k -space which will not necessarily coincide with the Brillouin zone of a periodic crystal. If some periodicity is introduced then there may be additional flux at the Brillouin zone boundary. If the periodicity is over a length scale a then the bands will fold back at the Brillouin zone boundaries at $|p| \approx \pi/a$. If $\gamma \ll \pi/a$ then the flux through the centre of the band will be of primary importance for the paraxial approximation.

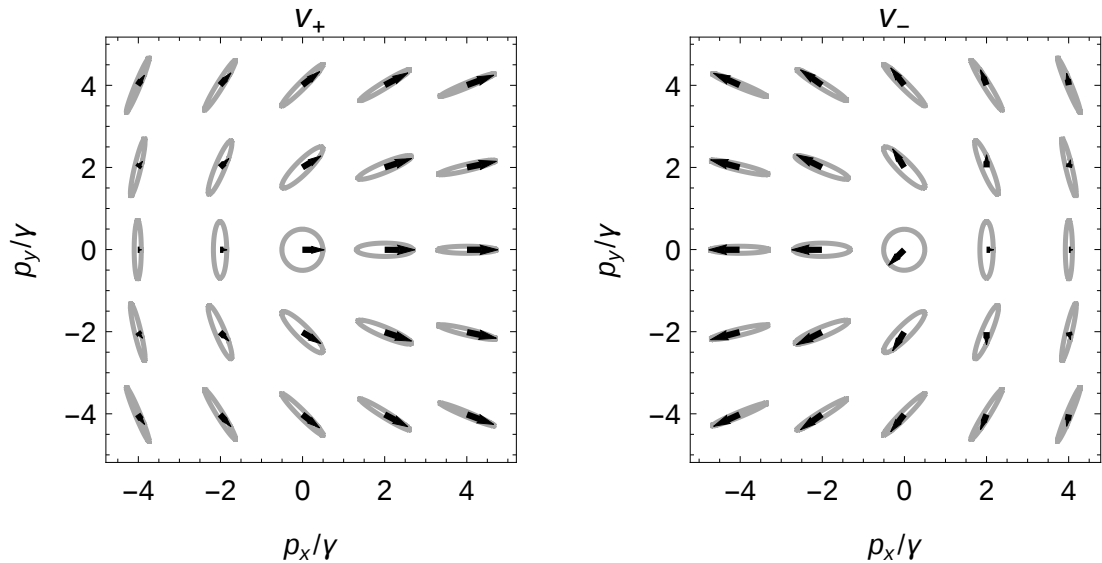


Figure 5.3: Polarisation and instantaneous field of the eigenvectors of Eq. (5.26) in a Cartesian basis. The fields are circular at the centre and increasingly elliptical away from the origin. The angle of polarisation rotates by π around the centre as the phase also increases by π . Note that depending on the choice of sign of γ , the elliptical polarisation in v_+ advances clockwise and in v_- anti-clockwise or vice-versa.

Outside of the paraxial approximation, i.e. for large p , the surfaces of 5.2 continue to curve, and the lower surface will cross the gap again rather than continuing to separate. The whole surfaces will be similar to Fig. 4.3(c), with the addition of gaps at each intersection point. However, neglecting the wider surfaces is equivalent to neglecting scattering from paraxial rays to non-paraxial rays, which are outside the scope of the paraxial approximation. Additionally, we have seen in the previous chapter that allowing a negative dielectric constant means the two surfaces will have opposite curvature, and will not cross the gap even outside the paraxial approximation. Such a system with uniaxial anisotropy was considered in [55], and was argued to be a photonic topological insulator.

The normalised eigenvectors of Eq. 5.20 with chirality (i.e. using Eq. 5.23) are

$$\hat{v}_{\pm} = \begin{pmatrix} \gamma \pm \sqrt{p^2 + \gamma^2} \\ p e^{i\phi} \end{pmatrix} \frac{1}{\sqrt{2} \sqrt{p^2 + \gamma^2 \pm \gamma \sqrt{p^2 + \gamma^2}}}. \quad (5.26)$$

These are plotted in Fig. 5.3. Here $\phi = \arctan(p_y/p_x)$ is the angle in momentum space. We plot the real part of the vector, to show the relative phase at different points, as well as the polarisation ellipse traced out by $\text{Re}[\exp(i\omega t)\hat{v}_{\pm}]$. At the origin, the modes are circularly polarised with the chirality splitting the propagation of left and right polarisations. Away from the origin both beams become increasingly linearly polarised. Note that around either eigenmode there is a π rotation of the

angle of elliptical polarisation. This pattern is similar to the conical refraction beam, but the presence of the σ_z term means the eigenfields are well defined, even at $p = 0$.

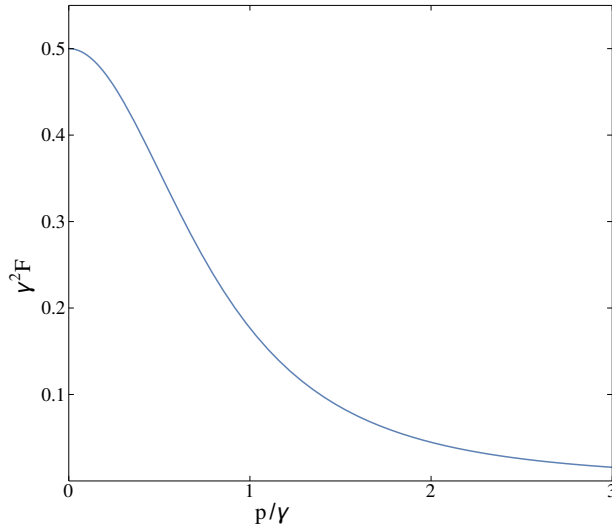


Figure 5.4: Cross section of Berry flux for lower band of a chiral biaxial material calculated using Eq. 5.12 to 5.14 and taking the dot product over the vector index. It is finite at $p = 0$ and falls off with increasing p in a range $\sim \gamma$.

Since, in the presence of chirality, the band-structure consists of two separate bands, we might naively attempt to calculate the Berry phase around some loop of each band separately, using Eq. 5.14, much as we would calculate the Chern number of each non-degenerate energy level in an electronic band structure. However, calculating the Berry flux of the lower band gives

$$F = \frac{\gamma}{2(p^2 + \gamma^2)^{3/2}}. \quad (5.27)$$

This is plotted in Fig. 5.4. This flux, in units of $1/\gamma^2$, is centred around $p = 0$ with a full width half-maximum of $\approx 0.76\gamma$. The integral of F over the whole sheet is π . Hence the Chern number appears to be

$$C_n = \frac{1}{2\pi} \oint F \cdot d\Omega = \frac{1}{2}, \quad (5.28)$$

which is not an integer. Of course, this calculation is over an open sheet and not a periodic Brillouin zone. However the flux is zero away from the centre of the band and for a scalar field this calculation would tell us the winding of the phase around this central point. Even though at each point in k -space the lower band describes a single polarisation, this polarisation varies around k -space and so this naive approach to calculating the invariant fails.

5.2.2 Homotopies between $U(1)$ vortices

To make further progress in understanding the invariants associated with loops in k -space when polarisation varies, it is helpful to introduce the mathematical concept of a homotopy class [11]. One way of describing a topological space is to consider closed paths in this space, and to identify paths which can be smoothly deformed into each other. Two paths are homotopic if there exists a continuous function which interpolates between them while always keeping the start and end points fixed. In a space such as \mathbb{R}^n , any two paths are homotopic. However, in a space such as $\mathbb{R}^2 - \{0\}$, paths which wind around the origin a different number of times are distinct. The equivalence class of paths, i.e. the set of all distinct paths, is called the homotopy group, denoted by π . The homotopy group of $U(1)$, denoted

$$\pi(U(1)) \sim \mathbb{Z}, \quad (5.29)$$

is isomorphic to the integers. Since an element of $U(1)$ is just a complex number of unit norm, the homotopy class can be described by the integer number of times the phase changes by 2π around the loop. This is why the $U(1)$ Chern number, which counts the number of times the $U(1)$ phase in the wavefunction changes around singular points, is an integer.

However, when polarisation is allowed to vary, a path in the space of possible two-dimensional fields which contains a phase vortex is actually homotopic to a path with no vortex, i.e. one can be smoothly deformed into the other. For example consider the field $\exp(i\phi)(1, 0)^T$, with ϕ parameterising some closed loop in k -space. This loop has $U(1)$ Chern number $C = 1$, but can be smoothly deformed to the trivial loop $(0, 1)^T$ by the homotopy

$$E(\phi, t) = \begin{pmatrix} e^{i\phi} \cos(t\pi/2) \\ \sin(t\pi/2) \end{pmatrix} \quad (5.30)$$

with $t \in [0, 1]$. This homotopic transformation is shown in Fig. 5.5. Considered as a function of t , this map smoothly interpolates between $E(\phi, 0) = e^{i\phi}(1, 0)^T$ and $E(\phi, 1) = (0, 1)^T$. In addition for any t , although the endpoint doesn't remain fixed, the loop remains closed, i.e. $E(2\pi, t) = E(0, t) \forall t$, and so the transformation is a smooth homotopy. The resulting vortex free field can be returned to the same polarisation $(1, 0)^T$ as the initial field by a similar deformation.

5.3 Non-Abelian gauge fields in paraxial optics

The reason why the $U(1)$ invariant does not capture the full change in the field over a closed loop is that we cannot write a general two dimensional complex field at some point in k space as simply a phase times the field at a reference point, as we did

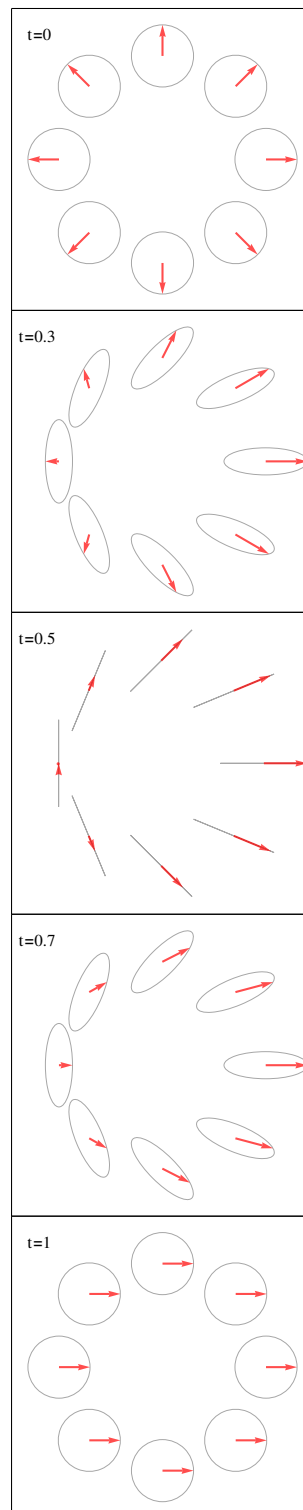


Figure 5.5: Illustration of homotopy, given by Eq. 5.30, between a field with a vortex and a field with uniform phase. As the parameter t varies, the homotopy smoothly interpolates between a circular polarised field with a phase vortex, through varying elliptical polarisation, to a field which is uniformly circularly polarised with uniform phase.

for a scalar field in Eq. 5.17. In the following we will be considering the eigenvectors of Hermitian Hamiltonians which appear in the paraxial wave equation. These have orthogonal eigenvectors which are always normalisable, and are uniquely defined so long as the Hamiltonian has no degeneracies. The most general relation between such a field at two ends of a path is

$$\vec{E}(\vec{p}) = U(\vec{p}, \vec{p}_0) \vec{E}(\vec{p}_0) \quad (5.31)$$

where U is a unitary 2×2 matrix. Unitarity is required so that the field has non-zero intensity everywhere. As in the $U(1)$ case a zero of the intensity can hide a discontinuity which would allow the phase winding to unravel.

The unitary transformation Eq. 5.31 consists of an overall phase multiplied by a special unitary matrix

$$U = e^{i\delta} \begin{pmatrix} \alpha & \beta \\ -\beta^* & \alpha^* \end{pmatrix} \quad (5.32)$$

with $|\alpha|^2 + |\beta|^2 = 1$. Here δ , α , and β will all depend on the point in k -space and possibly on the path taken to arrive there.

The matrix U changes the phase of the field and also the relative phase and amplitude of E_x and E_y , i.e. the polarisation. Again, this change can be incorporated in the definition of the states by choosing a local phase reference, but also a local polarisation basis. Then Eq. 5.31 can be interpreted as a local change of basis. This change from a global symmetry (the freedom to choose a polarisation basis) to a local one (the freedom to choose an independent basis at each point) is equivalent to the introduction of a gauge field [189]. Once again though this choice can only be made once at each point. If the phase and polarisation change when the system is taken through a closed cycle, then this change is gauge independent. The gauge freedom described by Eq. 5.31 is a $U(2)$ gauge.

A two level paraxial Hamiltonian will have two eigenvectors $E^{1,2}(\vec{p}, z)$. Recalling that z plays the role in the paraxial wave equation played by time in the Schrödinger equation, then the equivalent of an adiabatic transformation is a gradual change in \vec{p} along the beam axis. We can describe the evolution of the phase and polarisation in z by the action of a non-Abelian field with $U(2)$ symmetry, just as the spatially varying phase of a wave-function under an adiabatic transformation is equivalent to a magnetic potential.

The eigenvector at a point \vec{p} is related to the eigenvector at an infinitesimally distant point

$$\vec{E}^1(\vec{p}_0 + \delta\vec{p}) = (\mathbb{I} + iA(\vec{p}_0) \cdot \delta\vec{p}) \vec{E}^1(\vec{p}_0). \quad (5.33)$$

by the gauge field A , each component of which is now a matrix. The operator U which describes finite displacements is obtained by matrix exponentiation. However,

A is not completely defined by its action on a single vector, we also need to consider the other eigenvector at each point which is orthogonal:

$$\vec{E}^i \cdot \vec{E}^j = \delta_{ij}. \quad (5.34)$$

Propagation in a particular medium is characterised by the effect on both orthogonal polarisations at each point. Taking two such orthogonal basis vectors at each value of the momentum we find

$$i\vec{A}^{ij} = \overline{E^j} \cdot \nabla_k E^i. \quad (5.35)$$

This gives the matrix-valued Berry connection between the two fields at nearby points. Here the over-line refers to complex conjugation. The indices i and j refer to the first and second polarisation vectors, while the dot product is over the components of these vectors in some given basis. The vector nature of A comes from the vector ∇ which has a component for each dimension of \vec{k} . Hence \vec{A} is a vector of two by two matrices.

Looking back at the example of the homotopy Eq. 5.30, between a field with a vortex and one without, we can see why it is necessary to consider two orthogonal polarisations. While this homotopy removed a vortex from one polarisation, to maintain orthogonality at all times it would be necessary to also insert a vortex into the other polarisation. Hence when considering the two polarisations we see that we have not truly removed the winding, but merely transferred it from one polarisation to the other. The total number of windings is the same, We will make this more precise when we calculate the topological invariant associated with the non-Abelian Berry connection Eq. 5.35.

It is worth noting that just as the Abelian gauge field described in Eq. 5.7 couples the wavefunction to the electromagnetic field, non-Abelian gauge fields describe the coupling between wavefunctions and more complex forces, such as the weak and strong nuclear force. Hence the paraxial wave equation which has a Hamiltonian whose eigenvectors give a non-Abelian Berry connection 5.35 is analogous to a Schrödinger equation describing particles being acted on by such a higher order field. The nature of the force depends on the group of gauge symmetry, i.e. the group of all possible gauge transformations which leave the Schrödinger equation invariant. Beams with varying polarisation can thus act as a simple model for the coupling of matter to non-Abelian gauge fields.

5.3.1 Calculation of finite operator

By definition, a non-Abelian gauge field A is one which does not commute at different points. As A is matrix-valued (indeed we will see that it is in the Lie algebra \mathfrak{u}_2) we will have in general that

$$\left[A(\vec{k}), A(\vec{k}') \right] \neq 0. \quad (5.36)$$

The matrix exponential is defined through its Taylor series, which will mix terms with A at different points. It is therefore necessary to use the path-ordered exponentiation, which will keep track of the ordering of these factors,

$$U(\phi) = \mathcal{P} \left\{ \exp \left(i \int_0^\phi A_\varphi(\phi') d\phi' \right) \right\} \quad (5.37)$$

$$= \lim_{N \rightarrow \infty} e^{iA(\phi_N)\Delta t} \dots e^{iA(\phi_2)\Delta t} e^{iA(\phi_1)\Delta t}, \quad (5.38)$$

where $A_\varphi = \vec{A} \cdot d\vec{l}/d\phi$ gives the component of A along the path \hat{l} . The operator evolves the state along each infinitesimal part of the path in order, always moving along earlier parts before later ones.

Since the eigenstates are presumed normalised, we can show that A is Hermitian: the diagonal elements are real and the off-diagonal elements are related by complex conjugation.

$$\begin{aligned} \nabla(\bar{E}^i \cdot E^j) &= 0 = \bar{E}^i \cdot (\nabla E^j) + (\nabla \bar{E}^j) \cdot E^i \\ &= iA^{ji} - i\bar{A}^{ij} \\ &\Rightarrow \bar{A}^{ij} = A^{ji}. \end{aligned} \quad (5.39)$$

Hence A can be written as a linear combination of the identity and the Pauli matrices. We write

$$A^\mu(\phi) = a_0^\mu(\phi)\mathbb{I} + \vec{a}^\mu(\phi) \cdot \vec{\sigma}. \quad (5.40)$$

Note that $\vec{a}^\mu = \{a_i^\mu\}$ has a spinor index $i \in \{1, 2, 3\}$ and a vector index $\mu \in \{p_x, p_y\}$. Since the identity \mathbb{I} commutes with all the Pauli matrix, we can bring this contribution from each term to the front of (5.38) and separate them from the path ordered integral,

$$U(\phi) = \exp \left(i \int_0^\phi a_0(\phi') d\phi' \right) \mathcal{P} \left\{ \exp \left(i \int_0^\phi \vec{a}(\phi') \cdot \vec{\sigma} d\phi' \right) \right\}. \quad (5.41)$$

The first factor has the form of a global Berry phase acting on both polarisations while the second factor is a path ordered integral in $SU(2)$ accounting for an overall changing of the polarisation described by each band as we move along the path.

5.3.2 $U(2)$ topological invariants

We now describe how to calculate the homotopic invariant associated with the transformation given in Eq. 5.41. This operator $U(\phi)$, for a given value of ϕ , is a unitary matrix of dimension two. However, considered as a function of ϕ , it is a closed loop in the topological space of all two-dimensional unitary matrices, $U(2)$. Hence we can consider the homotopy class of such loops. Because $U(2) \sim U(1) \times SU(2)$

are isomorphic as groups, as can be seen from the general form of a unitary matrix Eq. 5.32, the homotopy group

$$\pi(U(2)) = \pi(U(1)) \times \pi(SU(2)) \quad (5.42)$$

is given by the product of the homotopy groups [190]. Since $SU(2)$ has a trivial homotopy group (all loops are contractible), the homotopy group of $U(2)$ is the same as the homotopy group of $U(1)$, which is the set of integers.

Although the homotopy groups are the same, we have seen already that the way in which loops are classified in this group is different. We seek a formula which will tell us the $U(2)$ integer invariant for a pair of orthogonally polarised bands. The winding number which should be associated to a loop in $U(2)$ is in fact the $U(1)$ winding number of the determinant of the $U(2)$ matrix along the path.

To see this consider two continuous loops in $U(2)$, i.e. continuous $U(2)$ -valued functions

$$M, N : [0, 2\pi] \rightarrow U(2) \quad (5.43)$$

with $M(0) = N(0) = M(2\pi) = N(2\pi) = \mathbb{I}$. Let the winding number of the determinant of a matrix be denoted, e.g.,

$$\gamma_N = \frac{1}{2\pi} \int_0^{2\pi} d\phi' \det(N(\phi'))^* \partial_{\phi'} \det(N(\phi')). \quad (5.44)$$

We claim that $M \sim N$ is a homotopy if and only if $\gamma_N = \gamma_M$.

First assume that $N \sim M$. Then by the definition of homotopy there exists a continuous function $G(\phi, t)$ such that $G(\phi, 0) = N(\phi)$, $G(\phi, 1) = M(\phi)$, and $G(0, t) = G(2\pi, t) = \mathbb{I}$ for all t . The first two properties ensure that $\gamma_G(0) = \gamma_N$ and $\gamma_G(1) = \gamma_M$. The third ensures that $\gamma_G(t)$ is always an integer. Since $\gamma_G(t)$ is a continuous function to the integers it must be constant.

Next assume $\gamma_M = \gamma_N$. The paths $N(\phi)$ and $M(\phi)$ are clearly homotopic to their diagonals at each point $N \sim D_N$, $M \sim D_M$. Note that they need not be simultaneously diagonalisable, we can diagonalise them independently at each value of ϕ , since any unitary matrix is diagonalisable. Since the eigenvectors are always orthogonal, there is no ambiguity in smoothly labelling each eigenvalue. Furthermore the determinant is invariant under this change of basis so $\gamma_{D_N} = \gamma_{D_M}$. Since the matrix is unitary the eigenvalues are of the form $\exp(if(\phi)) \in U(1)$ which are each homotopic to $\exp(im\phi)$ for some integer m . Two diagonal unitary matrices with linear phase can be related by the explicit homotopy

$$G(\phi, t) = \begin{pmatrix} e^{i\phi((1-t)m_1+tn_1)} & 0 \\ 0 & e^{i\phi((1-t)m_2+tn_2)} \end{pmatrix} \quad (5.45)$$

assuming that $n_1 + n_2 = m_1 + m_2$. (To see that this is necessary consider the determinant

$$\det(G(2\pi, t)) = \exp\{i2\pi(m_1 + m_2 + t((n_1 + n_2) - (m_1 + m_2)))\} \quad (5.46)$$

which should be equal to one for all t because $\det(G(0)) = 1$ and we require the loop to remain closed.) Hence we conclude $M \sim N$ if and only if $\gamma_N = \gamma_M$, i.e. the winding numbers of their determinants are equal.

Taking the determinant of the infinitesimal expansion Eq. 5.38 and using the matrix identities

$$\det(AB) = \det(A) \det(B), \quad (5.47)$$

$$\det(\exp(L)) = \exp(\text{Tr}(L)), \quad (5.48)$$

we find that

$$\det(U(\phi)) = \det\left(\lim_{N \rightarrow \infty} e^{iA(\phi_N)\Delta t} \dots e^{iA(\phi_2)\Delta t} e^{iA(\phi_1)\Delta t}\right) \quad (5.49)$$

$$= \lim_{N \rightarrow \infty} \det(e^{iA(\phi_N)\Delta t}) \dots \det(e^{iA(\phi_1)\Delta t}) \quad (5.50)$$

$$= \lim_{N \rightarrow \infty} e^{i\text{Tr}(A(\phi_N))\Delta t} \dots e^{i\text{Tr}(A(\phi_1))\Delta t}. \quad (5.51)$$

The trace of the gauge field, A , is simply a complex number, so the path ordering is trivial and can be neglected, giving

$$\det(U(\phi)) = \exp\left\{i \int_0^\phi \text{Tr}(A(\phi')) d\phi'\right\}. \quad (5.52)$$

Since the Pauli matrices are trace-less the winding number is

$$\gamma = \frac{1}{2\pi} \int_0^{2\pi} \text{Tr}(a_0(\phi')\mathbb{I}) d\phi' = \frac{1}{\pi} \int_0^{2\pi} a_0(\phi') d\phi'. \quad (5.53)$$

More generally, without parameterising the path, the gauge invariant winding number around a general closed loop c is

$$\gamma = \frac{1}{\pi} \oint_c a_0 \cdot d\vec{l}. \quad (5.54)$$

This integral characterises the winding of the phase and polarisation around a loop in phase space. When the path c is the boundary of the Brillouin zone, this integer characterises the bands describing two orthogonal polarisations. Equation 5.54, along with Eq. 5.35, gives a simple formula to calculate the homotopy invariant associated with the change in both phase and polarisation around a loop in momentum space for propagating paraxial beams of light in a medium with polarisation coupling. This is the sum of the phase winding numbers in the two orthogonal polarisations. Although the twisting of the polarisation does not explicitly appear in the $U(2)$ invariant Eq. 5.53 it allows phase windings to move between the two polarisations meaning that the naive $U(1)$ number for either mode is not invariant. Note that if the Hamiltonian H had been simultaneously diagonalisable at each point, we could have carried through the same analysis, with all matrices being diagonal. There would be no way to move vortices between the eigenvalues of a_0 , and the trace in Eq. 5.54 would be the sum of two integers which were each independently invariant, i.e. the $U(11)$ Chern numbers of each scalar field.

5.4 Non-Abelian gauge field of a chiral biaxial material

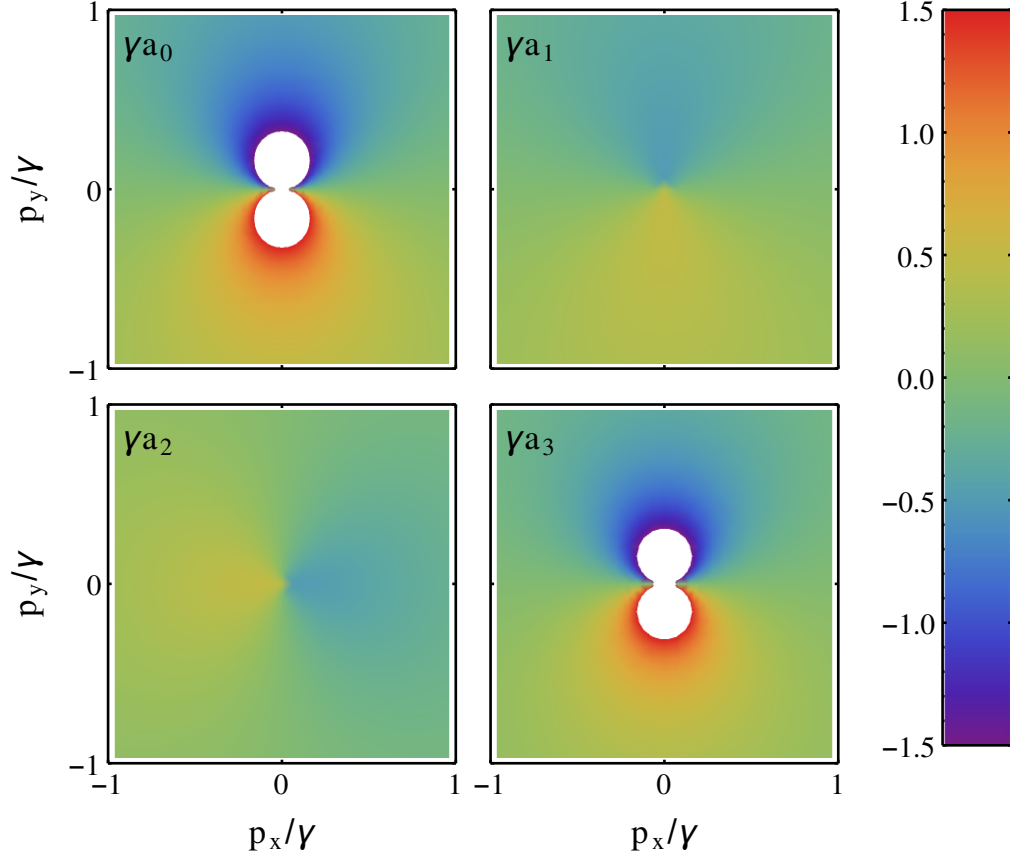


Figure 5.6: The four matrix coefficients of the x component of the non-Abelian gauge potential A , describing the eigenmodes of a chiral biaxial medium. The panels correspond to the coefficients of the potential expressed as a linear combination of the identity and the Pauli matrices, i.e. $\vec{A} = a_0 \mathbb{I} + \vec{a} \cdot \vec{\sigma}$. These are density plots of γA_x as a function of \vec{p}/γ . In this gauge (see text) the y component is equivalent but rotated by 90° .

As an explicit realisation of the general physics discussed above, we return to a chiral biaxial medium, and compute both the gauge field and the invariant. Using Eq. 5.35 and the eigenmodes Eq. 5.26 the artificial gauge potential, in polar coordinates (p, ϕ) , is

$$A_x = -\frac{\sin(\phi)}{2p} \mathbb{I} - \frac{\sin(\phi)}{2\sqrt{p^2 + \gamma^2}} \sigma_1 - \frac{\cos(\phi)\gamma}{2(p^2 + \gamma^2)} \sigma_2 - \frac{\sin(\phi)\gamma}{2p\sqrt{p^2 + \gamma^2}} \sigma_3 \quad (5.55)$$

$$A_y = \frac{\cos(\phi)}{2p} \mathbb{I} + \frac{\cos(\phi)}{2\sqrt{p^2 + \gamma^2}} \sigma_1 - \frac{\sin(\phi)\gamma}{2(p^2 + \gamma^2)} \sigma_2 + \frac{\cos(\phi)\gamma}{2p\sqrt{p^2 + \gamma^2}} \sigma_3 \quad (5.56)$$

The potential is shown in Fig. 5.6. Note that as ϕ and p are varied, the potential and field will have different coefficients of the Pauli matrices. Hence the fields at any two points will generally not commute, and we have a true non-Abelian field. In the chosen gauge the potential exhibits dipole like patterns in each component. The non-trivial p -dependence of all four components is a consequence of the fact that the phase, the ellipticity, and the angle of polarisation are all varying. However, the potential A is gauge dependent and could look quite different in a different gauge. Hence the details need not be over-analysed.

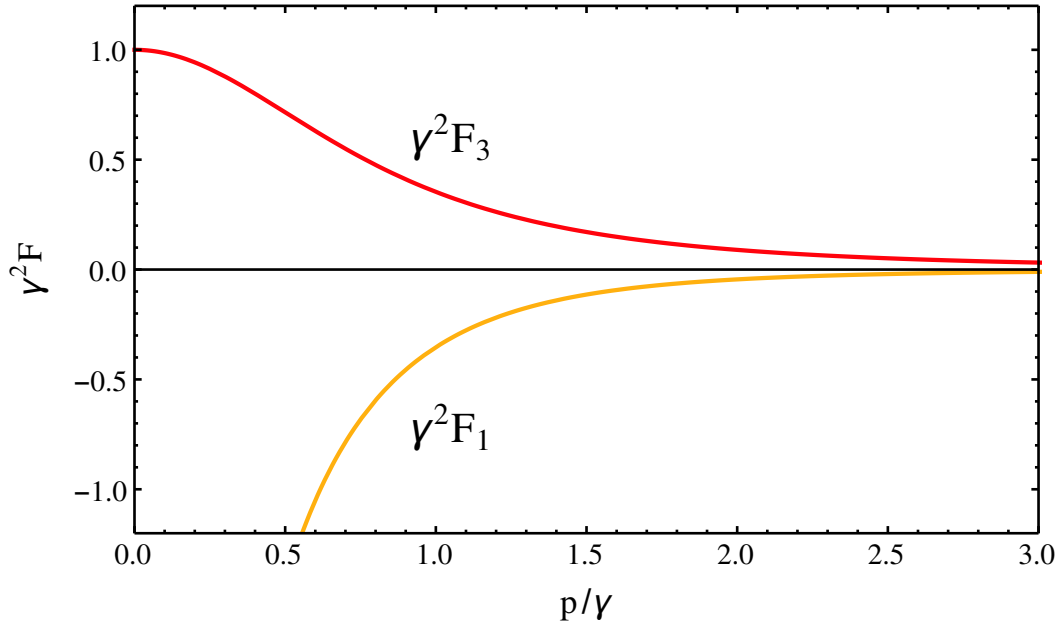


Figure 5.7: The two components of the non-Abelian field strength $F = F_1\sigma_1 + F_3\sigma_3$ for a chiral biaxial material are shown as cross sections at constant angle. The two components are circularly symmetric around the origin. Note we plot $\gamma^2 F$ as a function of p/γ . The x component is negative infinite at the origin while the z component is finite everywhere. Both components approach zero for $p \gg \gamma$.

The resulting field is calculated from a non-Abelian potential

$$F = \partial_{p_x} A_y - \partial_{p_y} A_x - i[A_x, A_y]. \quad (5.57)$$

Note the extra term $-i[A_x, A_y]$ in the calculation of the field from a non-Abelian potential, which is not present for an Abelian field. This term must be present to construct a gauge invariant Lagrangian for a non-Abelian field [189], and is only absent from an Abelian theory because it is always zero.

In the case of the chiral biaxial material we find that the resulting field is

$$F_z = -\frac{\gamma^2}{p(p^2 + \gamma^2)^{3/2}}\sigma_1 + \frac{\gamma}{(p^2 + \gamma^2)^{3/2}}\sigma_3. \quad (5.58)$$

This is plotted in Fig. 5.7. The field has two components, proportional to σ_1 and σ_3 respectively. As we can see it is confined to a region of order γ around the origin. Both components are positive and fall off with increasing distance. These components are gauge invariant, and represent the strength of artificial non-Abelian gauge field experienced by rays of light with given transverse momentum. The component proportional to σ_1 is infinite at the origin, as the fields there are circularly polarised and the angle of polarisation is not well-defined. The term proportional to σ_3 is finite everywhere.

The topology of the potential Eq. 5.55 can be understood by considering a circular path around the origin at large p , compared to γ . Taking the limit gives

$$\lim_{p/\gamma \rightarrow \infty} \vec{A} \cdot d\vec{p} = \left(\frac{1}{2}\mathbb{I} + \frac{1}{2}\sigma_1 \right) d\phi \quad (5.59)$$

with $d\vec{p} = p d\hat{\phi}$. As we move along this circle the phase of each polarisation increases at a rate of π per revolution, as shown by the $\mathbb{I}/2$ term. However, the polarisation is also rotating at the same rate, as shown by the $\sigma_1/2$ term. This explains the half-integer $U(1)$ Chern number which only accounts for the increasing phase. However, we can now calculate the $U(2)$ Chern number along a similar loop. Eq. 5.55 gives $a_0 = (\sin(\phi)/2p, -\cos(\phi)/2p)^T \mathbb{I}$. Thus $\vec{a}_0 \cdot d\vec{p} = \mathbb{I}/2$ giving

$$\gamma = \frac{1}{2\pi} \int_0^{2\pi} \text{Tr} \left\{ \frac{1}{2}\mathbb{I} \right\} d\phi' = 1. \quad (5.60)$$

The topological invariant associated with the simultaneous evolution of both polarisations is an integer. The half-windings in the phase of both eigenmodes add rather than cancelling meaning this is a topologically non-trivial state. The example of a chiral biaxial material therefore is a non-trivial material which may lead to designs with topologically robust edge states when it shares an interface with a trivial material such as the vacuum.

5.5 Conclusions

In conclusion, we have shown that the evolution of a paraxial beam of light along the beam axis in a general medium is equivalent to the evolution in time of a particle in two dimensions in the presence of a non-Abelian $U(2)$ gauge field. In the absence of polarisation mixing this gauge group is equivalent to a $U(1)$ magnetic vector potential acting on each polarisation. However, in the presence of disorder, or in a material which allows the polarisation to change as the beam propagates, the winding number associated with a single polarisation is not an integer invariant. Instead there is an integer associated with the equivalent non-Abelian field which describes the propagation of both polarisations.

It is interesting to note that this $U(2)$ gauge potential can be split into a $U(1)$ term, corresponding to overall phase, and an $SU(2)$ term corresponding to polarisation mixing. This is analogous to the splitting of the electroweak force into an electromagnetic $U(1)$ gauge field and the weak nuclear $SU(2)$ gauge field. Photonic systems designed to control both the phase and polarisation of propagating light could therefore simulate the presence of a combined electroweak force. More generally this gives a simple and accessible way to construct non-Abelian artificial gauge fields which are of considerable present interest [191, 192, 180].

The results of this chapter can be directly compared to our results on angular momentum in chapters 2 and 3. In both cases we have shown that the phase of an electric field can change by a multiple of π around a closed loop as long as the polarisation rotates by a similar amount. We have described this effect in two different ways, concentrating on the quantities of interest in both fields; optical angular momentum for vortex beams in real space, and topological invariants and homotopy classes for vortices in reciprocal space. The conclusion that the calculation of a half-integer Chern number is incorrect may seem at odds with the claim of half-integer generalised angular momentum. A physical beam with a particular polarisation and phase structure can indeed carry a half-integer angular momentum, while its orthogonal partner, which would also have half-integer generalised angular momentum, need not be present in the experiment. However, when we consider the class of paraxial Hamiltonians which act on both spin components in a way which is time-reversal invariant, we see that we cannot separate one polarisation from the other. However, there is a winding number of the $U(2)$ gauge field which includes both polarisations and is an integer.

The recent appearance of many papers which calculate topological invariants for time-reversal invariant photonic systems, using artificial gauge fields, chirality etc. are largely based on a formula for the Chern number of a scalar field. Using the results of this chapter, the full invariant in the presence of polarisation coupling can be calculated simply. Future work exploring specific realisations of this physics in a periodic lattice, and the consequences for edge states, is currently planned and will provide further insight into the nature of this invariant.

Chapter 6

Concluding remarks

In this thesis we have discussed three different subjects, linked through the recurring themes of topology and inhomogeneous polarisation. Here we provide a brief summary of the work, set it in the context of other work in the field, and suggest some possible future directions.

We have explored the possible forms of total angular momentum of a beam of light whose polarisation and phase are both allowed to vary in space. Using the paraxial approximation to describe the two-dimensional transverse field led us to consider a general form for the angular momentum, which is a linear combination $L + \gamma S$ of the spin and orbital components. This angular momentum is the generator of a rotation of the image and the polarisation by a fixed ratio. The generalised angular momentum has a complete set of continuous and single-valued eigenmodes when γ is either integer, or half-integer. When γ is half-integer, the eigenmodes have a half-integer winding in their phase around the beam which is compensated by a half-integer rotation in the angle of the polarisation ellipse. We have constructed a second quantised theory of this angular momentum and used it to calculate the statistics of the angular momentum current for a variety of states, providing an experimental probe of quantisation. For integer γ , the spectrum of angular momentum is an integer multiple of \hbar , while for half-integer γ the spectrum is a half-integer multiple of \hbar . The restriction to the two-dimensional transverse field thus leads to an unexpected, half-integer angular momentum for photons.

To measure this fractional angular momentum we have built an interferometer which rotates the image and the polarisation of the beam by different amounts, leading to constructive or destructive interference for different eigenmodes at the output. The angular momentum current is therefore the sum of the photon current

at each output weighted by the angular momentum per photon of that mode. We have measured the average angular momentum current per photon for the cases of spin, orbital, and generalised angular momentum, and shown that for $L + S/2$, this is indeed an average of $\hbar/2$ per photon. Furthermore we have measured a reduction in the shot noise for a coherent state which shows that the quantum of generalised angular momentum carried by individual photons is indeed a half-integer (in units of \hbar).

We have explored the creation of beams with inhomogeneous polarisation by conical refraction in a hyperbolic metamaterial. These materials have one principal dielectric constant which is negative, resulting from sub-wavelength layering of metal and dielectric constituents. We have extended the theory to the general case where the two remaining dielectric constants need not be equal. We have fully described the surfaces which give the refractive indices for the two orthogonal polarisations for any direction of propagation. These surfaces intersect linearly at four distinct points. We have derived both a geometrical optics and a full diffraction description of light propagating close to these intersection points. This theory includes absorption, which is unavoidable due to the metallic elements. We have also considered some possible implementations of such a material in the range where the effective theory considered here is applicable.

Finally, we have examined the topological numbers associated with scalar fields in periodic structures, and shown that this classification is not suitable to describe vector fields where the polarisation can change smoothly. We have shown that a non-Abelian artificial gauge field is necessary to describe the $U(2)$ group of possible symmetries of a paraxial field, rather than the $U(1)$ phase of a scalar field. This non-Abelian field has an invariant associated with it which is an integer, just like the naive $U(1)$ Chern number which describes bandstructures of scalar fields. However, the Chern number for a single polarisation is not invariant if polarisation coupling allows windings to move smoothly from one polarisation to the other. The line integral of the trace of the non-Abelian potential around the Brillouin zone gives the appropriate invariant, specifically the integer corresponding to the first homotopy classification of paths in $U(2)$ corresponding to paths in k -space. We have illustrated these findings with the example of the bandstructure of a chiral biaxial material, showing that this bandstructure is described by a non-Abelian field, with an invariant $C = 1$.

Our work extends the study of optical angular momentum to true fractional angular momentum, at both a classical and a quantum level. Beams where the phase varies by a fractional multiple of 2π around the beam have previously been studied [101, 18, 102]. If this phase is carried by a scalar beam, then the remainder of the phase change must happen at one or more discontinuities, destroying rotational

symmetry. The beams we consider are continuous, single valued functions of the azimuthal angle, and the fractional angular momentum is preserved under propagation. Previous studies of fractional angular momentum in two dimensions have focused on electronic systems [34, 193], in particular the fractional quantum Hall effect [161]. By using the shot noise in a coherent beam to measure the quantum of angular momentum, we have opened the way for the study of fractional quantisation in beams of light. Measuring the noise in the angular momentum current also measures the quantum of traditional quantities like the spin and orbital angular momentum, giving a method to measure these quantities at the quantum level without the use of single-photon detectors [104, 194].

Our work on topology implies that invariants calculated for scalar fields will not provide robustness to disorder when polarisation coupling is considered. Since generic disorder will mix polarisations, it is necessary to consider the full $U(2)$ invariant to design devices which are truly robust. The invariant we have found gives a means to extend the classification of paraxial bandstructures to the case where the polarisation can vary in k -space in a non-trivial way. Furthermore the associated gauge fields give a simple and accessible model of non-Abelian gauge fields which are currently of significant interest [191, 192, 180].

Future work on generalised angular momentum could concentrate on multi-photon effects. Our interferometer acts on single photons in a linear way, with each photon being measured independently. Although our shot noise measurement shows that each photon carries a half-integer multiple of \hbar of generalised angular momentum, the question remains if this fermionisation has any effect on the statistics. This question could be explored through calculations and measurements of two-photon or multi-photon correlations between the outputs of the interferometer. Of particular interest is the Hong-Ou Mandel effect [195], whereby two identical photons incident on different inputs of a 50/50 beamsplitter will always emerge from the same output. For fermions the effect is reversed and both particles will emerge from different outputs. An interesting question is whether we could see the fermionic nature of the generalised angular momentum states, perhaps by replacing the beamsplitter with an element which acts on the image and the polarisation, such as our generalised angular momentum interferometer.

It would also be interesting to examine more fundamental quantum mechanical properties of photons in a generalised angular momentum state. For example work on orbital angular momentum has shown that the quantum number l can be entangled [41, 196], and that there is an action-angle uncertainty principle which governs its measurement [197, 49]. Similar questions can be explored for a generalised angular momentum state. Is there a corresponding uncertainty principle which limits how accurately one can measure j_γ ? Can we have entanglement between photons

with different j_γ , or entanglement between the spin and orbital angular momentum in pairs of photons which are not eigenstates of spin and orbital angular momentum but only of generalised angular momentum? In particular, can we devise novel tests of Bell-like inequalities incorporating correlations of spin, orbital and generalised angular momentum? All these questions could provide the basis of ongoing work.

The theory of conical refraction in a biaxial hyperbolic metamaterial presented here is reasonably self contained. Additional calculations to fully describe the three dimensional iso-frequency surface in the presence of absorption, and especially in the case of anisotropic absorption, would be of interest. Additionally, the full effect of chirality could be explored, in particular the existence and position of polarisation singularities which should remain even when the refractive-index degeneracies are lifted. Finally, it would be interesting to calculate the diffraction of a beam on which propagates along the direction of the conical intersection, beyond the focal image plane.

However, the main challenge is to manufacture an experimental sample which is described by the effective medium theory used here with sufficient biaxiality to observe conical refraction. As we have discussed, there is an extended range of parameters for which this is possible. Nevertheless making a sample of sufficient size, either by self-assembly or by nano-fabrication, will not be trivial.

Future work on topological invariants of periodic systems could focus on designing particular systems which have non-trivial polarisation winding, with edge states which are protected by the full $U(2)$ invariant. The chiral biaxial material examined in this thesis may act as a starting point for such a design. An interesting theoretical extension would be to consider polariton systems, rather than simply linear photonics. Polaritons, formed from coupling semiconductor excitons to light in a cavity, can interact [198]. The effect of such interactions on the topological classification may open the way to a fractional quantum Hall effect of light [199, 200]. Since polaritons are also spin one particles, the considerations of varying polarisation are equally valid in these systems. The end goal of this path would be to have a full library of possible terms including spin-orbit, interactions, etc. which could arise in a photonic or polariton system, and to understand the effect of each of them on the topology of the bandstructure.

Bibliography

- [1] J. E. Avron, D. Osadchy, and R. Seiler. A Topological Look at the Quantum Hall Effect. *Physics Today*, 56(8):38–42, August 2003.
- [2] K. v. Klitzing, G. Dorda, and M. Pepper. New method for high-accuracy determination of the fine-structure constant based on quantized Hall resistance. *Phys. Rev. Lett.*, 45:494–497, Aug 1980.
- [3] M. Z. Hasan and C. L. Kane. Colloquium: Topological insulators. *Rev. Mod. Phys.*, 82:3045–3067, Nov 2010.
- [4] Hsin Lin, L. Andrew Wray, Yuqi Xia, Suyang Xu, Shuang Jia, Robert J. Cava, Arun Bansil, and M. Zahid Hasan. Half-heusler ternary compounds as new multifunctional experimental platforms for topological quantum phenomena. *Nat Mater*, 9(7):546–549, July 2010.
- [5] A. R. Mellnik, J. S. Lee, A. Richardella, J. L. Grab, P. J. Mintun, M. H. Fischer, A. Vaezi, A. Manchon, E.-A. Kim, N. Samarth, and D. C. Ralph. Spin-transfer torque generated by a topological insulator. *Nature*, 511(7510):449–451, July 2014.
- [6] M.S. Soskin and M.V. Vasnetsov. Chapter 4 Singular optics. *Progress in Optics*, 42:219 – 276, 2001.
- [7] Mark R. Dennis, Kevin O’Holleran, and Miles J. Padgett. Chapter 5 Singular optics: Optical vortices and polarization singularities. *Progress in Optics*, 53:293 – 363, 2009.
- [8] D. R. Smith and D. Schurig. Electromagnetic wave propagation in media with indefinite permittivity and permeability tensors. *Phys. Rev. Lett.*, 90:077405, Feb 2003.

- [9] Alexander Poddubny, Ivan Iorsh, Pavel Belov, and Yuri Kivshar. Hyperbolic metamaterials. *Nat Photon*, 7(12):948–957, December 2013.
- [10] Barry Simon. Holonomy, the quantum adiabatic theorem, and Berry’s phase. *Phys. Rev. Lett.*, 51:2167–2170, Dec 1983.
- [11] M. Nakahara. *Geometry, Topology, and Physics*. Graduate Student Series in Physics. IOP, 2003.
- [12] J. F. Nye and M. V. Berry. Dislocations in wave trains. *Proceedings of the Royal Society of London A: Mathematical, Physical and Engineering Sciences*, 336(1605):165–190, 1974.
- [13] M. Harris, C.A. Hill, and J.M. Vaughan. Optical helices and spiral interference fringes. *Optics Communications*, 106(4-6):161 – 166, 1994.
- [14] M. S. Soskin, V. N. Gorshkov, M. V. Vasnetsov, J. T. Malos, and N. R. Heckenberg. Topological charge and angular momentum of light beams carrying optical vortices. *Phys. Rev. A*, 56:4064–4075, Nov 1997.
- [15] Gabriel Molina-Terriza, Jaume Recolons, Juan P. Torres, Lluís Torner, and Ewan M. Wright. Observation of the dynamical inversion of the topological charge of an optical vortex. *Phys. Rev. Lett.*, 87:023902, Jun 2001.
- [16] Mahito Kohmoto. Topological invariant and the quantization of the Hall conductance. *Annals of Physics*, 160(2):343 – 354, 1985.
- [17] L. Allen, M. W. Beijersbergen, R. J. C. Spreeuw, and J. P. Woerdman. Orbital angular momentum of light and the transformation of Laguerre-Gaussian laser modes. *Phys. Rev. A*, 45:8185–8189, Jun 1992.
- [18] Jonathan Leach, Eric Yao, and Miles J Padgett. Observation of the vortex structure of a non-integer vortex beam. *New Journal of Physics*, 6(1):71, 2004.
- [19] J. F. Nye, J. V. Hajnal, and J. H. Hannay. Phase saddles and dislocations in two-dimensional waves such as the tides. *Proceedings of the Royal Society of London A: Mathematical, Physical and Engineering Sciences*, 417(1852):7–20, 1988.
- [20] Isaac Freund. Poincaré vortices. *Opt. Lett.*, 26(24):1996–1998, Dec 2001.
- [21] Jonathan Leach, Mark R. Dennis, Johannes Courtial, and Miles J. Padgett. Laser beams: Knotted threads of darkness. *Nature*, 432(7014):165–165, November 2004.

- [22] M V Berry and M R Dennis. Knotting and unknotting of phase singularities: Helmholtz waves, paraxial waves and waves in 2+1 spacetime. *Journal of Physics A: Mathematical and General*, 34(42):8877, 2001.
- [23] M. V. Berry. Quantal phase factors accompanying adiabatic changes. *Proceedings of the Royal Society of London. A. Mathematical and Physical Sciences*, 392(1802):45–57, 1984.
- [24] F. Wilczek and A. Shapere. *Geometric Phases in Physics*. Advanced series in mathematical physics. World Scientific, 1989.
- [25] D. J. Thouless, M. Kohmoto, M. P. Nightingale, and M. den Nijs. Quantized Hall conductance in a two-dimensional periodic potential. *Phys. Rev. Lett.*, 49:405–408, Aug 1982.
- [26] Li-Gang Wang, Zhi-Guo Wang, Jun-Xiang Zhang, and Shi-Yao Zhu. Realization of Dirac point with double cones in optics. *Opt. Lett.*, 34(10):1510–1512, May 2009.
- [27] J. Dieudonné. *A History of Algebraic and Differential Topology, 1900 - 1960*. Modern Birkhäuser Classics. Birkhäuser Boston, 2009.
- [28] John H. Davies. *The Physics of Low-dimensional Semiconductors: An Introduction*. Cambridge University Press, 1998.
- [29] J. L. Morán-López. *Physics of Low Dimensional Systems*. Focus on biotechnology. Springer, 2001.
- [30] H. Georgi. *Lie Algebras in Particle Physics: From Isospin to Unified Theories*. Frontiers in Physics Series. Westview Press, 1999.
- [31] A. P. French and E. F. Taylor. *An Introduction to Quantum Physics*. M.I.T. introductory physics series. Taylor & Francis, 1979.
- [32] Y. Aharonov and D. Bohm. Significance of electromagnetic potentials in the quantum theory. *Phys. Rev.*, 115:485–491, Aug 1959.
- [33] Frank Wilczek. Quantum mechanics of fractional-spin particles. *Phys. Rev. Lett.*, 49:957–959, Oct 1982.
- [34] Frank Wilczek. Magnetic flux, angular momentum, and statistics. *Phys. Rev. Lett.*, 48:1144–1146, Apr 1982.
- [35] Gregory W. Moore and N. Read. Nonabelions in the fractional quantum Hall effect. *Nucl.Phys.*, B360:362–396, 1991.

- [36] R. B. Laughlin. Anomalous quantum Hall effect: An incompressible quantum fluid with fractionally charged excitations. *Phys. Rev. Lett.*, 50:1395–1398, May 1983.
- [37] Andrew M. Essin and Victor Gurarie. Bulk-boundary correspondence of topological insulators from their respective Green’s functions. *Phys. Rev. B*, 84:125132, Sep 2011.
- [38] Ling Lu, John D. Joannopoulos, and Marin Soljacic. Topological photonics. *Nat Photon*, 8(11):821–829, November 2014.
- [39] B. I. Halperin. Quantized Hall conductance, current-carrying edge states, and the existence of extended states in a two-dimensional disordered potential. *Phys. Rev. B*, 25:2185–2190, Feb 1982.
- [40] S.J. van Enk and G. Nienhuis. Eigenfunction description of laser beams and orbital angular momentum of light. *Optics Communications*, 94(1-3):147 – 158, 1992.
- [41] Alois Mair, Alipasha Vaziri, Gregor Weihs, and Anton Zeilinger. Entanglement of the orbital angular momentum states of photons. *Nature*, 412(6844):313–316, July 2001.
- [42] Stephen M Barnett. Optical angular-momentum flux. *Journal of Optics B: Quantum and Semiclassical Optics*, 4(2):S7, 2002.
- [43] H. He, M. E. J. Friese, N. R. Heckenberg, and H. Rubinsztein-Dunlop. Direct observation of transfer of angular momentum to absorptive particles from a laser beam with a phase singularity. *Phys. Rev. Lett.*, 75:826–829, Jul 1995.
- [44] N. B. Simpson, K. Dholakia, L. Allen, and M. J. Padgett. Mechanical equivalence of spin and orbital angular momentum of light: An optical spanner. *Opt. Lett.*, 22(1):52–54, Jan 1997.
- [45] B. Thidé, H. Then, J. Sjöholm, K. Palmer, J. Bergman, T. D. Carozzi, Ya. N. Istomin, N. H. Ibragimov, and R. Khamitova. Utilization of photon orbital angular momentum in the low-frequency radio domain. *Phys. Rev. Lett.*, 99:087701, 2007.
- [46] Yan Yan, Guodong Xie, Martin P. J. Lavery, Hao Huang, Nisar Ahmed, Changjing Bao, Yongxiong Ren, Yinwen Cao, Long Li, Zhe Zhao, Andreas F. Molisch, Moshe Tur, Miles J. Padgett, and Alan E. Willner. High-capacity millimetre-wave communications with orbital angular momentum multiplexing. *Nat Commun*, 5:4876, September 2014.

- [47] Jonathan Leach, Barry Jack, Jacqui Romero, Anand K. Jha, Alison M. Yao, Sonja Franke-Arnold, David G. Ireland, Robert W. Boyd, Stephen M. Barnett, and Miles J. Padgett. Quantum correlations in optical angle-orbital angular momentum variables. *Science*, 329(5992):662–665, 2010.
- [48] Adetunmise C. Dada, Jonathan Leach, Gerald S. Buller, Miles J. Padgett, and Erika Andersson. Experimental high-dimensional two-photon entanglement and violations of generalized Bell inequalities. *Nat Phys*, 7(9):677–680, September 2011.
- [49] B Jack, P Aursand, S Franke-Arnold, D G Ireland, J Leach, S M Barnett, and M J Padgett. Demonstration of the angular uncertainty principle for single photons. *Journal of Optics*, 13(6):064017, 2011.
- [50] Monika A. M. Marte and Stig Stenholm. Paraxial light and atom optics: The optical schrödinger equation and beyond. *Phys. Rev. A*, 56:2940–2953, Oct 1997.
- [51] S. Raghu and F. D. M. Haldane. Analogs of quantum-Hall-effect edge states in photonic crystals. *Phys. Rev. A*, 78:033834, Sep 2008.
- [52] Tetsuyuki Ochiai and Masaru Onoda. Photonic analog of graphene model and its extension: Dirac cone, symmetry, and edge states. *Phys. Rev. B*, 80:155103, Oct 2009.
- [53] Alexander B. Khanikaev, S. Hossein Mousavi, Wang-Kong Tse, Mehdi Kargarian, Allan H. MacDonald, and Gennady Shvets. Photonic topological insulators. *Nat Mater*, 12(3):233–239, 2013.
- [54] Mikael C. Rechtsman, Julia M. Zeuner, Yonatan Plotnik, Yaakov Lumer, Daniel Podolsky, Felix Dreisow, Stefan Nolte, Mordechai Segev, and Alexander Szameit. Photonic Floquet topological insulators. *Nature*, 496(7444):196–200, 2013.
- [55] Wenlong Gao, Mark Lawrence, Biao Yang, Fu Liu, Fengzhou Fang, Benjamin Béri, Jensen Li, and Shuang Zhang. Topological photonic phase in chiral hyperbolic metamaterials. *Phys. Rev. Lett.*, 114:037402, Jan 2015.
- [56] Mikael C. Rechtsman, Yonatan Plotnik, Julia M. Zeuner, Daohong Song, Zhigang Chen, Alexander Szameit, and Mordechai Segev. Topological creation and destruction of edge states in photonic graphene. *Phys. Rev. Lett.*, 111:103901, Sep 2013.

- [57] Mohammad Hafezi, Eugene A. Demler, Mikhail D. Lukin, and Jacob M. Taylor. Robust optical delay lines with topological protection. *Nat Phys*, 7(11):907–912, Nov 2011.
- [58] Kejie Fang, Zongfu Yu, and Shanhui Fan. Realizing effective magnetic field for photons by controlling the phase of dynamic modulation. *Nat Photon*, 6(11):782–787, 2012.
- [59] Lawrence D. Tzuang, Kejie Fang, Paulo Nussenzeveig, Shanhui Fan, and Michal Lipson. Non-reciprocal phase shift induced by an effective magnetic flux for light. *Nat Photon*, 8(9):701–705, September 2014.
- [60] John C. Stover. *Optical Scattering: Measurement and Analysis*. SPIE, 2012.
- [61] M. Born, E. Wolf, and A.B. Bhatia. *Principles of Optics: Electromagnetic Theory of Propagation, Interference and Diffraction of Light*. Cambridge University Press, 1999.
- [62] J. F. Nye and J. V. Hajnal. The wave structure of monochromatic electromagnetic radiation. *Proceedings of the Royal Society of London A: Mathematical, Physical and Engineering Sciences*, 409(1836):21–36, 1987.
- [63] D. P. O’Dwyer, C. F. Phelan, K. E. Ballantine, Y. P. Rakovich, J. G. Lunney, and J. F. Donegan. Conical diffraction of linearly polarised light controls the angular position of a microscopic object. *Opt. Express*, 18(26):27319–27326, Dec 2010.
- [64] D. P. O’Dwyer, K. E. Ballantine, C. F. Phelan, J. G. Lunney, and J. F. Donegan. Optical trapping using cascade conical refraction of light. *Opt. Express*, 20(19):21119–21125, Sep 2012.
- [65] A. Turpin, V. Shvedov, C. Hnatovsky, Yu. V. Loiko, J. Mompart, and W. Krolikowski. Optical vault: A reconfigurable bottle beam based on conical refraction of light. *Opt. Express*, 21(22):26335–26340, Nov 2013.
- [66] Amin Abdolvand, Keith G. Wilcox, Todor K. Kalkandjiev, and Edik U. Rafailov. Conical refraction Nd:KGd(WO₄)₂ laser. *Opt. Express*, 18(3):2753–2759, Feb 2010.
- [67] R. T. Darcy, D. McCloskey, K. E. Ballantine, J. G. Lunney, P. R. Eastham, and J. F. Donegan. Conical diffraction intensity profiles generated using a top-hat input beam. *Opt. Express*, 22(9):11290–11300, May 2014.
- [68] Alex Turpin, Yury V Loiko, Todor K Kalkandjiev, and Jordi Mompart. Light propagation in biaxial crystals. *Journal of Optics*, 17(6):065603, 2015.

- [69] M V Berry, M R Jeffrey, and M Mansuripur. Orbital and spin angular momentum in conical diffraction. *Journal of Optics A: Pure and Applied Optics*, 7(11):685, 2005.
- [70] D. P. O'Dwyer, C. F. Phelan, Y. P. Rakovich, P. R. Eastham, J. G. Lunney, and J. F. Donegan. Generation of continuously tunable fractional optical orbital angular momentum using internal conical diffraction. *Opt. Express*, 18(16):16480–16485, Aug 2010.
- [71] M V Berry. Conical diffraction asymptotics: Fine structure of Poggendorff rings and axial spike. *Journal of Optics A: Pure and Applied Optics*, 6(4):289, 2004.
- [72] A. M. Belskii and A. P. Khapalyuk. Propagation of confined light beams along the beam axes (axes of single ray velocity) of biaxial crystals. *Optics and Spectroscopy*, 44:312–315, March 1978.
- [73] A. M. Belskii and A. P. Khapalyuk. Internal conical refraction of bounded light beams in biaxial crystals. *Optics and Spectroscopy*, 44:436–439, April 1978.
- [74] J. H. Poynting. The wave motion of a revolving shaft, and a suggestion as to the angular momentum in a beam of circularly polarised light. *Proceedings of the Royal Society of London A: Mathematical, Physical and Engineering Sciences*, 82(557):560–567, 1909.
- [75] C. Cohen-Tannoudji, J. Dupont-Roc, and G. Grynberg. *Photons and Atoms: Introduction to Quantum Electrodynamics*. Wiley professional paperback series. Wiley, 1997.
- [76] Miles Padgett and Richard Bowman. Tweezers with a twist. *Nat Photon*, 5(6):343–348, 2011. 10.1038/nphoton.2011.81.
- [77] Gabriel Molina-Terriza, Juan P. Torres, and Lluís Torner. Twisted photons. *Nature Physics*, 3(5):305, 2007.
- [78] Jonathan Leach, Johannes Courtial, Kenneth Skeldon, Stephen M. Barnett, Sonja Franke-Arnold, and Miles J. Padgett. Interferometric methods to measure orbital and spin, or the total angular momentum of a single photon. *Phys. Rev. Lett.*, 92:013601, Jan 2004.
- [79] Stephen M. Barnett and L. Allen. Orbital angular momentum and nonparaxial light beams. *Optics Communications*, 110:670 – 678, 1994.

- [80] R. de Picciotto, M. Reznikov, M. Heiblum, V. Umansky, G. Bunin, and D. Mahalu. Direct observation of a fractional charge. *Nature*, 389(6647):162–164, 1997. 10.1038/38241.
- [81] C. L. Kane and Matthew P. A. Fisher. Nonequilibrium noise and fractional charge in the quantum Hall effect. *Phys. Rev. Lett.*, 72:724–727, Jan 1994.
- [82] V. J. Goldman and B. Su. Resonant tunneling in the quantum Hall regime: Measurement of fractional charge. *Science*, 267(5200):1010–1012, 1995.
- [83] Iuliana P. Radu, J. B. Miller, C. M. Marcus, M. A. Kastner, L. N. Pfeiffer, and K. W. West. Quasi-particle properties from tunneling in the $\nu = 5/2$ fractional quantum Hall state. *Science*, 320(5878):899–902, 2008.
- [84] M. Dolev, M. Heiblum, V. Umansky, Ady Stern, and D. Mahalu. Observation of a quarter of an electron charge at the $\nu = 5/2$ quantum Hall state. *Nature*, 452(7189):829–834, 2008.
- [85] John D. Jackson. *Classical Electrodynamics Third Edition*. Wiley, third edition, August 1998.
- [86] E. F. Nichols and G. F. Hull. A preliminary communication on the pressure of heat and light radiation. *Phys. Rev. (Series I)*, 13:307–320, Nov 1901.
- [87] L. Allen, S.M. Barnett, and M.J. Padgett. *Optical angular momentum*. Institute of Physics Pub., 2003.
- [88] L. Mandel and E. Wolf. *Optical Coherence and Quantum Optics*. Cambridge University Press, 1995.
- [89] A. T. O’Neil, I. MacVicar, L. Allen, and M. J. Padgett. Intrinsic and extrinsic nature of the orbital angular momentum of a light beam. *Phys. Rev. Lett.*, 88:053601, Jan 2002.
- [90] Richard A. Beth. Mechanical detection and measurement of the angular momentum of light. *Phys. Rev.*, 50:115–125, Jul 1936.
- [91] L Allen and M.J Padgett. The Poynting vector in Laguerre-Gaussian beams and the interpretation of their angular momentum density. *Optics Communications*, 184(14):67 – 71, 2000.
- [92] Michael V. Berry. Paraxial beams of spinning light. In Marat S. Soskin, editor, *International Conference on Singular Optics*, volume 3487, pages 6–11. SPIE, 1998.

- [93] J. Garrison and R. Chiao. *Quantum Optics*. Oxford Graduate Texts. OUP Oxford, 2008.
- [94] A.E. Siegman. *Lasers*. University Science Books, 1986.
- [95] S. J. van Enk and G. Nienhuis. Spin and orbital angular momentum of photons. *EPL (Europhysics Letters)*, 25(7):497, 1994.
- [96] G. F. Calvo, A. Picón, and E. Bagan. Quantum field theory of photons with orbital angular momentum. *Physical Review A*, 73(1):013805, 2006.
- [97] W. Pauli. The connection between spin and statistics. *Phys. Rev.*, 58:716–722, Oct 1940.
- [98] Frank Wilczek. Magnetic flux, angular momentum, and statistics. *Phys. Rev. Lett.*, 48:1144–1146, Apr 1982.
- [99] C. A. Dartora, G. G. Cabrera, K. Z. Nobrega, V. F. Montagner, Marina H. K. Matielli, Fillipi Klos Rodrigues de Campos, and Horacio Tertuliano S. Filho. Lagrangian-Hamiltonian formulation of paraxial optics and applications: Study of gauge symmetries and the optical spin Hall effect. *Phys. Rev. A*, 83:012110, Jan 2011.
- [100] S. J. van Enk and G. Nienhuis. Spin and orbital angular momentum of photons. *EPL (Europhysics Letters)*, 25(7):497, 1994.
- [101] M V Berry. Optical vortices evolving from helicoidal integer and fractional phase steps. *Journal of Optics A: Pure and Applied Optics*, 6(2):259, 2004.
- [102] J. B. Götte, S. Franke-Arnold, R. Zambrini, and Stephen M. Barnett. Quantum formulation of fractional orbital angular momentum. *Journal of Modern Optics*, 54(12):1723–1738, 2007.
- [103] M. J. Padgett and J. Courtial. Poincaré-sphere equivalent for light beams containing orbital angular momentum. *Opt. Lett.*, 24(7):430–432, Apr 1999.
- [104] Jonathan Leach, Miles J. Padgett, Stephen M. Barnett, Sonja Franke-Arnold, and Johannes Courtial. Measuring the orbital angular momentum of a single photon. *Phys. Rev. Lett.*, 88:257901, Jun 2002.
- [105] L. Marrucci, C. Manzo, and D. Paparo. Optical spin-to-orbital angular momentum conversion in inhomogeneous anisotropic media. *Phys. Rev. Lett.*, 96:163905, Apr 2006.
- [106] Gerard Nienhuis. Doppler effect induced by rotating lenses. *Optics Communications*, 132(1-2):8 – 14, 1996.

- [107] R. Simon, H. J. Kimble, and E. C. G. Sudarshan. Evolving geometric phase and its dynamical manifestation as a frequency shift: An optical experiment. *Phys. Rev. Lett.*, 61:19–22, Jul 1988.
- [108] Bruce A. Garetz. Angular doppler effect. *J. Opt. Soc. Am.*, 71(5):609–611, May 1981.
- [109] L. Allen, M. Babiker, and W.L. Power. Azimuthal doppler shift in light beams with orbital angular momentum. *Optics Communications*, 112(3 -4):141 -144, 1994.
- [110] R. Loudon. *The quantum theory of light*. Oxford science publications. Clarendon Press, 1983.
- [111] U. Fano. Ionization yield of radiations. ii. the fluctuations of the number of ions. *Phys. Rev.*, 72:26–29, Jul 1947.
- [112] C. W. J. Beenakker and M. Patra. Photon shot noise. *Modern Physics Letters B*, 13(11):337–347, 1999.
- [113] K. Y. Bliokh, J. Dressel, and F. Nori. Conservation of the spin and orbital angular momenta in electromagnetism. *New Journal of Physics*, 16(9):093037, September 2014.
- [114] Robert P Cameron, Fiona C Speirits, Claire R Gilson, L Allen, and Stephen M Barnett. The azimuthal component of Poynting’s vector and the angular momentum of light. *Journal of Optics*, 17(12):125610, 2015.
- [115] A. Aiello and M. V. Berry. Note on the helicity decomposition of spin and orbital optical currents. *Journal of Optics*, 17(6):062001, June 2015.
- [116] S. Machida, Y. Yamamoto, and Y. Itaya. Observation of amplitude squeezing in a constant-current-driven semiconductor laser. *Phys. Rev. Lett.*, 58:1000–1003, Mar 1987.
- [117] Y. Yamamoto, S. Machida, and O. Nilsson. Amplitude squeezing in a pump-noise-suppressed laser oscillator. *Phys. Rev. A*, 34:4025–4042, Nov 1986.
- [118] D. P. O’Dwyer, C. F. Phelan, Y. P. Rakovich, P. R. Eastham, J. G. Lunney, and J. F. Donegan. The creation and annihilation of optical vortices using cascade conical diffraction. *Opt. Express*, 19(3):2580–2588, Jan 2011.
- [119] Ivan Moreno, Gonzalo Paez, and Marija Strojnik. Polarization transforming properties of dove prisms. *Optics Communications*, 220(4 -6):257 – 268, 2003.

- [120] Laurence William Nagel and Donald O Pederson. *SPICE: Simulation program with integrated circuit emphasis*. Electronics Research Laboratory, College of Engineering, University of California, 1973.
- [121] G. Heinzel, A. Rüdiger, and R. Schilling. Spectrum and spectral density estimation by the discrete Fourier transform (DFT), including a comprehensive list of window functions and some new flat-top windows. Technical report, Max-Planck-Institut für Gravitationsphysik Teilinstitut, Hannover, February 2002.
- [122] J.G. Proakis and D.G. Manolakis. *Digital Signal Processing: Principles, Algorithms, and Applications*. Prentice Hall international editions. Prentice Hall, 1996.
- [123] H.A. Bachor and T.C. Ralph. *A Guide to Experiments in Quantum Optics*. Physics textbook. Wiley, 2004.
- [124] D. R. Smith, J. B. Pendry, and M. C. K. Wiltshire. Metamaterials and negative refractive index. *Science*, 305(5685):788–792, 2004.
- [125] V. G. Veselago. The electrodynamics of substances with simultaneously negative values of ϵ and μ . *Physics-Uspekhi*, 10(4):509–514, 1968.
- [126] Mikhail Noginov, Mikhail Lapine, Viktor Podolskiy, and Yuri Kivshar. Focus issue: hyperbolic metamaterials. *Opt. Express*, 21(12):14895–14897, Jun 2013.
- [127] Karolina Korzeb, Marcin Gajc, and Dorota Anna Pawlak. Compendium of natural hyperbolic materials. *Opt. Express*, 23(20):25406–25424, Oct 2015.
- [128] G.W. Milton. *The Theory of Composites*. Cambridge Monographs on Applied and Computational Mathematics. Cambridge University Press, 2002.
- [129] C L Cortes, W Newman, S Molesky, and Z Jacob. Quantum nanophotonics using hyperbolic metamaterials. *Journal of Optics*, 14(6):063001, 2012.
- [130] J. B. Pendry. A chiral route to negative refraction. *Science*, 306(5700):1353–1355, 2004.
- [131] Lorenzo Ferrari, Dylan Lu, Dominic Lepage, and Zhaowei Liu. Enhanced spontaneous emission inside hyperbolic metamaterials. *Opt. Express*, 22(4):4301–4306, Feb 2014.
- [132] Zubin Jacob, Leonid V. Alekseyev, and Evgenii Narimanov. Optical hyperlens: Far-field imaging beyond the diffraction limit. *Opt. Express*, 14(18):8247–8256, Sep 2006.

- [133] Dylan Lu, Jimmy J. Kan, Eric E. Fullerton, and Zhaowei Liu. Enhancing spontaneous emission rates of molecules using nanopatterned multilayer hyperbolic metamaterials. *Nat Nano*, 9(1):48–53, January 2014.
- [134] J. B. Pendry. Negative refraction makes a perfect lens. *Phys. Rev. Lett.*, 85:3966–3969, Oct 2000.
- [135] Alessandro Salandrino and Nader Engheta. Far-field subdiffraction optical microscopy using metamaterial crystals: Theory and simulations. *Phys. Rev. B*, 74:075103, Aug 2006.
- [136] Justin Elser, Robyn Wangberg, Viktor A. Podolskiy, and Evgenii E. Narimanov. Nanowire metamaterials with extreme optical anisotropy. *Applied Physics Letters*, 89(26):261102, 2006.
- [137] Jingbo Sun, Jinwei Zeng, and Natalia M. Litchinitser. Twisting light with hyperbolic metamaterials. *Opt. Express*, 21(12):14975–14981, Jun 2013.
- [138] M.V. Berry and M.R. Jeffrey. Conical diffraction: Hamilton’s diabolical point at the heart of crystal optics. *Progress in Optics*, 50:13 – 50, 2007.
- [139] M. Plihal and A. A. Maradudin. Photonic band structure of two-dimensional systems: The triangular lattice. *Phys. Rev. B*, 44:8565–8571, Oct 1991.
- [140] Or Peleg, Guy Bartal, Barak Freedman, Ofer Manela, Mordechai Segev, and Demetrios N. Christodoulides. Conical diffraction and gap solitons in honeycomb photonic lattices. *Phys. Rev. Lett.*, 98:103901, Mar 2007.
- [141] Xueqin Huang, Yun Lai, Zhi Hong Hang, Huihuo Zheng, and C. T. Chan. Dirac cones induced by accidental degeneracy in photonic crystals and zero-refractive-index materials. *Nat Mater*, 10(8):582–586, 2011.
- [142] G. A. Niklasson, C. G. Granqvist, and O. Hunderi. Effective medium models for the optical properties of inhomogeneous materials. *Appl. Opt.*, 20(1):26–30, Jan 1981.
- [143] L.D. Landau, E.M. Lifshitz, and L.P. Pitaevskii. *Electrodynamics of continuous media*. Pergamon, 1984.
- [144] E. Hecht. *Optics*. Addison-Wesley Longman, Incorporated, 2002.
- [145] D. L. Portigal and E. Burstein. Internal conical refraction. *J. Opt. Soc. Am.*, 59(12):1567–1573, Dec 1969.
- [146] J.F. Nye. *Natural Focusing and Fine Structure of Light: Caustics and Wave Dislocations*. Taylor & Francis, 1999.

- [147] Omar Kidwai, Sergei V. Zhukovsky, and J. E. Sipe. Effective-medium approach to planar multilayer hyperbolic metamaterials: Strengths and limitations. *Phys. Rev. A*, 85:053842, May 2012.
- [148] M V Berry and M R Jeffrey. Conical diffraction complexified: dichroism and the transition to double refraction. *Journal of Optics A: Pure and Applied Optics*, 8(12):1043, 2006.
- [149] Akhlesh Lakhtakia, Bernhard Michel, and Werner S Weiglhofer. The role of anisotropy in the Maxwell Garnett and Bruggeman formalisms for uniaxial particulate composite media. *Journal of Physics D: Applied Physics*, 30(2):230, 1997.
- [150] Ohad Levy and David Stroud. Maxwell Garnett theory for mixtures of anisotropic inclusions: Application to conducting polymers. *Phys. Rev. B*, 56:8035–8046, Oct 1997.
- [151] R. A. de Groot, F. M. Mueller, P. G. van Engen, and K. H. J. Buschow. New class of materials: Half-metallic ferromagnets. *Phys. Rev. Lett.*, 50:2024–2027, Jun 1983.
- [152] D. Dragoman and M. Dragoman. *Quantum-Classical Analogies*. The Frontiers Collection. Springer, 2004.
- [153] C. L. Kane and E. J. Mele. \mathbb{Z}_2 topological order and the quantum spin Hall effect. *Phys. Rev. Lett.*, 95:146802, Sep 2005.
- [154] B. Andrei Bernevig, Taylor L. Hughes, and Shou-Cheng Zhang. Quantum spin Hall effect and topological phase transition in HgTe quantum wells. *Science*, 314(5806):1757–1761, 2006.
- [155] MV Berry and MR Jeffrey. Chiral conical diffraction. *Journal of Optics A: Pure and Applied Optics*, 8(5):363, 2006.
- [156] R. A. Indik and A. C. Newell. Conical refraction and nonlinearity. *Opt. Express*, 14(22):10614–10620, Oct 2006.
- [157] N. Regnault and Th. Jolicoeur. Quantum Hall fractions in ultracold fermionic vapors. *Phys. Rev. B*, 70:241307, Dec 2004.
- [158] N. R. Cooper and R. Moessner. Designing topological bands in reciprocal space. *Phys. Rev. Lett.*, 109:215302, Nov 2012.
- [159] D. Hsieh, D. Qian, L. Wray, Y. Xia, Y. S. Hor, R. J. Cava, and M. Z. Hasan. A topological Dirac insulator in a quantum spin Hall phase. *Nature*, 452(7190):970–974, apr 2008.

- [160] Joel E. Moore. The birth of topological insulators. *Nature*, 464(7286):194–198, March 2010.
- [161] D. C. Tsui, H. L. Stormer, and A. C. Gossard. Two-dimensional magneto-transport in the extreme quantum limit. *Phys. Rev. Lett.*, 48:1559–1562, May 1982.
- [162] Zheng Wang, Yidong Chong, J. D. Joannopoulos, and Marin Soljačić. Observation of unidirectional backscattering-immune topological electromagnetic states. *Nature*, 461(7265):772–775, Oct 2009.
- [163] Yin Poo, Rui-xin Wu, Zhifang Lin, Yan Yang, and C. T. Chan. Experimental realization of self-guiding unidirectional electromagnetic edge states. *Phys. Rev. Lett.*, 106:093903, Mar 2011.
- [164] Mohammad Hafezi. Measuring topological invariants in photonic systems. *Phys. Rev. Lett.*, 112:210405, May 2014.
- [165] Long-Hua Wu and Xiao Hu. Scheme for achieving a topological photonic crystal by using dielectric material. *Phys. Rev. Lett.*, 114:223901, Jun 2015.
- [166] Y. Aharonov and J. Anandan. Phase change during a cyclic quantum evolution. *Phys. Rev. Lett.*, 58:1593–1596, Apr 1987.
- [167] Joseph Samuel and Rajendra Bhandari. General setting for berry’s phase. *Phys. Rev. Lett.*, 60:2339–2342, Jun 1988.
- [168] Di Xiao, Ming-Che Chang, and Qian Niu. Berry phase effects on electronic properties. *Rev. Mod. Phys.*, 82:1959–2007, Jul 2010.
- [169] Y. D. Chong. *Two Classes of Unconventional Photonic Crystals*. PhD thesis, Massachusetts Institute of Technology, Dept. of Physics, 2008.
- [170] Markus KÄnig, Hartmut Buhmann, Laurens W. Molenkamp, Taylor Hughes, Chao-Xing Liu, Xiao-Liang Qi, and Shou-Cheng Zhang. The quantum spin hall effect: Theory and experiment. *Journal of the Physical Society of Japan*, 77(3):031007, 2008.
- [171] B. Andrei Bernevig and Shou-Cheng Zhang. Quantum spin hall effect. *Phys. Rev. Lett.*, 96:106802, Mar 2006.
- [172] S. Mittal, J. Fan, S. Faez, A. Migdall, M. Taylor, J. and M. Hafezi. Topologically robust transport of photons in a synthetic gauge field. *Phys. Rev. Lett.*, 113:087403, Aug 2014.

- [173] Kejie Fang, Zongfu Yu, and Shanhui Fan. Photonic Aharonov-Bohm effect based on dynamic modulation. *Phys. Rev. Lett.*, 108:153901, Apr 2012.
- [174] R. O. Umucalılar and I. Carusotto. Artificial gauge field for photons in coupled cavity arrays. *Phys. Rev. A*, 84:043804, Oct 2011.
- [175] Y.-J. Lin, R. L. Compton, K. Jimenez-Garcia, J. V. Porto, and I. B. Spielman. Synthetic magnetic fields for ultracold neutral atoms. *Nature*, 462(7273):628–632, December 2009.
- [176] Kejie Fang, Zongfu Yu, and Shanhui Fan. Realizing effective magnetic field for photons by controlling the phase of dynamic modulation. *Nat Photon*, 6(11):782–787, November 2012.
- [177] Kejie Fang, Zongfu Yu, and Shanhui Fan. Experimental demonstration of a photonic Aharonov-Bohm effect at radio frequencies. *Phys. Rev. B*, 87:060301, Feb 2013.
- [178] Frank Wilczek and A. Zee. Appearance of gauge structure in simple dynamical systems. *Phys. Rev. Lett.*, 52:2111–2114, Jun 1984.
- [179] John Moody, A. Shapere, and Frank Wilczek. Realizations of magnetic-monopole gauge fields: Diatoms and spin precession. *Phys. Rev. Lett.*, 56:893–896, Mar 1986.
- [180] H. Terças, H. Flayac, D. D. Solnyshkov, and G. Malpuech. Non-Abelian gauge fields in photonic cavities and photonic superfluids. *Phys. Rev. Lett.*, 112:066402, Feb 2014.
- [181] K. Osterloh, M. Baig, L. Santos, P. Zoller, and M. Lewenstein. Cold atoms in non-Abelian gauge potentials: From the Hofstadter "moth" to lattice gauge theory. *Phys. Rev. Lett.*, 95:010403, Jun 2005.
- [182] G. Juzeliūnas, P. Öhberg, J. Ruseckas, and A. Klein. Effective magnetic fields in degenerate atomic gases induced by light beams with orbital angular momenta. *Phys. Rev. A*, 71:053614, May 2005.
- [183] M. J. Edmonds, M. Valiente, G. Juzeliūnas, L. Santos, and P. Öhberg. Simulating an interacting gauge theory with ultracold bose gases. *Phys. Rev. Lett.*, 110:085301, Feb 2013.
- [184] Yu-Xin Hu, Christian Miniatura, David Wilkowski, and Benoit Grémaud. U(3) artificial gauge fields for cold atoms. *Phys. Rev. A*, 90:023601, Aug 2014.
- [185] Shiing-shen Chern. Characteristic classes of hermitian manifolds. *Annals of Mathematics*, 47(1):pp. 85–121, 1946.

- [186] J. Jost. *Riemannian Geometry and Geometric Analysis*. Universitext. Springer, 2008.
- [187] K. Yu. Bliokh, D. Yu. Frolov, and Yu. A. Kravtsov. Non-abelian evolution of electromagnetic waves in a weakly anisotropic inhomogeneous medium. *Phys. Rev. A*, 75:053821, May 2007.
- [188] Konstantin Y. Bliokh, Avi Niv, Vladimir Kleiner, and Erez Hasman. Geometrodynamics of spinning light. *Nat Photon*, 2(12):748–753, December 2008.
- [189] G.L. Kane. *Modern Elementary Particle Physics: The Fundamental Particles and Forces*. Advanced book classics. Addison-Wesley Pub., 1993.
- [190] G. Meurant. *Homotopy theory*. Pure and Applied Mathematics. Elsevier Science, 1959.
- [191] L. Tagliacozzo, A. Celi, P. Orland, M. W. Mitchell, and M. Lewenstein. Simulation of non-abelian gauge theories with optical lattices. *Nat Commun*, 4:2615, Oct 2013.
- [192] Fernando de Juan. Non-abelian gauge fields and quadratic band touching in molecular graphene. *Phys. Rev. B*, 87:125419, Mar 2013.
- [193] J. Q. Liang and X. X. Ding. Fractional angular momentum and magnetic-flux quantization. *Phys. Rev. Lett.*, 60:836–839, Feb 1988.
- [194] Haiqing Wei, Xin Xue, Jonathan Leach, Miles J. Padgett, Stephen M. Barnett, Sonja Franke-Arnold, Eric Yao, and Johannes Courtial. Simplified measurement of the orbital angular momentum of single photons. *Optics Communications*, 223(1&A3):117 – 122, 2003.
- [195] C. K. Hong, Z. Y. Ou, and L. Mandel. Measurement of subpicosecond time intervals between two photons by interference. *Phys. Rev. Lett.*, 59:2044–2046, Nov 1987.
- [196] B. Jack, A. M. Yao, J. Leach, J. Romero, S. Franke-Arnold, D. G. Ireland, S. M. Barnett, and M. J. Padgett. Entanglement of arbitrary superpositions of modes within two-dimensional orbital angular momentum state spaces. *Phys. Rev. A*, 81:043844, Apr 2010.
- [197] Stephen M. Barnett and D. T. Pegg. Quantum theory of rotation angles. *Phys. Rev. A*, 41:3427–3435, Apr 1990.
- [198] Iacopo Carusotto and Cristiano Ciuti. Quantum fluids of light. *Rev. Mod. Phys.*, 85:299–366, Feb 2013.

- [199] Charles-Edouard Bardyn, Torsten Karzig, Gil Refael, and Timothy C. H. Liew. Topological polaritons and excitons in garden-variety systems. *Phys. Rev. B*, 91:161413, Apr 2015.
- [200] Torsten Karzig, Charles-Edouard Bardyn, Netanel H. Lindner, and Gil Refael. Topological polaritons. *Phys. Rev. X*, 5:031001, Jul 2015.